Quantitative Analysis of Inline, Time-Resolved FTIR Spectra

Steps towards Full Automation

Paul Sonnendecker

12-4-2015

UNIVERSITEIT VAN PRETORIA
UNIVERSITY OF PRETORIA
YUNIBESITHI YA PRETORIA

Quantitative Analysis of Inline, Time-Resolved FTIR Spectra

Steps towards Automation

PW Sonnendecker

Supervised by:

PL Crouse

4 December 2015

Department of Chemical Engineering

Faculty of Engineering, the Built Environment and Information Technology

University of Pretoria

Pretoria

South Africa

Executive Summary

Inline, time-resolved FTIR spectra are commonly recorded after completion of the experiments. The abilities and versatility of FTIR spectroscopy can, however, also be utilised in the *in situ* quantification of absorbing mixtures. Recent developments, in the laboratory where this investigation was conducted, demands the inline quantification of PTFE pyrolysis products for process control purposes. This investigation is primarily focused on the development of a procedure and software capable of processing, fitting and quantifying real-time, time-resolved spectra. Processing methods were evaluated with respect or improvement in SNR, smoothing and baseline tracking of infrared spectra. Execution speed was also considered due the need for real-time analysis. The asymmetric least squares method proved to be the optimal choice with respect to the mentioned criteria. An asymmetric lineshape fitting function together with a Levenberg-Marquardt nonlinear solving function was introduced to represent pure component spectra mathematically. A method for quantitative analysis by means of solving a linear set of equations was developed. The software was implemented on the batch pyrolysis of PTFE pyrolysis as test case. Experiments were conducted to obtain sufficient samples of the components such that FTIR spectra could be captured. Infrared spectra of the perfluorobutenes were experimentally determined. These spectra could not be found in the available literature and are deemed to be novel. The ability of the software to perform real-time quantification of the PTFE pyrolysis stream

was demonstrated over a range of experimental conditions spanning the temperature range 650 ºC to 850 ºC, and pressures from <1kPa to 70 kPa.

Acknowledgements

The author would like to thank Prof PL Crouse and Prof PL de Vaal for their continued support and supervision during the course of this project.

I would like to extend a special thank you to Mr Carl Sandrock for his technical contributions, guidance and advice.

Table of Contents

List of Figures

List of Tables

1 Introduction

The fast, vacuum pyrolysis of polytetrafluoroethylene is a relatively well published field in historic and recent literature (Lewis & Naylor, 1947; Collins, Fiveash & Holland, 1969; Morisaki, 1978; Szekely *et al.*, 1987; Simon & Kaminsky, 1997; Meissner, Książcak, Boniuk & Cudzilo, 2003; Wróblewska & Milchert, 2003 and Bhadury *et al.*, 2006). The kinetics of side reactions, amongst others, the formation of hexafluoropropylene (HFP) and octafluorocyclobutane (OFCB) from tetrafluoroethylene (TFE), are also well known (Lacher, Tompkin & Park, 1952; Atkinson & Trenwith, 1953; Atkinson & Atkinson, 1957; Butler, 1961; Drennan & Matula, 1968 and Buravtsev & Kolbanovskii, 2001). The Fluoro-polymer Laboratory (FPL) is advancing toward continuous pyrolysis of PTFE as well as continuous separation of the pyrolysis product stream. From the known literature, no conclusive model is available with respect to the pyrolysis reaction mechanism, nor are stepwise kinetic data available. The qualitative and quantitative analyses are usually done by gas chromatography, which implies a relatively long lead-time between sampling and analysis.

Due to the variation in the reported mechanisms, the age and sophistication of results and equipment used by some of the researchers, and the lack of a comprehensive kinetic study, it is very difficult to predict process conditions and product selectivity during continuous pyrolysis of PTFE. Implementation of a process control philosophy for such a fast reaction is complicated since the process conditions and product selectivity cannot be predicted with great certainty. Furthermore, qualitative analyses of the bottoms and/or distillate of a separation column must be done with as little dead-time as possible, to ensure successful operation of a column.

The above mentioned complications necessitated the development of a qualitative and, if at all possible, quantitative method for the analysis of pyrolysis product gas

and the bottoms and distillate product obtained from distillation. Infrared (IR) spectroscopy proves to be the quickest and easiest method to obtain qualitative data for the gaseous products produced. The decision was therefore made to devise a method, that employs IR spectroscopy, to characterise the pyrolysis products and that is versatile enough to use in various other application within the Fluoro-polymer Laboratory. This entailed the development of a software package that can be used in a laboratory environment and that can provide qualitative and quantitative results as the process proceeds. The software package was specified to include the following features:

1. Preprocessing of infrared spectra, with the emphasis on baseline removal and smoothing.
2. Fitting of the known component spectra to an experimental spectrum and minimising the residual of that spectrum after all components have been subtracted. Spectra for all the components in the pyrolysis product stream are not widely available. For these components, as pure as possible spectra should be obtained.
3. Provision of qualitative and quantitative results on the possible pyrolysis product stream.
4. Optimisation of the software package with respect to execution time to facilitate the successful implementation of a process control philosophy.
5. An additional, yet not critical, objective was to implement the code such that it is applicable to other analytical platforms, such as GC-FTIR or TGA-FTIR.

The method developed was tested on the case of vacuum pyrolysis of PTFE with the subsequent formation of only tetrafluoromethane (TFM), hexafluoroethane (HFE), tetrafluoroethylene (TFE), octafluoropropane (OFP), hexafluoropropene (HFP), octafluorocyclobutane (OFCB), 1-and 2-octafluorobutene (OFB) and perfluoroisobutane (PFIB). The products mentioned are those reported by Lewis & Naylor (1947) with the corresponding temperature and pressure range of

550 – 850 °C and 0 – 70 kPa (abs) respectively. The qualitative analysis of the data is of utmost importance. However, quantitative analysis is the ultimate objective. This study is limited to the method, rather than the exact solution to this problem. Experimental spectra obtained for the low-fraction components (TFM, HFE, OFP, OFB and PFIB) are for qualitative in-house analysis and are not for publication as absolute scientific values. Quantitative spectra for the three major components, TFE, HFP and OFCB, were determined.

2 Algorithm and Software Development

The work presented in this section pertains to the development of software for the automated analysis of time-resolved infrared spectra. No experimental data were considered in the validation of the software in this section.

2.1 Literature

More often than not, infrared spectra contain some unwanted high-frequency, noise, and low-frequency background components. These components distort the desired data, hampers automated processing, and may yield erroneous results when qualitative or quantitative analyses are done. A typical experimental spectrum is mathematically expressed by Equation (1).

$$\bar{y} = \left(\bar{s} + \bar{b}\right) * \bar{p} + \bar{n} \tag{1}$$

Here $\bar{y} = \{y_1, y_2, \ldots, y_i\}$ are the spectral intensities over a measured frequency range. The desired spectrum is represented by $\bar{s}$,while $\bar{b}$ is the background or low-frequency component, and $\bar{p}$ is a blurring function (with $*$ denoting convolution), and $\bar{n}$ represents noise. The undesired components may be known or unknown, determined explicitly, implicitly or ignored (Schulze *et al.*, .2005).

An alternative representation of an arbitrary, experimentally determined spectrum is given Equation (2).

$$\bar{y} = \bar{s} + \bar{b} + \bar{n} \tag{2}$$

All components have the same meaning as previously mentioned (Liland, Almøy & Mevik, 2010). However, this representation either assumes a zero blurring function or it is assumed to be part of the background. Figure 1 depicts an arbitrary,

experimental spectrum. The effect of noise is clearly visible and an offset from zero absorbance is also noticeable due to background addition.

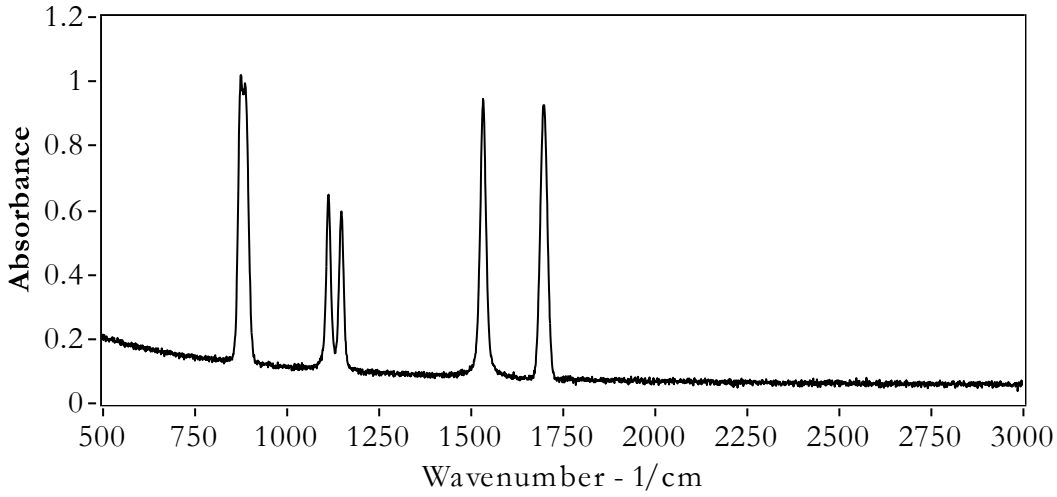

Figure 1: An arbitrary FTIR spectrum with a background addition and noise.

The removal of these artefacts may be necessary for presentation of data or for more precise requirements, post-processing or quantification of data. Depending on the requirements of the removal of these artefacts, one must evaluate complexity, modes of failure, and computational resources (Schulze *et al.*, 2005).

As seen in Figure 2, the background and noise should be removed from an experimental infrared spectra before accurate analysis or processing of the data can be done. The background component can be attributed to various factors and can take almost any shape, depending on the instrument in use, chemical composition and analytical method in use. Noise can arise from the instrument itself, for example the source, input and output transducer or signal-processing elements or from uncontrollable variables within the sample (Skoog, Holler & Nieman, 1998: 100). The cause of these effects is beyond the scope of this text, however, it is necessary to remove these components from experimental data if post-processing is required.

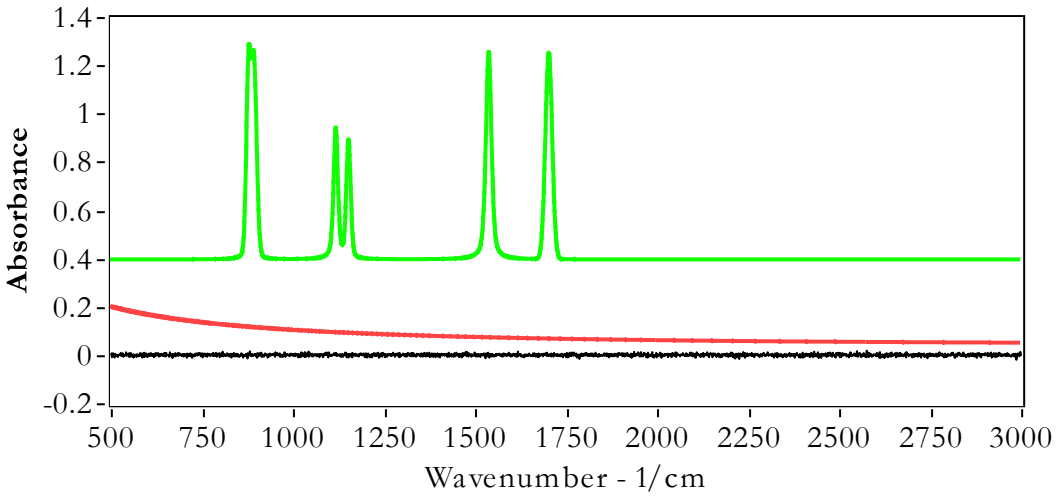

Figure 2: The separate components from the spectrum in Figure 1. From top to bottom, desired spectral data, **s**, background, **b**, and noise, **n**. The components are translated for clarity.

2.1.1 Beer's Law

Beer's law, occasionally referred to as Beer-Lambert law or Beer-Lambert-Bouguer law, relates the absorbance, A, of an absorbing specie, to the path length, l,of the incident radiation and the concentration, c, of the absorbing specie.

$$A = \varepsilon bc \tag{3}$$

The law states that, for a beam of parallel, monochromatic radiation, the absorbance varies linearly as a function of the path length and concentration, such that: the slope of the linear relationship, ε (which is referred to as the molar attenuation coefficient), is a collection of constant values obtained from the derivation, from first principles, of the law (Skoog *et al.*, 1998: 302).

Beer's law can be applied to a mixture of non-interacting components such that the total absorbance is equal to the sum of the absorbances of the individual (Skoog *et al.*, 1998: 303). Mathematically, this can be represented by Equation (4).

$$A_{Total} = \sum A_i = \sum \varepsilon_i b c_i \tag{4}$$

Beer's law is limited in its ability to predict non-ideal systems. Deviation from the linear relationship are frequently observed. When the concentrations of absorbing species are fixed, deviations are commonly encountered due to the interaction of molecules at higher concentrations. For the best results, the concentration of absorbing species should be kept as low as possible. Furthermore, the molar attenuation coefficient is also a function of the refractive index of the mixture. Changes in concentration could alter the refractive index and consequently cause deviations in linearity.

2.1.2 Baseline Correction Methods

Baseline correction is a comparatively poorly published field given the vast range of scientific and mathematical analysis methods to which it is applicable (Komsta, 2011, Schulze *et al.*, 2005). Baseline correction methods (BCMs) vary in different aspects and Schulze *et al.* (2005) classifies some of them according to Table 1.

Table 1: Baseline correction methods based on information required (Schulze *et al.*, 2005).

Class	Method
Methods requiring no explicit knowledge of $\bar{p}$, $\bar{b}$, or $\bar{n}$	Noise median method (NMM) First derivative method (FDM)
Methods requiring estimates of $\bar{b}$	Artificial neural networks (ANN) Threshold-based classification (TBC) Signal removal methods (SRM) Composite (linear-sine-cosine) baseline method (CBM) Spectra shift methods (SSM)
Methods requiring estimates of $\bar{b}$ and $\bar{n}$	Manual methods (MM)
Methods requiring use of $\bar{p}$, $\bar{b}$, and $\bar{n}$	Maximum entropy method (MEM)
Methods requiring information about frequency	Fourier transform method (FTM) Wavelet transform method (WTM)

Liland *et al.* (2010) investigated more recent techniques, such as an asymmetric least squares (ALS) method proposed by Eilers (2003), robust baseline estimation (RBE) proposed by Ruckstuhl *et al.* (2001), and the rolling ball method proposed by Kneen & Annegarn (1996). Liland also investigated methods published in the work by Schulze *et al.* (2005). These methods are those described by Friedrichs (1995), which are classified as the noise median method by Schulze, signal and baseline estimation by polynomial or spline fitting, and the wavelet transform method.

Based on the methods proposed and findings by Schulze *et al.*, Liland *et al.* and Komsta, a shortlist of favourable baseline correction methods are given in the sections that follow.

2.1.2.1 Asymmetric Least Squares Algorithm

Eilers (2003) published an algorithm based on the Whittaker smoother. This smoothing function relies on discrete penalised least squares to minimise an objective function Q (Equation (5):

$$Q = S + \lambda R \tag{5}$$

Here

$$R = \sum_i (\Delta z_i)^2 \tag{6}$$

$$S = \sum_i (y_i - z_i)^2 \tag{7}$$

λ is a fitting parameter, y a noisy series of arbitrary length, z the fitted series, and $\Delta z_i = z_i - z_{i-1}$ the first order difference. The fitting parameter, λ, penalises the smoothing of the curve for small values of λ and increases smoothing for larger values, with the disadvantage of a decrease in the fit of the data.

For increased computational performance, Eilers suggests the use of matrices and vectors. For even better computational performance, the use of sparse matrices are also introduced. When matrices and vectors are used, Equation (5) can be written as:

$$Q = |\bar{y} - \bar{z}|^2 + \lambda |D\bar{z}|^2 \tag{8}$$

$$D = \begin{bmatrix} -1 & 1 & 0 \\ 0 & -1 & 1 \end{bmatrix}$$

D is a matrix such that $D\bar{z} = \Delta\bar{z}$. The vector of partial derivatives is shown in Equation (9). Equating this to zero one obtains a linear set of equations (Equation (10)).

$$\frac{\partial Q}{\partial z'} = -2(\bar{y} - \bar{z}) + 2\lambda D'D\bar{z} \tag{9}$$

$$(I + \lambda D'D)\bar{z} = \bar{y} \tag{10}$$

I represents an identity matrix and D' is the transposed matrix of D. According to Eilers, the use of sparse matrices reduced the computational time by a factor of 100.

Furthermore, in the above series of equations the first-order difference is used, whereas the original Whittaker smoother used third order differences. The second and third order differences are shown in Equation (11) and (12).

$$\Delta^2 z_i = \Delta(\Delta z_i) = (z_i - z_{i-1}) - (z_{i-1} - z_{i-2}) \\ = z_i - 2z_{i-1} + z_{i-2} \tag{11}$$

$$\Delta^3 z_i = \Delta(\Delta^2 z_i) = z_i - 3z_{i-1} + 3z_{i-2} - z_{i-3} \tag{12}$$

Eilers also suggests a weight vector to handle missing data. It is suggested that a weight of $w_i = 0$ for missing data points be used and for all other data $w_i = 1$. More complex criteria for the weight vector can also be included. Equation (13) shows the addition of the weight vector to Equation (10), where $W = \bar{w}I$.

$$(W + \lambda D'D)\bar{z} = W\bar{y} \tag{13}$$

The fitting parameter can be automatically validated by cross reference as suggested by Eilers. This is however beyond the scope of this text.

A more recent study by He *et al.* (2014) adapted the asymmetric least squares method and applied this method to Raman spectra. He *et al.* states that the asymmetric least squares method only considers the second derivative with respect to the smoothness. The suggested improvement is to include the first derivative since the baseline correction method should include the constraints of a well fitted baseline and that the first derivatives for the baseline are close to each other. Considering the above mentioned, they suggest the following addition to Eilers' second order derivative penalty method:

$$Q = \sum_i (y_i - z_i)^2 + \lambda_1 \sum_i (\Delta(y_i - z_i))^2 \\ + \lambda \sum_i (\Delta^2 z_i)^2 \tag{14}$$

Equation (14) can be rewritten in matrix form and is shown in Equation (15).

$$(W'W + \lambda_1 D'_1 D_1 + \lambda D'D)\bar{z}) = (W'W + \lambda_1 D'_1 D_1)\bar{y} \qquad (15)$$

All symbols have the same meaning as previously. The solution of this method is based on the prediction of a baseline. A second order polynomial is suggested, from which an iterative process continues. The process is shown in Figure 3. He *et al.* report a significant increase in computational time, with the advantage of a decrease in root mean square error of at least ten fold.

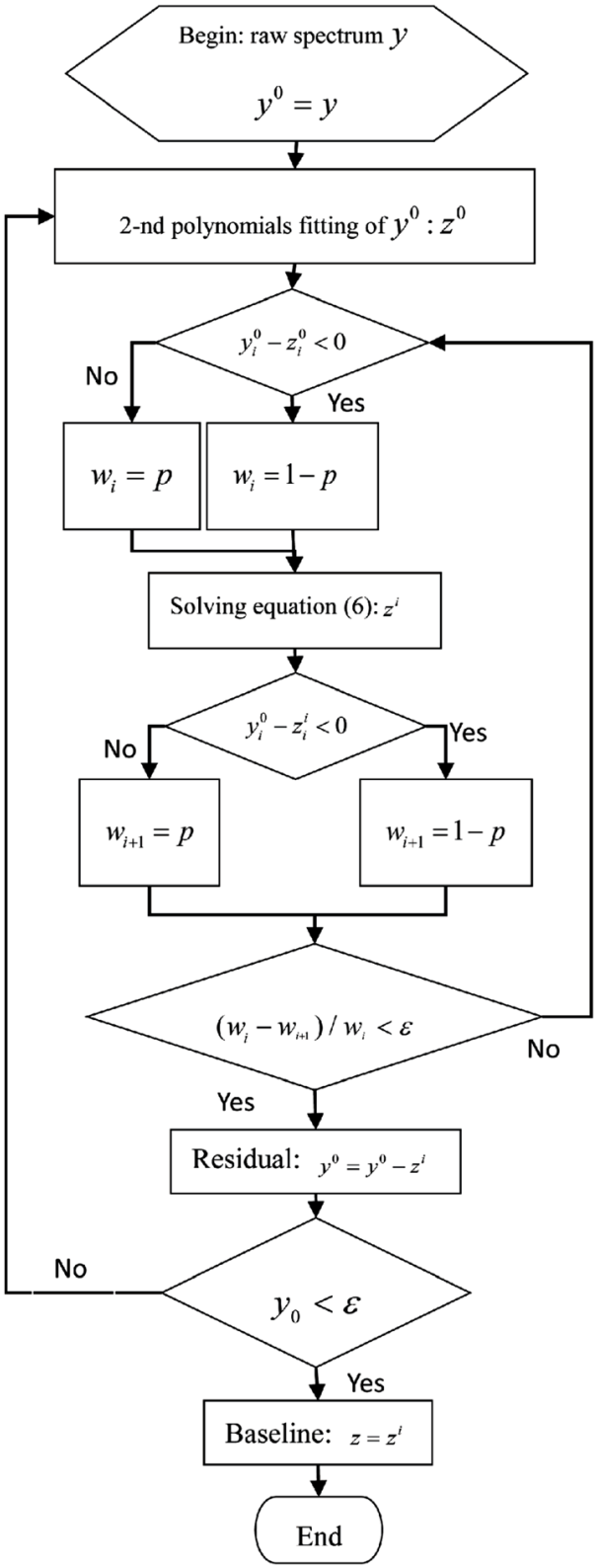

Figure 3: The flow diagram indicating the solution method for the improved asymmetric least squares method (He *et al.* (2014)

2.1.2.2 LOWESS and Robust Baseline Estimation

The robust baseline estimation (RBE) technique, proposed by Ruckstuhl *et al.* (2001), relies on spectra having sharp features convolved on a continuous baseline with a relatively slow varying first derivative. This technique employs methods of robust local regression to determine the baseline component. Peaks are considered outliers and are weighted such that the estimator rejects these areas. As with almost all other baseline estimations, congested peak areas pose an additional difficulty if the baseline is not smooth or slowly varying, in other words, easily predictable.

Some baseline estimation methods rely on a known shape of the baseline, with the RBE it is locally estimated by a low order polynomials and need not be known. The window size of each local neighbourhood of data points used, determines the fit to the data. The smaller the window the better the fit, with less smoothing of noise. A larger window will smooth the data more but with a worse fit.

Cleveland (1979) developed the LOcally WEighted Scatter plot Smoother (LOWESS). The RBE is closely related to this method. For clarity, the LOWESS method will first be introduced, and thereafter, the additions made by Ruckstuhl *et al.*

For a data set $(x_i,\ y_i)$ with y_i, the response to the independent variable x_i, a regression curve can be fitted such that:

$$y_i = g(x_i) + E_i \text{ where } (i = 1, \dots, n) \tag{16}$$

In Equation (16), E_i represents an unknown error and it can be assumed that this error is evenly distributed with a mean zero and variance of one. Locally weight regression and robust locally weight regression is a common procedure in data processing and is defined by the following procedure:

1. Estimate the coefficients, $\hat{a}_j$ for $j = 0, \dots, d$, of a d[th]-order polynomial regression on a subset of (x_i, y_i), denoted by (x_k, y_k). These coefficients are calculated by solving Equation (17), which is a fit of weighted least squares, with weight $w_k(x_i)$.

$$\sum_{k=1}^{n} w_k(x_i)\left(y_k - a_0 - a_1 x_k - \cdots - a_d x_k^d\right)^2 = 0 \qquad (17)$$

   Once the coefficients of the d[th]-order polynomial regression is known, one can calculate the fitted value, $\hat{y}_i$, at x_i:

$$\hat{y}_i = \sum_{j=1}^{d} \hat{a}_k(x_i) \cdot \left(x_i^j\right) = \sum_{k=1}^{n} r_k(x_i) \cdot y_k \qquad (18)$$

   In Equation (18), $r_k(x_i)$ represents the coefficients that arise from the regression of y_k.

2. To introduce robustness, Cleveland includes the robustness weights, $w \cdot \delta_k$, which are defined as indicated in Equation (19).

$$\delta_k = B\left(\frac{e_k}{6 \cdot s}\right) \qquad (19)$$

$$B(x) = \begin{cases} (1 - x^2)^2, & |x| < 1 \\ 0, & |x| \geq 1 \end{cases}$$

$$e_i = y_i - \hat{y}_i$$

Here s is the median of $|e_i|$.

3. Once the robustness weights, Equation (19), have been calculated, new fitted values, $\hat{y}_i$, are calculated for $i = 1, \dots, n$, by replacing the initial $w_k(x_i)$ weights with $\delta_k \cdot w_k(x_i)$.
4. Steps 2 and 3 are repeated a number of t times.

Cleveland defines the weight function as a unimodal, symmetrical, nonnegative function that is zero outside the window of interest. The suggested function is a tricube kernel, centred about x_i as shown in Equation (20).

$$w_k(x_i) = \begin{cases} \left(1 - \left|\frac{x_i - x_k}{h}\right|^3\right)^3, & |x_i - x_k| < h \\ 0, & |x_i - x_k| \geq h \end{cases} \qquad (20)$$

The RBE procedure includes several additional features to that of the LOWESS with respect to an additional robustness weight as well as iterative re-evaluation of a scale parameter. The RBE procedure is recommended for future investigation and is considered beyond the scope of this text.

2.1.2.3 Noise-Median Method

Friedrichs (1995) proposed a model-free algorithm for the estimation of the baseline. It is said to be model-free since it does not require the discrimination of peaks from noise extrema and no assumptions are made with respect to the source or form of the baseline.

Instead of defining the noise of a spectra to have a mean of zero, Friedrichs employs method where the number of local maxima and minima is used. Peaks are therefore only seen as another maximum in the spectra. In other words, sections of the baseline is fitted by the median of extrema over a selected window size. This is done for each point on the spectra to obtain the entire baseline of the spectra. Friedrichs defines extrema as intensitis, y_i, which are greater or less than both neighbouring points, y_{i-1} and y_{i+1}. As Friedrichs states, "since no assumptions regarding the functional form of the artefact is made, the shape of the distortion that can be handled is arbitrary".

Modifications to the spectrum must be made at the boundaries since a fixed window size will have to extend past each boundary by $h/2$, with h being the number of

data points in the window. Friedrichs suggests wrapping the spectrum such that the lower boundary will include the last $h/2$ data points of the upper boundary of the spectrum and *vice versa*. This method will only hold if the baseline is relatively continuous over the boundaries. If this assumption is not satisfied, Friedrichs suggest using only the first and last h points of the spectrum. Consequently, the first $h/2$ points would not be centred about the calculated median and would have the same resulting baseline.

To remove sharp discontinuities from the baseline, Friedrichs applies a Gaussian function to the estimation algorithm. The final baseline estimation algorithm is shown in Equation (21).

$$B(i) = \sum_{j = i - (h/2)+1}^{i + (h/2)} M(j) \cdot G(i - j) \tag{21}$$

Here $M(j)$ is the median value at point j and $G(i - j)$ is a Gaussian function centred about zero and normalized, as shown in Equation (22). Let $k = i - j$ to reduce the Gaussian function to Equation (22).

$$\sum_{k = -(h/2)}^{(h/2) - 1} G(k) = 1 \tag{22}$$

If the standard deviation, σ, of the Gaussian curve is reduced substantially, one obtains a weighted distribution that starts at a uniform distribution and reduces to a delta function as σ approaches zero. The standard form of a Gaussian equation can be seen in section 2.1.3 on page 17.

As mentioned in other locally solved methods in this text, the success of this method is strongly dependent on the window size, h. The window size must be chosen large enough such that the number of local extremes, resulting from noise, dominates the

median. However, selection of a window size too big will provide false estimations of the baseline.

The major disadvantage of this method is the application to areas of spectra where there are unresolved peaks. If the number of extrema from desired peaks approaches the number of noise extrema, this estimation will be biased and penalize the desired peaks. Very broad peaks can also bias the baseline estimation which will penalize the desired peak(s) as well. One should also keep the signal-to-noise-ratio in mind when using this method, since the success of the method is highly dependent on the number of local extrema in the window. Friedrichs suggests that for higher signal-to-noise ratios, ~60, one should use a window size double that of the peak linewidth. For lower signal-to-noise ratios, 10 – 20, the window size must be two to three times larger than the linewidth of the peak.

Congested areas are usually smoother than the rest of the spectrum, due to the ratio between peak intensities and noise. There are therefore fewer extrema in these areas and the algorithm deviates from the baseline. To improve on the baseline estimation in areas congested with desirable peaks, Friedrichs suggests the use of a variable window size. The method described by Friedrichs to remedy this problem, is to determine the maximum number of extrema in a user specified, fixed, window size. This maximum number of extrema is then used to determine the window size at any given point, in other words, any given window must include the same number of extrema as any other window. This method is advantageous since areas with more noise will be smoothed more that areas with less noise. However, this advantage inherently increases computation time.

2.1.3 Infrared Absorbance Lineshape Fitting

Numerous mathematical models can be fitted to spectral bands or to total spectra (Pitha & Jones, 1966; Vandeginste & De Galan, 1975 and Stancik & Brauns, 2008). The most widely published method for lineshape fitting is either a pure Lorentzian

function, pure Gaussian function or a combination of the two, known as a Voigt function. The choice of the mentioned function is not due to mathematical simplicity but rather due to the fact that the peak width, area and position are relevant quantities and are the parameters fitted to both Lorentzian and Gaussian curves (Stancik & Brauns, 2008).

Different forms of the Lorentzian function are found in literature (Pitha & Jones, 1966; Vandeginste & De Galan, 1975 and Stancik & Brauns, 2008). The form of the function that will be used in this text is the form published by Stancik & Brauns (2008).

$$L(x) = \frac{2A/\pi\gamma_0}{1 + 4[(x - x_0)/\gamma_0]^2} \tag{23}$$

Equation (23) is a normalized Lorentzian function with A the area under the peak, γ_0 the full width at half maximum, and x_0 the centre of the peak in wavenumbers. The numerator is the normalization constant in Equation (23). According to Stancik & Brauns, radiation dampening and collision broadening give rise to Lorentzian lineshapes, while Doppler broadening gives rise to Gaussian lineshapes. The Gaussian function used is as proposed by Stancik & Brauns and is shown in Equation (24).

$$G(x) = \frac{A}{\gamma_0}\sqrt{\frac{4\ln 2}{\pi}}\exp\left[-4\ln 2\left(\frac{x - x_0}{\gamma_0}\right)^2\right] \tag{24}$$

The parameters in Equation (24) have the same meaning as in Equation (23) with the term in front of the exponential serving as the normalisation constant.

Due to the variation in magnitude of the three factors contributing to these lineshapes, a combination of these lineshapes must be used to fit real infrared spectra. A true Voigt function is a convolution of a Gaussian and Lorentzian function and increases the complexity of the mathematical model. If one is

interested in the reduction of calculation time or mathematical simplicity, a pseudo-Voigt function can be used as proposed by Stancik & Brauns (2008). Other variations of the Voigt function are discussed by Pitha & Jones (1966) and Vandeginste & De Galan (1975). The pseudo-Voigt function as discussed here is a summation of fractions of Gaussian and Lorentzian functions and can be seen in Equation (25).

In Equation (25), f represents the fraction of a Lorentzian lineshape. This model can therefore predict pure Lorentzian and pure Gaussian curves by the manipulation of f.

$$V(x) = fL(x) + (1 - f)G(x) \tag{25}$$

Another common problem associated with infrared bands is that of asymmetry in the lineshape. Stancik & Brauns propose the addition of asymmetry to model spectra more accurately. Non-physical peak widths can occur with the use of unbounded asymmetric functions. Stancik & Brauns therefore propose a sigmoidal function as shown in Equation (26). This function is bounded at 0 and $2\gamma_0$ for $a = \infty$ and $a = -\infty$ respectively.

$$\gamma(x) = \frac{2\gamma_0}{1 + \exp[a(x - x_0)]} \tag{26}$$

Asymmetry is then implemented in the model by substituting the constant, γ_0, in Equations (23) and (24) with the dependent variable γ from Equation (26). This adaptation incurs an increase in complexity and computation time.

2.1.4 Quantification of Infrared Absorbance Spectra

Quantification of chemical species by means of Fourier transform infrared spectroscopy is a well-known, yet disputed method of quantification, due to the deviation from Beer's law as well as possible inaccuracy of the molar attenuation

coefficient. Deviations from linearity can also arise from overlapping peaks and chemical interactions (Skoog *et al.*, 1998: 418; Stec *et al.*, 2011; Xin *et al.*, 2014 and McCue *et al.*, 2015).

Even though this method is prone to deviations, it is still widely used in numerous disciplines. FTIR spectroscopy is advantageous as it is non-invasive, fast and applicable to almost any absorbing chemical species. It has been applied to *in situ* analysis of fire gases (Stec *et al.*, 2011), adsorbed species in catalysis (McCue *et al.*, 2015) and characterisation of coal functional groups (Xin *et al.*, 2014) amongst others.

In theory, quantification of the constituents of a mixture should be relatively easy since the attenuation coefficient is the only parameter to obtain for each component. However, due to the deviations from linearity, a full set of calibration spectra for each component must be obtained for accurate results. Furthermore, the concentration of a mixture is often dependent on temperature and pressure, especially in the event of a gaseous mixture. If variations in these conditions are considered, the calibration data must be expanded to include these effects.

For the sake of brevity, a short discussion of the basic procedure used by McCue *et al.*, Stec *et al.* and Xin *et al.* will be included. As mentioned previously, a representative set of spectra, as a function of the concentration or pressure in the case of gaseous mixtures, must be obtained for each individual component in a mixture. The molar attenuation coefficient can be calculated from the calibration data set. The molar attenuation coefficient varies exponentially through the path length of the medium. For a fixed path length, as would be considered for infrared spectroscopy, the coefficient is an indication of the number of absorbing molecules encountered through the medium.

The spectrum of a mixture of components can be predicted by the cumulative spectra of all individual components as per Equation (4) in Section 2.1.1. The sum

of these spectra can be subtracted from the acquired experimental spectrum and minimised to obtain the absorbance of each component.

The concentration of each component can then be determined by means of Beer's law using the previously determined attenuation coefficients.

2.2 Software Development

2.2.1 Baseline Removal and Smoothing

Software was developed to pre-process spectral data by means of smoothing and the removal of any baseline trends. For purposes of calibration and curve fitting, data were imported from multiple spectra, normalised to maximum absorbance of unity and averaged to obtain a better signal-to-noise ratio and penalise any artefacts that may have been imposed on an individual spectrum.

The spectrum is scanned for peaks by means of a LabVIEW library function, *Multiscale Peak Detection*, which uses multiresolution wavelet analysis to detect the peaks in the spectrum. A constant window size is added to the peak position and a weight vector, consisting of 0s and 1s is constructed. The weight vector is applied to the smoothing techniques and therefore discriminates against the smoothing of the area under peaks. The window must be chosen sufficiently large to include the tails of the peaks. If the window does not include the tails, the peak intensity is reduced.

The spectrum is smoothed and any baseline removed by means of a Whitaker Smoother (Asymmetric Least Squares algorithm), the Noise-Median Method or an adapted LOWESS smoother, all methods are discussed in Section 2.1.2 on page 7.

Weighting the peaks as unity ensures that the algorithm does not penalise the peak intensity and indirectly interpolates over spectral bands. Congested peak areas may incur some inaccuracy due to interpolation over large areas. Therefore, the choice of the weighting window size is of utmost importance to ensure good results.

2.2.2 Absorption Spectra Fitting

A smoothed, baseline corrected, and normalised spectrum, or the mean of multiple spectra, is selected for the nonlinear spectrum solving function. Various functions

are called during this operations. The procedure is summarised in Figure 4. The function detects peaks by means of multiresolution wavelet analysis with a pre-set width and threshold. Once the number of peaks, centre wavenumber (hereafter referred to as location) and amplitude is known, the *init_param_search* function is called (refer to Figure 5 for a flow diagram of the procedure).

The *init_param_search* function searches for non-zero minima between peaks. Minima equal to zero are excluded since these represent the baseline or bands of zero absorbance. Non-zero minima between two consecutive peak locations represents an overlap in these two peaks. If it occurs that a given peak has a peak and local minimum trailing it, as well as a local minimum and leading peak, it is considered to be congested. If a peak is congested, either side of the centre could be affected by the surrounding peaks and no accurate approximation of the Gaussian coefficients can be made. Congested peaks are approximated after all trailing and leading peaks have been approximated and subtracted.

Isolated and peaks leading or trailing congested areas are approximated by fitting a Gaussian curve to a window of values to the left or right of the peak centre. The *Gaussian Peak Fit Coefficients* function is a LabVIEW library function and has outputs of intensity, a, peak centre, b, and standard deviation, c. This generalised form of the Gaussian function is shown in Equation (27).

$$G(x) = a\exp\left[\left(\frac{x-b}{c}\right)^2\right] \tag{27}$$

The area under a Gaussian curve and the full width at half maximum can be calculated with Equation (28) and (29) respectively. These parameters are the same for both Gaussian and Lorentzian functions and are necessary for the function variations as used by Stancik & Brauns (2008).

$$A = \sqrt{(2\pi)}ac \tag{28}$$

$$\text{FWHM} = \gamma_0 = 2\sqrt{(2ln2)c} \tag{29}$$

Once these parameters are known, the Voigt function parameter is solved by means of the nonlinear Levenberg-Marquardt method.

The sum of all the individual peaks is subtracted from the experimental spectrum and the process is iterated until the initial number of peaks has been solved for.

During the execution of the *init_param_search* function the *higher-order_derivative_test* function is also called. A flow diagram of this function can be seen in Figure 6. The peak detection function can only detect peaks that are sufficiently resolved such that a threshold value can be applied. Shoulder peaks with maxima below the threshold and shoulder peaks that only impose an inflection point on the spectrum are not detected. Inflection points are detected by approximating the higher-order derivatives of the spectrum. These are calculated up to the third order since higher-order derivatives on experimental data can lead to erroneous extrema due to noise. A summary of the procedure is given in the following text (refer to Figure 6 for the flow diagram of the *higher-order_derivative_test* function):

1. Isolate a window around a peak position. The window size is predetermined to be 20 indices for peaks with intensity of above 0.6 (for a normalised spectrum with maximum absorbance of 1), 15 indices for peaks with intensity between 0.3 and 0.6 and 10 indices for peaks with intensity below 0.3.
2. Exclude all indices with absorbance of less than 0.005 and first derivative value of less than $0.015y_i$. This step ensures that noisy sections at the base of peaks are not interpreted as possible inflection points.
3. Find all indices were the second derivative crosses the abscissa. These are possible inflection points but not necessarily inflection points indicating shoulder peaks.
4. For shoulder peaks toward lower wavenumbers, the first derivative will be positive. A strictly increasing inflection point will therefore have a positive

third derivative as well. For shoulder peaks toward higher wavenumbers, both first and third derivative must be negative to indicate a strictly decreasing inflection point.

5. If an index tests positive for all above mentioned steps, it is likely to have a shoulder peak in the vicinity of the corresponding wavenumber.

The high order derivative test is not always conclusive. It is not included in the test to yield perfect results. It is however very effective in indicating possible shoulders to the user which can be included after visual inspection in the results.

The *nonlinear_fit* function (Figure 4) is ready to optimise all parameters after all iterations of the *init_param_search* function has been executed. It is imperative to know that the success of a nonlinear solving function is primarily based on the quality of the starting values of all parameters. The nonlinear solving function used is a LabVIEW library function included in the Full Development System. Two instances are provided as standard: an instance using the Levenberg-Marquardt (LM) algorithm, and another that uses the Trust-Region DogLeg (TRDL) algorithm. Both instances of this function are solved to provide the user with different optimised solutions.

The asymmetry parameter, as discussed in Section 2.1.3 on page 17, is introduced only after an optimised solution for symmetric lineshapes is found. This sequential optimisation is performed to ensure high quality initial parameters and because asymmetry significantly complicates the solution, leading to an ill-behaved set of equations.

A third and final optimisation of the parameters is performed to include the shoulder peaks detected with the higher-order derivative test.

Both instances of the nonlinear solving function can be solved using either the least squares error (LSE), least absolute residual (LAR), or the bi-square method.

The goodness of fit for all sets of parameters are evaluated by means of the R - square method and the Root Mean Squared Error (RMSE) between the best fit and the experimental spectrum. These methods provide a good indication of the error of the optimum fits. However, visual inspection must always be done to ensure that the solution represents the experimental spectrum.

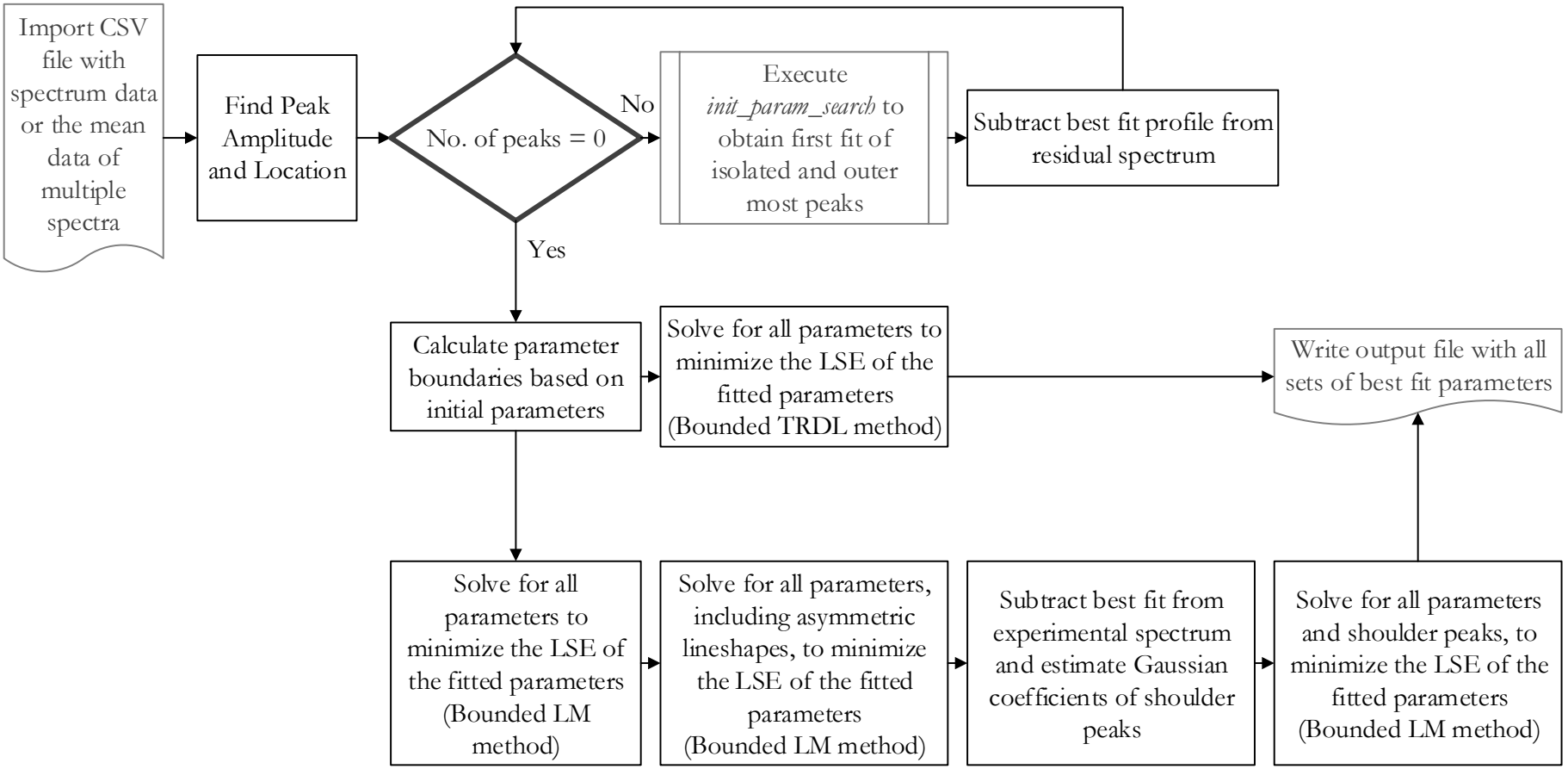

Figure 4: The *nonlinear_fit* function. This function calls *init_param_search* to obtain the initial parameters for all detected peaks and optimises these parameters using the Trust-Region DogLeg method and the Levenberg-Marquardt method.

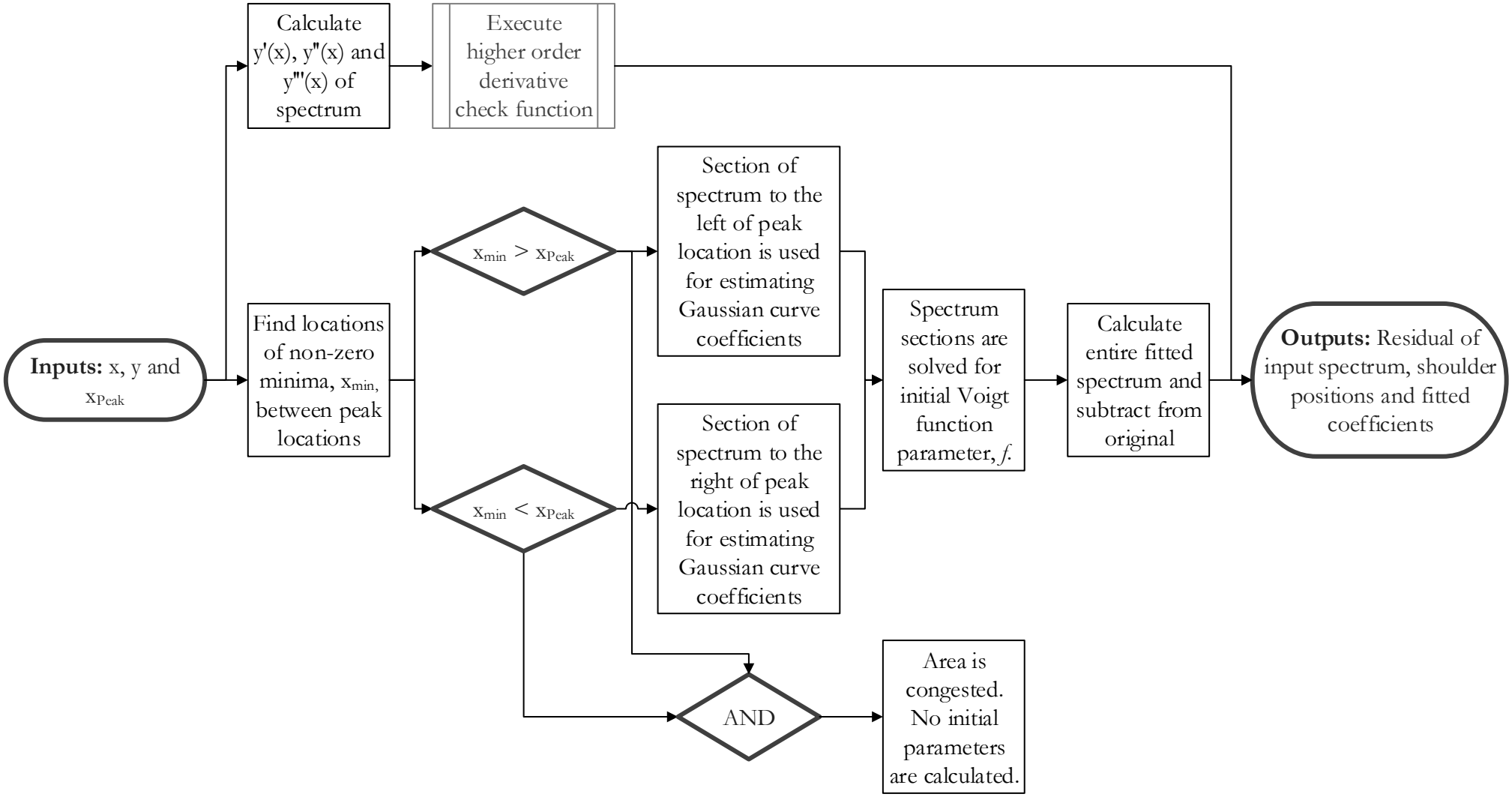

Figure 5: The *init_param_search* function procedure to estimate the initial parameters of individual peaks.

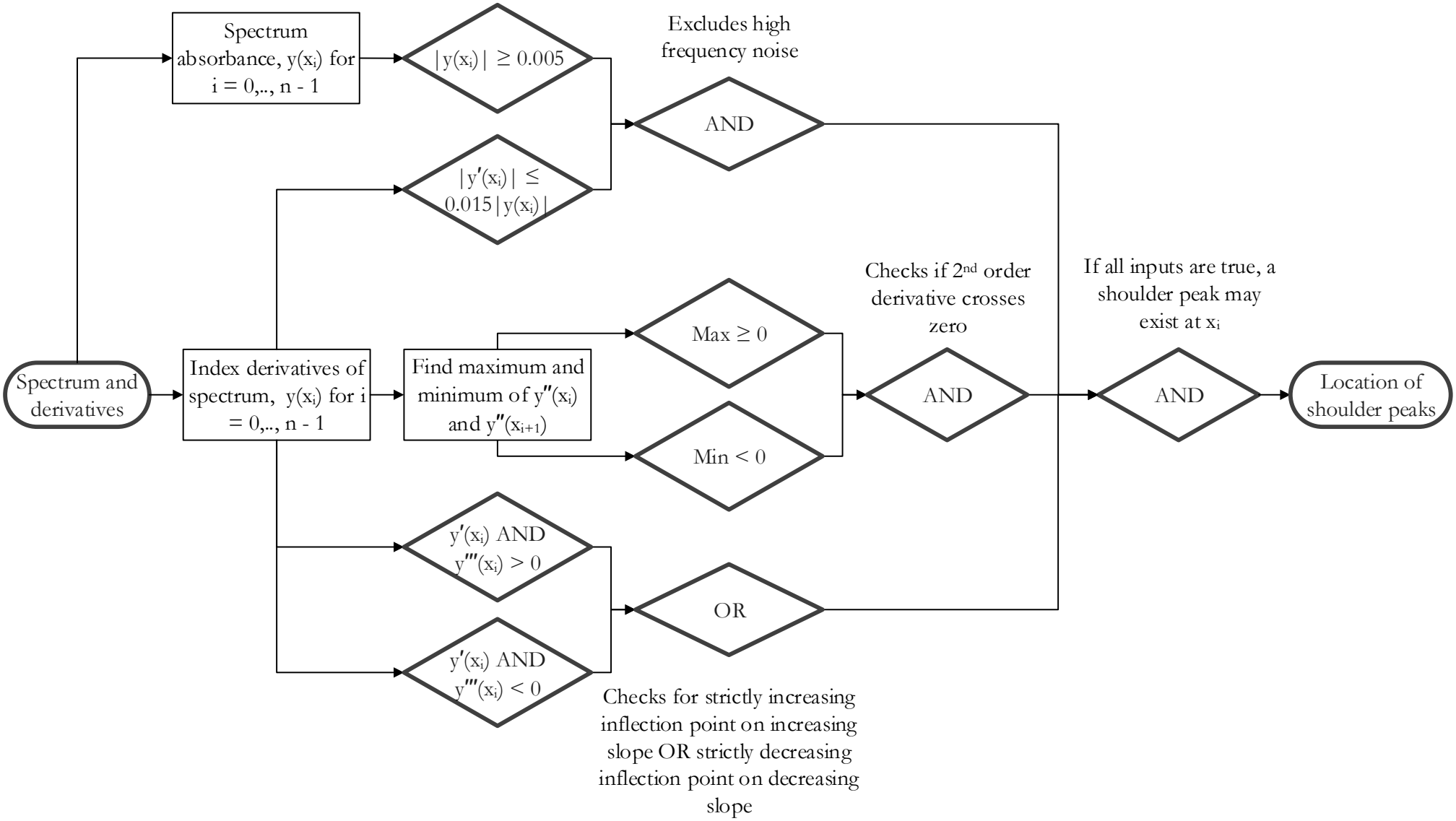

Figure 6: The *higher-order_differential_test* function. Up to the 3rd-order derivative is used to determine locations of possible shoulder peaks.

2.2.3 Synthetic Spectra for Software Validation

Synthetic spectra were produce and analysed in order to verify and quantify the predictive action taken by the software. These spectra were generated by superimposing a known, random noise distribution, a smooth baseline component and a distribution of asymmetric Gaussian and Lorentzian function.

Three different noise distributions were used, *viz.* a periodic random noise (PRN) distribution, a Gaussian distributed white noise (GWN) signal convoluted on a chirp pattern, and a periodic random noise distribution convoluted with a linearly ramped pattern (see Figure 7).

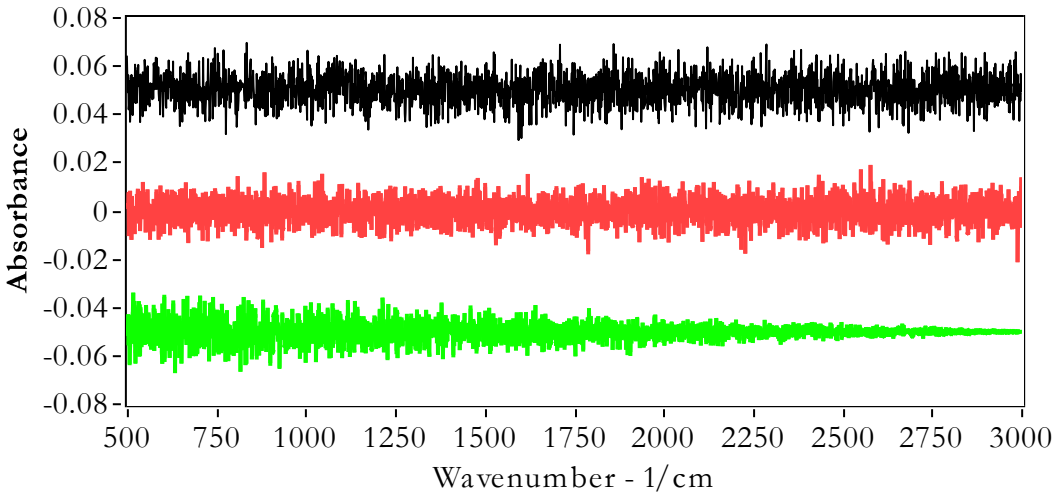

Figure 7: From top to bottom, periodic random noise (N1), Gaussian white noise (N2) and a ramped distribution of the periodic random noise (N3). Note, N1 and N2 are translated by ±0.05 on the ordinate for clarity.

The mean, standard deviation (σ), variance (σ^2) and the mean of the root-mean-square (RMS) power spectrum (PS) of the noise distributions are shown in Table 2. These statistical analyses were used to quantify the performance of the spectrum processing software with respect to each spectral component. The standard deviation is an indicator for the smoothing capability of the smoothing function.

Table 2: Statistical information of the noise distributions used in the validation of the software.

	Mean	σ	σ^2	Mean PS
N1	0.05	6.251×10^{-3}	3.908×10^{-5}	1.015×10^{-6}
N2	1.158×10^{-4}	4.948×10^{-3}	2.448×10^{-5}	9.791×10^{-9}
N3	-5.00×10^{-2}	3.636×10^{-3}	1.322×10^{-5}	1.006×10^{-6}

For synthetic baselines, two commonly seen trends were chosen and a third, complex trend was generated for validation. The two commonly observed trends are a monotonic increasing trend and a monotonic decreasing function. These functions were obtained by an exponential function with a power of 0.1 and the reciprocal of a hyperbolic tangent function. The third, smoothly varying, function was chosen as the hyperbolic tangent function superimposed on a sine wave. More complex functions could be devised, but this, however, would be without merit since experimental spectra with very complex, sharply increasing or decreasing baseline should be discarded as the analysis thereof may not yield any valuable information. Figure 8 indicates the three baseline trends simulated for method validation.

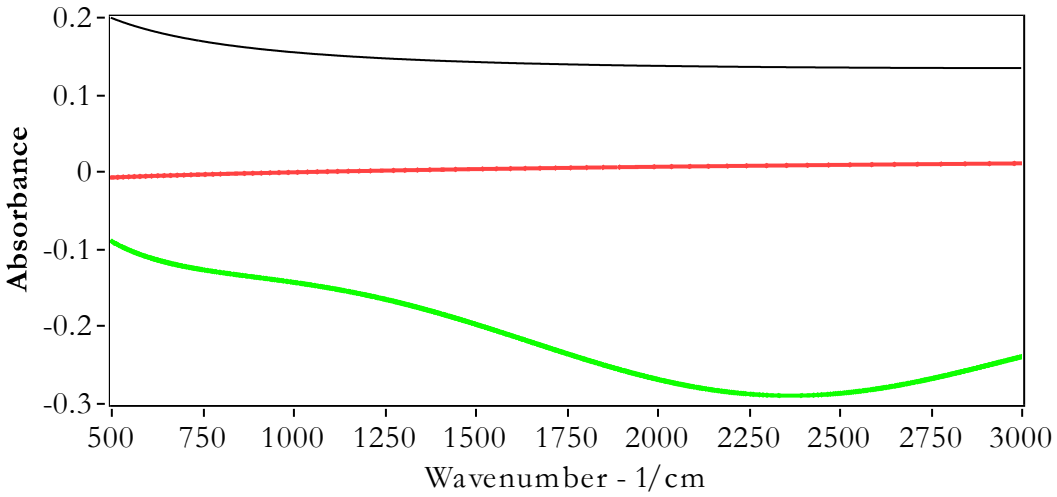

Figure 8: The baseline trends used for the synthetic spectra. From top to bottom, B1 is the reciprocal of a hyperbolic tangent function, B2 is an exponential function and B3 is a sinus wave convolved with the hyperbolic tangent function (B2). The functions are translated for clarity.

Pure, undistorted synthetic spectra were generated for method validation. These spectra were generated to include known problematic areas such as congested peak areas, asymmetry and lineshapes which are not pure Gaussian or Lorentzian distributions, but rather a combination of the two. These synthetic spectra can be seen in Figure 9. The spectra are translated for ease of identification.

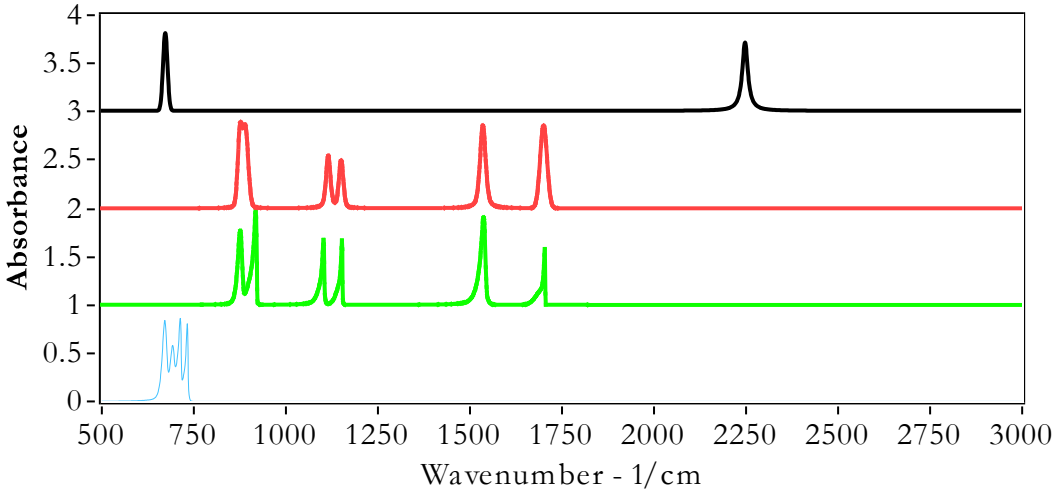

Figure 9: Synthetic spectra to test the peak detection, baseline removal and spectrum fitting software. From top to bottom, spectra are referred to as S1, S2, S3 and S4.

The spectra shown in Figure 9 have unique characteristics to test different aspects of the software. S1 has two peaks, a pure Gaussian (~670 cm^{-1}) and a pure Lorentzian, situated at the higher range of the scale. S2 has six peaks, two at ~875 – 890 cm^{-1} to test the higher order derivative test. This spectra contains only peaks that are of the Voigt function shape $(f \neq 0, 1)$. Test spectrum S3 is similar to S2. However, the congested peaks are well eluted and asymmetry is introduced. Spectrum S3 was designed to test the ability to handle congested peak areas.

2.2.4 Quantification of Infrared Absorbance Spectra

If the molar attenuation coefficient of a particular specie is known, and the species obeys Beer's law within the range of the investigation, one can quantify the result of a spectrum by solving for Equation (4). Assuming that a full set of calibration spectra at known concentrations is available for each species within the mixture to

be quantified, the following procedure can be followed to calculate the unknown quantities of the mixture. The procedure is discussed for the purpose of *in situ* quantification of time-resolved FTIR spectra.

1. A matrix of dimensions $n \times n$ must be generated with n being the number of components in the mixture.
2. n wavenumbers must be selected, each of these wavenumbers corresponding to a peak of sufficient absorbance of each component in the mixture. The uniqueness of the selected peaks is directly related to the uniqueness of the solution. For example, if all the wavenumbers selected, correspond to one and only one component with non-zero absorbance in the band and no two wavenumbers correspond to the same absorbing species, the solution will be unique. The selection of wavenumbers to satisfy this condition is near impossible, however, the fewer non-unique selections will consequently reduce the number of possible solutions.
3. Steps 1 and 2 should be done prior to data analysis. The solution of any given spectrum can then be obtained by solving the linear set of equations shown in Equation (30).

$$\begin{bmatrix} a_{ij} & \cdots & a_{in} \\ \vdots & \ddots & \vdots \\ a_{nj} & \cdots & a_{nn} \end{bmatrix} \cdot \begin{bmatrix} x_{ij} \\ \vdots \\ x_{nn} \end{bmatrix} = \begin{bmatrix} y_i \\ \vdots \\ y_n \end{bmatrix} \qquad (30)$$

Here i represents the selected wavenumbers and a_{ij} represents the absorbance of a known concentration of specie j at wavenumber i. In Equation (30) x_i and y_i are the absorbance of specie j solved for, and the experimentally determined absorbance at wavenumber i, respectively. The concentration of the absorbing specie (at wavenumber i) can then be calculated using Beer's law.

With modern day computational power it is almost irrelevant to select only n wavenumbers to solve for n components. Essentially, Equation (4) in section 2.1.1

on page 6 holds for any wavenumber over the entire range. A spectrum obtained from a mixture of absorbing components is equal to the sum of the individual components' spectrum over the same range. The method employed for qualitative and quantitative analysis utilise the same Levenberg-Marquardt non-linear solving function used for determining the lineshape parameters. Even though the set of equations are linear. In essence, the function minimise Equation (31).

$$argmin\ [\bar{S}_{exp} - (x_1 \cdot \bar{S}_1 + x_2 \cdot \bar{S}_2 + \cdots + x_i \cdot \bar{S}_i)\ ] \qquad (31)$$

The symbols in Equation (31) are S_{exp} signal or spectrum acquired from the unknown sample, x_i refer to the fraction of the normalised pure component spectrum and S_i represents the normalised pure component spectrum. The function therefore solves for the fraction of each of the normalised pure component spectrum such that the sum of these spectra fit the experimental spectrum.

Figure 10 is a flow diagram of the logic behind *in situ* quantification of experimental, time-resolved infrared data. The logic is essentially very simple, the spectrum is corrected with respect to detrending and noise reduction, Equation (31) is optimised and each component is quantified by means of Beer's law.

2.2.5 Summary of Software Functionality

Although the goal of the developed software is to automate the analysis of time-resolved infrared spectra, several steps must be taken beforehand to enable the automation of such data. These steps are as follow:

1. At least one pure spectrum is needed for each component in the anticipated product mixture. Each of the components' spectra are fitted with the lineshape fitting program to obtain the fitting parameters of the Voigt function. This step is done once, or to the satisfaction of the user.
2. Once all the linshape fitting parameters are known, one must provide the molar attenuation coefficient for each possible component. This is necessary

for the purpose of quantifying the spectral data and not for the purpose of deconvolution. A function is coded to automate this procedure for large data sets.

3. The previously mentioned steps provide the fitting parameters for the function that quantifies the input spectrum.

Further optimisation of operating parameters by means of repetitive tests on different product mixtures, rectifying the code to be generic regardless of input file format etc. and ease of use is beyond the scope of this text.

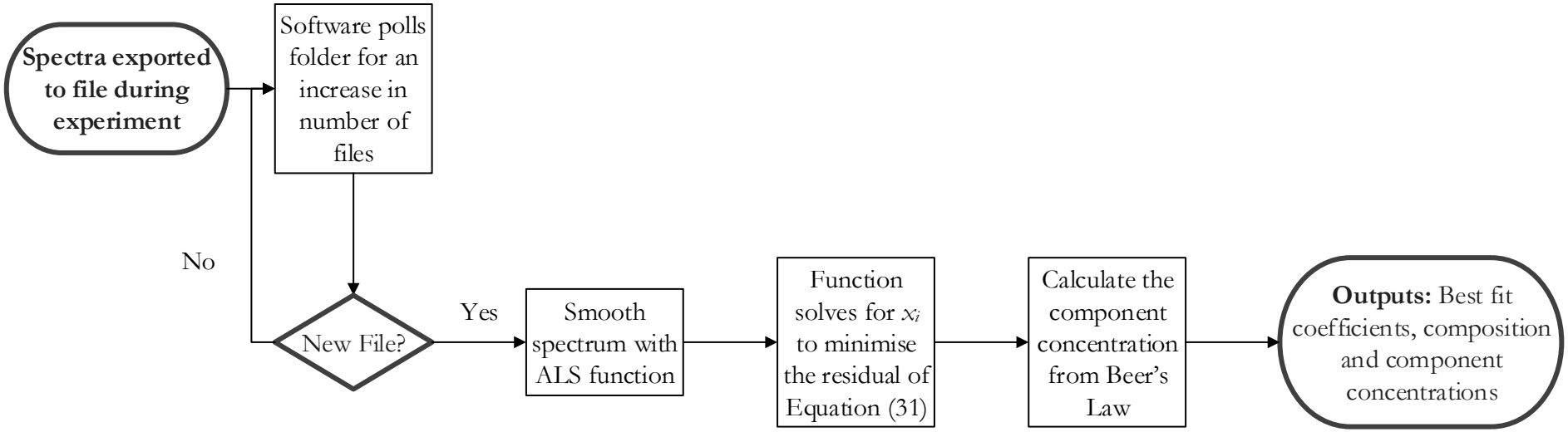

Figure 10: Flow diagram of the simplified logic for solving experimental spectra with respect to composition and concentration.

2.3 Results and Discussion

Performance criteria were set in advance, to enable comparison of each method with all other. Three performance criteria were identified as the predominant indicators:

1. **Execution time** is important with respect to time resolved data capture, and serves as an indication of memory- and CPU usage.
2. **Standard deviation** of baseline areas. The standard deviation, together with the median of the corrected baseline is an indication of the noise of the signal. A reduction in noise of the original spectra has a proportional decrease in the standard deviation of the corrected baseline and is therefore a quantifiable indication of the amount of smoothing done by the technique.
3. **Signal-to-Noise Ratio (SNR)** is a ratio of the power spectrum of the desired, signal spectrum versus the power spectrum of the unwanted noise. A high SNR indicates a dominant signal area with respect to noise. A comparison of the SNR of the original spectrum and the corrected spectrum, as well as visual inspection, were used to evaluate the effectiveness of a technique's smoothing ability, and its peak discrimination ability.

2.3.1 Processing Software Validation: Preprocessing of Synthetic Spectra

The spectral processing software developed was applied to synthetically generated spectra in order to quantify its capabilities and the extent of errors, if any. A statistical analysis was done on the resulting absorbance signal and then compared to the original statistical analysis of each component, noise, baseline and signal, of the synthetic spectrum. These spectra were generated with a wavenumber interval of 1, from 500 cm^{-1} to 3000 cm^{-1}, similar to that of an experimentally obtained spectrum The signal-to-noise ratio (SNR) of the synthetic spectra, N1B1S1, N2B2S2, N2B3S2 and N3B3S4, were 2.19, 774, 774 and 3.51, respectively.

2.3.1.1 Asymmetric Least Squares Method

The asymmetric least squares (ALS) method has two tuning parameters, *viz.* λ for the amount of smoothing, and d, the order of the derivative, which penalises high frequency disturbances. The lower λ is, the more it smooths. Values were increased by three orders of magnitude. All analyses were done with a first order penalty $(d = 1)$, as suggested by Eilers (2003), unless stated otherwise.

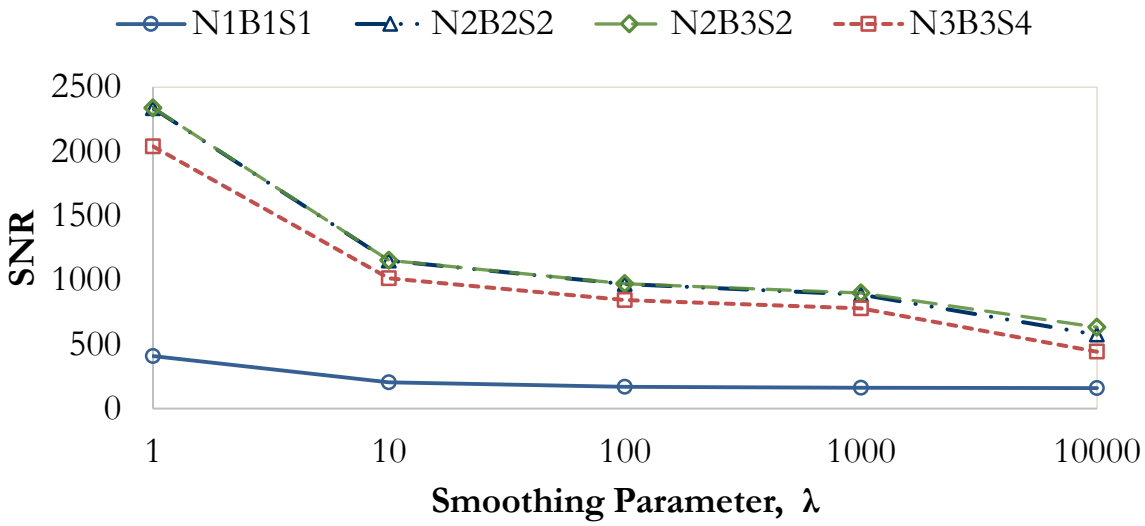

Figure 11: The signal-to-noise ratio of the processed, by means of the ALS method, synthetic spectra. SNR for the original spectra were 2.19, 774, 774 and 3.51, respectively.

Figure 11 shows the SNR of all the processed synthetic spectra as a function of the smoothing parameter. The ALS method performed very well with respect to SNR development, even when little smoothing was applied ($\lambda \geq 1000$),. The only occurrences where the SNR after processing were less than the original, are for N2B2S2 and N2B3S2, with smoothing parameters greater than 1000.

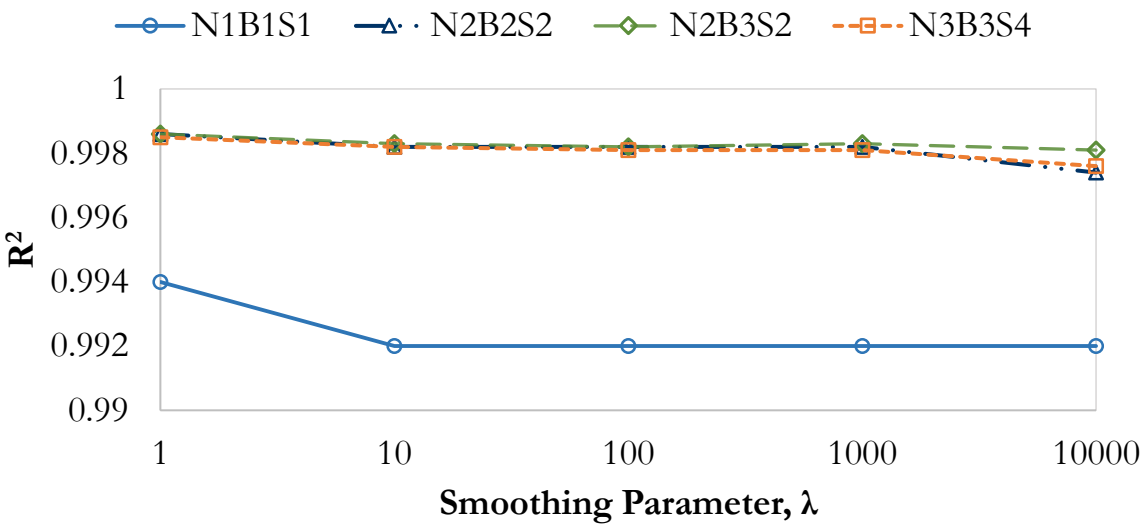

Figure 12: R^2 values of the processed, by means of the ALS method, spectra with respect to the synthetic signal spectra (without the addition of noise or a baseline).

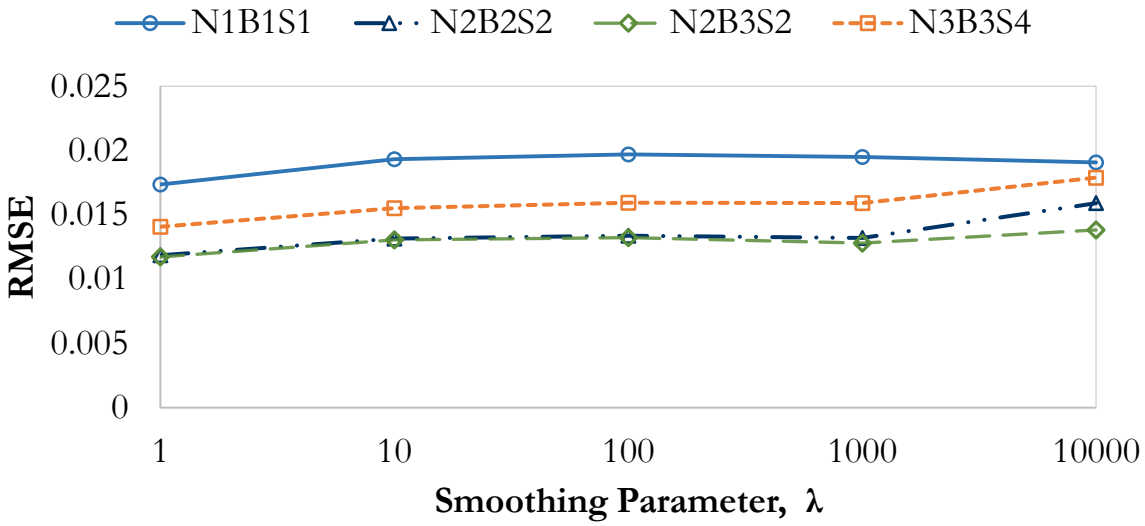

Figure 13: RMSE results after processing with the ALS method. The residue is that of the processed spectra with respect to the pure signal spectra (without the addition of noise or a baseline).

Figure 12 and Figure 13 are indicators of the goodness-of-fit, R^2 and RMSE, respectively, of the processed spectra with respect to the original signal spectra of each synthetic spectrum. An R^2 value of above 0.99 was considered a very good fit.

With reference to Figure 13, the RMSE values confirm this criterion with no processed spectrum exceeding 0.002 for any of the chosen smoothing parameters.

2.3.1.2 Noise-Median Method

The NM method was evaluated at four different initial window sizes. These window sizes were, 4, 10, 20 and 50. The choice of window size is dependent on the amount of smoothing desired, as well as the width of the broadest peak, or group of peaks, in the spectrum to be analyzed. Since a weight vector, which discriminates against peaks, was applied to all the methods, the choice of window size is not as crucial with respect to peak width.

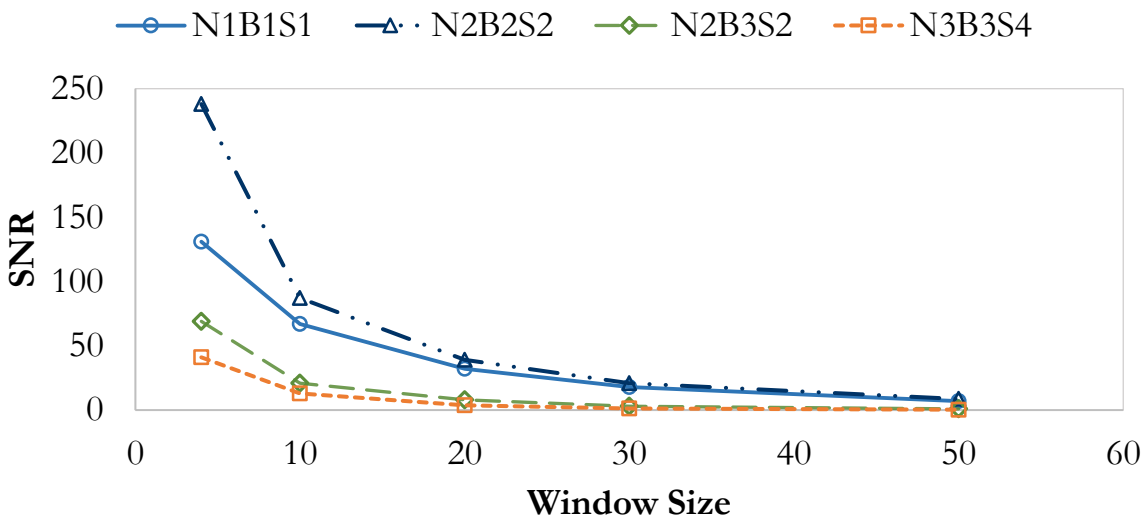

Figure 14: SNR after processing the synthetic spectra by means of the NMM as a function of the window size.

The SNR of the synthetic spectra, processed by means of the NMM can be seen in Figure 14. The SNR is strongly affected by the window size used, this is expected since the median approached the exact value of the original spectrum, as the window size approaches unity. One should keep in mind that the window size refers to the initial parameter setting to determine the maximum number of extrema in this initial window (refer to Section 2.1.2 on page 7 for a detailed explanation). Thereafter, the

window size is changed such that each window includes the same number of extrema.

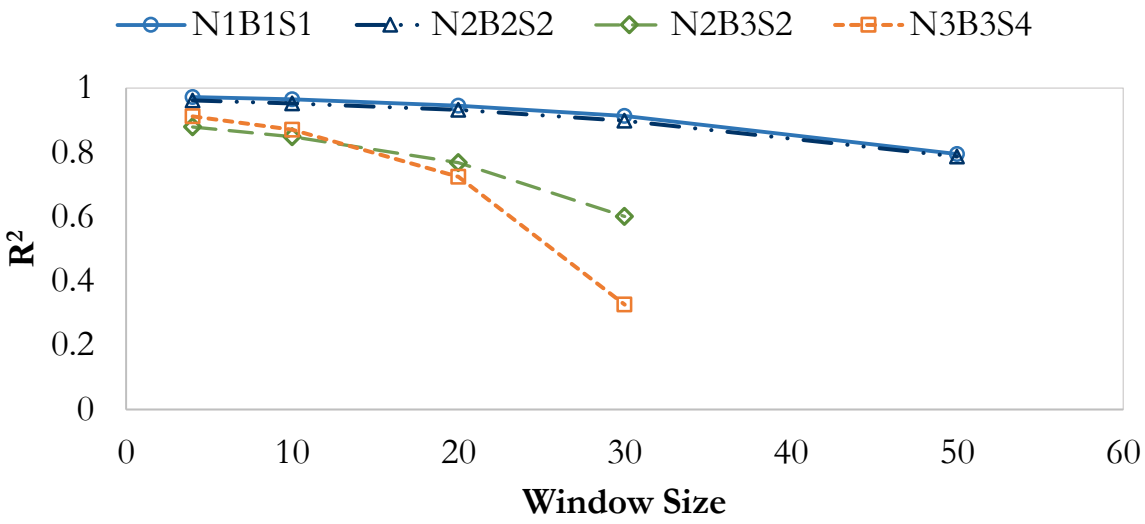

Figure 15: R^2 indicators of the goodness-of-fit for the NMM processed spectra with respect to the signal spectra.

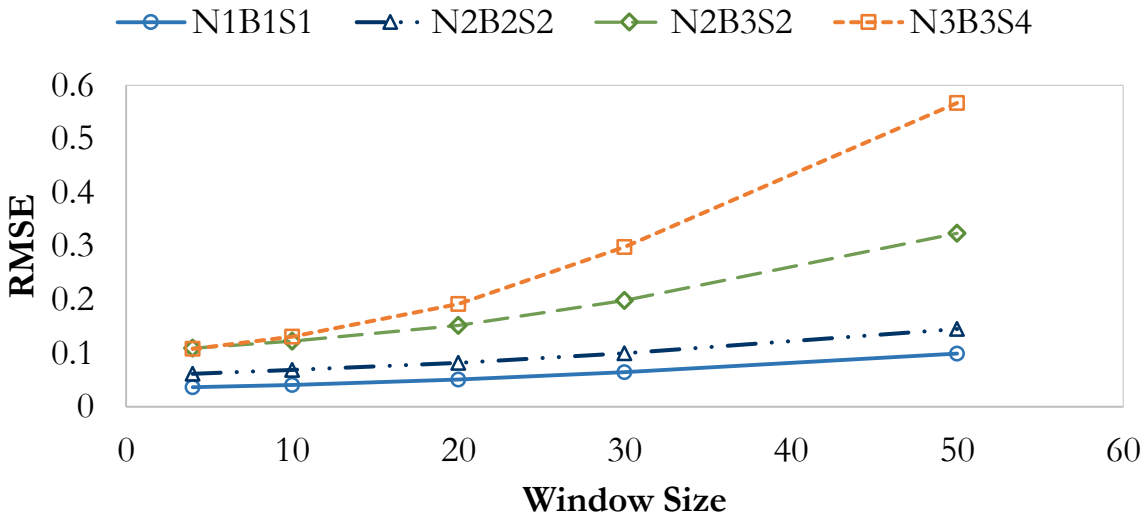

Figure 16: RMSE indicator of the goodness-of-fit for the NMM processed spectra with respect to the signal spectra.

The R^2 and RMSE indicators (Figure 15 and Figure 16, respectively) show a strong relationship between the window size and the baseline shape. Baselines B1 and B2 are strictly increasing and strictly decreasing, respectively, which this method seems

to handle much better than other baseline function (B3). The R^2 indicators for a window size greater than 30 provided negative values, indicative of a very poor fit.

2.3.1.3 LOWESS/Robust Baseline Estimation Method

Initially only the LOWESS procedure was tested on the synthetic spectra. Good performance of this procedure should, intuitively, indicate better results when processed by the RBE method. The function used for evaluating the LOWESS procedure (Hoerman, B: 2006) accepts a weight parameter, *q*, which is a fraction of the total number of elements of the input spectrum. Weight parameters in excess of 0.5 are not considered since the solution cannot be considered "locally weighted".

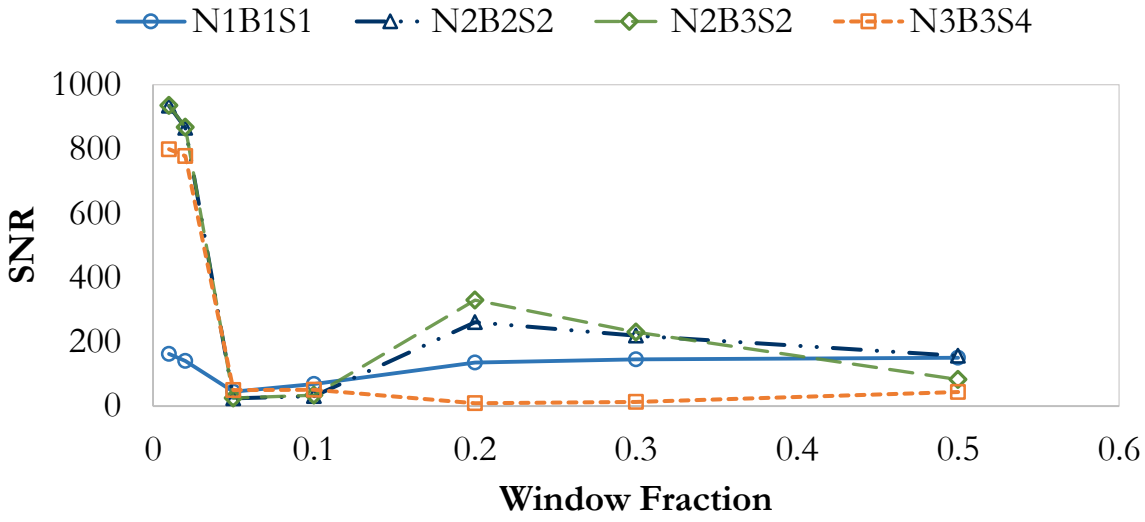

Figure 17: SNR development as a function of the fraction of elements used for linear regression by the LOWESS procedure.

No definite trend is visible in the development of the SNR (Figure 17) after processing by means of the LOWESS procedure. However, it is certain that the procedure is not suited for a window fraction of 0.1. The procedure does show an increase in SNR for all processed spectra with a window fraction of 0.01. The SNR of spectrum N1B1S1 does show a steady increase for larger window fractions. This could be attributed to the baseline having a slow, steady slope, much like the linear

regression used by the LOWESS procedure. However, the actual cause is still unclear since the SNR is not associated with the baseline.

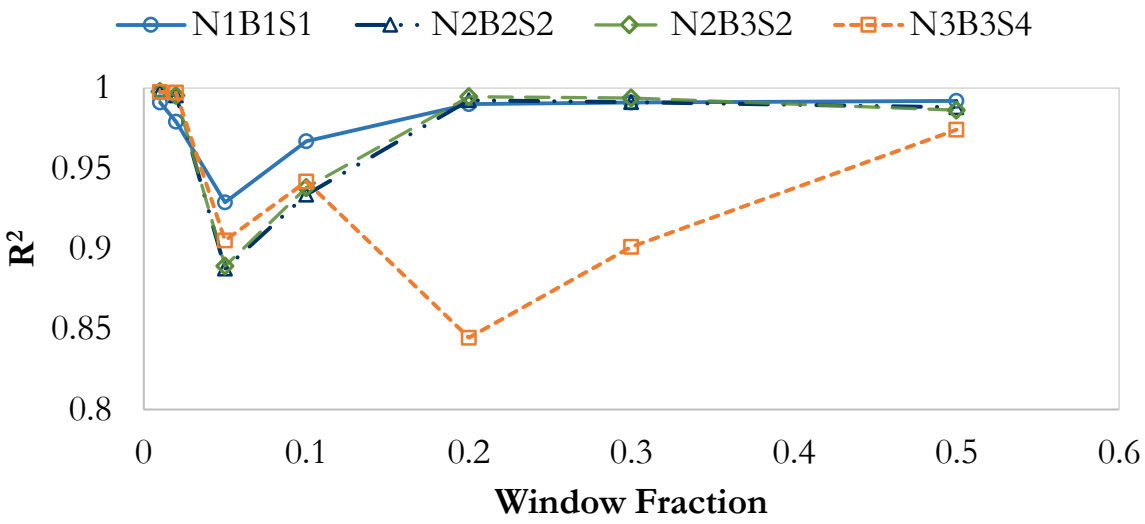

Figure 18: Goodness-of-fit indicator, R^2, evaluated from the LOWESS method solution with respect to the signal spectra (without noise or baseline function).

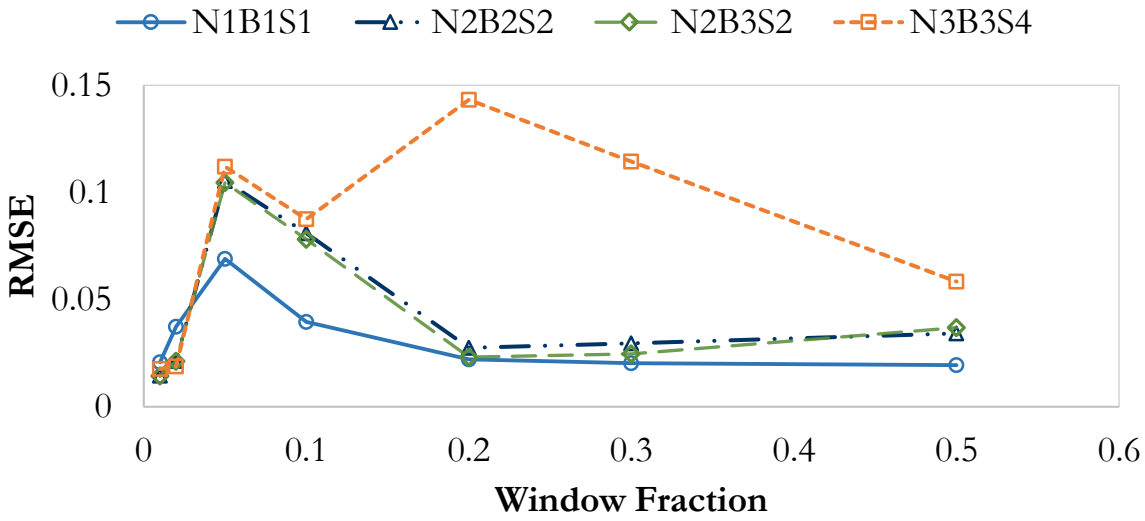

Figure 19: RMSE goodness-of-fit indicator as a function of window fraction, evaluated with the LOWESS procedure.

The LOWESS procedure produced good fits to the signal spectra after smoothing and baseline removal. However, erratic results were obtained for congested peak areas (S4), which indicates the procedure's dependence on the number and position of peaks. The procedure provided the best result using a window fraction of 0.01

for all spectra, apart from N1B1S1, which provided a better fit with increasing window fraction. This is explained by the slow varying, strictly increasing B1 baseline and shows that the choice of window fraction is important when evaluating spectral data with different baseline trends.

2.3.1.4 Comparison of the Pre-processing Methods

All methods analysed provided a relatively good fit, for at least one of the parameters tested, to the synthetic spectra. The best parameter for each method was chosen for evaluation, except for the ALS method. A conservative choice for the smoothing parameter was made, since this method provided very good results with less smoothing and will consequently reduce discrimination against peaks.

The processed spectra of one of the synthetic spectra are shown in Figure 20 for illustrative purposes. All the processed spectra are shown, enlarged, in Appendix 5.1 on page 100. In these figures, the black line represents the original, synthetic spectrum, the red dots indicate the detected peaks, the solid red line is the spectrum solution by means of the ALS method, the dashed blue line indicates the NMM solution and the solid green line indicates the LOWESS solution.

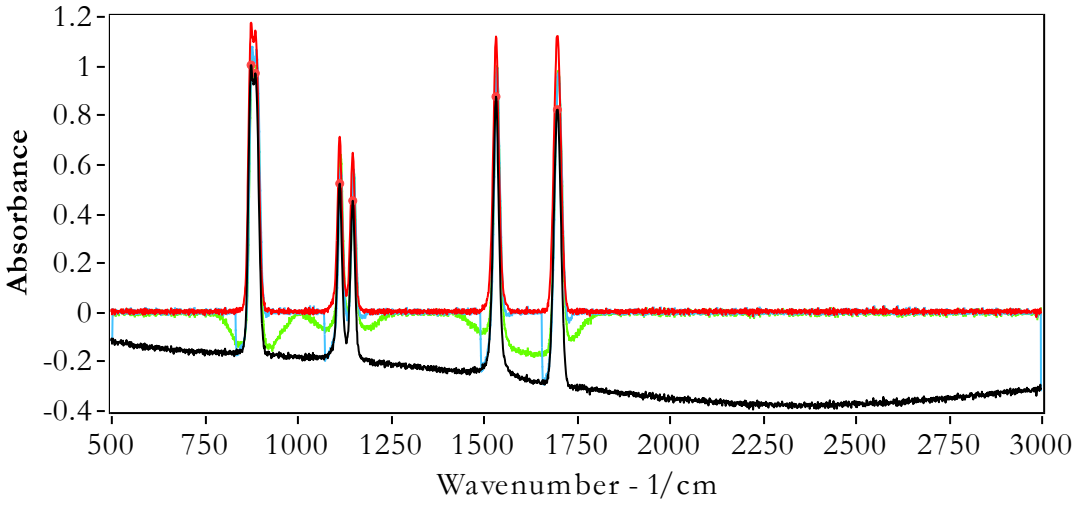

Figure 20: Spectrum N2B3S2 with detected peaks indicated and processed results for all methods. The smoothing parameter for the ALS method was 10, the NMM window size 4 and the LOWESS window fraction 0.05.

Figure 20 clearly shows the large effect window fraction has on the LOWESS procedure. This effect is cumbersome since this parameter needs to be set before processing an on-line set of data.

Table 3 shows a comparison of the three processing methods tested. The SNR was evaluated as the smallest factor a method obtained for the increase in SNR. Average values of the R^2 and RMSE indicators for the four spectra processed are shown. The average execution time of all spectra and parameters are reported.

Table 3: Comparison of minimum increase in SNR, average R^2, average RMSE and average execution time of the three spectrum processing methods.

	$\left(\frac{SNR_{Processed}}{SNR_{Sig}}\right)_{Min}$	R^2	RMSE	Exe. Time (ms)
ALS ($\lambda = 10$)	1.49	0.997	0.0138	2530
NMM ($W = 4$)	0.09	0.931	0.0788	45
LOWESS ($q = 0.01$)	1.21	0.996	0.0169	3870

The results from Table 3 clearly show that the ALS and LOWESS methods outperform the NM method, with respect to smoothing and baseline tracking. The NMM is a promising processing method when execution time is critical. The NMM could, however, be improved by implementing a different baseline estimation method under peaks. Even though the LOWESS procedure shows very good smoothing and baseline tracking, the method is too slow when considering processing of time-resolved data. The ALS method is also rather slow. However, it is well within the 5.4 s interval between consecutive time-resolved spectra, which enables on-line processing of experimental data. The ALS method also proves to be the least sensitive to the characteristics of the noise, baseline and signal.

2.3.2 Infrared Absorbance Lineshape Fitting

The lineshape fitting function was applied to the synthetic spectra in order to validate the accuracy of the fitted parameters. Synthetic signals S1, S2, S3, and S4 were solved

with no noise or baseline trend added. The same signals were then solved with noise and baseline trends. These spectra were pre-processed with the ALS processing function prior to fitting. The fitted parameters for all the evaluated spectra can be seen in Appendix 5.2 on page 105.

All fitting algorithms fitted the exact parameters very well for signal spectra S1 and S2 with and without noise and a baseline trend. The TRDL, LM and asymmetric LM algorithms were within 0.1 cm^{-1} with respect to the peak centre for these signals. The largest deviation in peak area was for peak 2 in signal S1. This is a pure Lorentzian peak and was not solved as such. The deviation in the Voigt parameter, *f*, was also the largest for this peak.

Substantial deviations from the exact parameters were noticed for signal S3 and spectrum N1B1S3. The algorithms performed well with respect to peak position. However, the area and FWHM were incorrectly fitted in most cases. The asymmetric LM algorithm predicted the asymmetric parameter accurately.

The predictions for signal S4 and the corresponding spectrum N3B3S4 follow the same trend as with signal S3. In this instance, the peak centres were predicted to within 2 cm^{-1} of the exact value. The peak area and FWHM was predicted with large variances and the Voigt parameter and asymmetric parameter was predicted with reasonable success.

Even though some variation to the exact solution exists, the actual fit to the data is the most important for the purpose of this investigation. The best fitted solution was evaluated with respect to the exact signal to determine the goodness-of-fit. The results for the residue of each solving method can be seen in Figure 21.

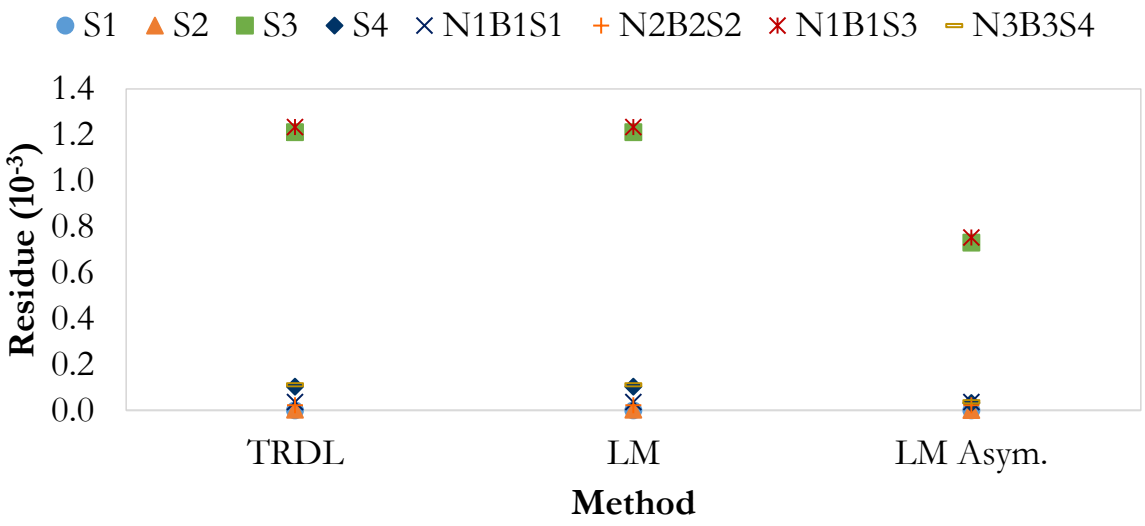

Figure 21: The residue of the best fit parameters for each synthetic spectrum, with and without noise and baseline components.

It is clear from Figure 21 that signal S3 was the most challenging to solve for all methods used. The asymmetric solution shows a considerable decrease in the residue of signal S3. The solutions of both the TRDL and LM methods are comparable with respect to the residue.

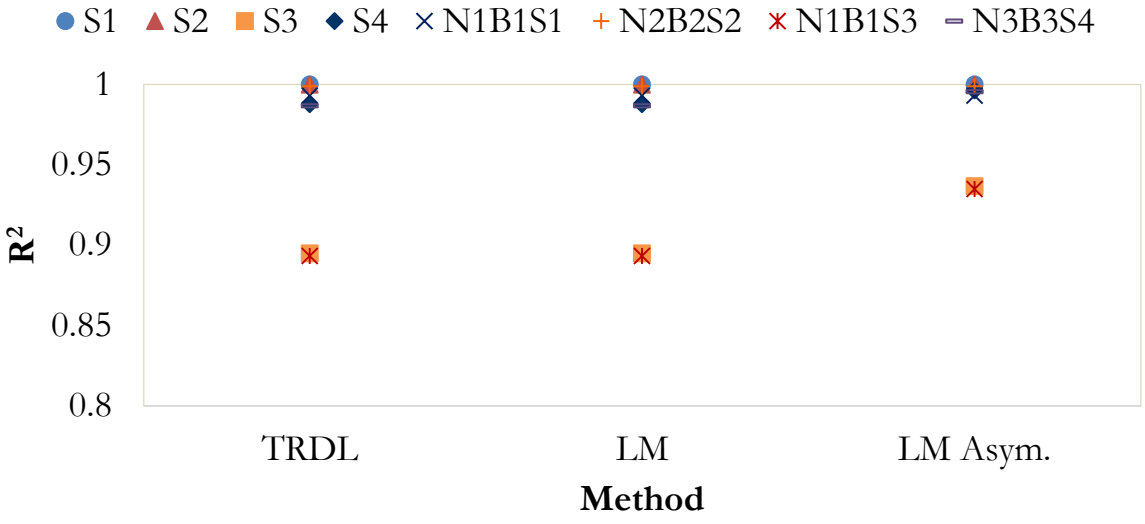

Figure 22: R^2 goodness-of-fit indicator for the best fit parameters of the TRDL, LM and asymmetric LM solutions.

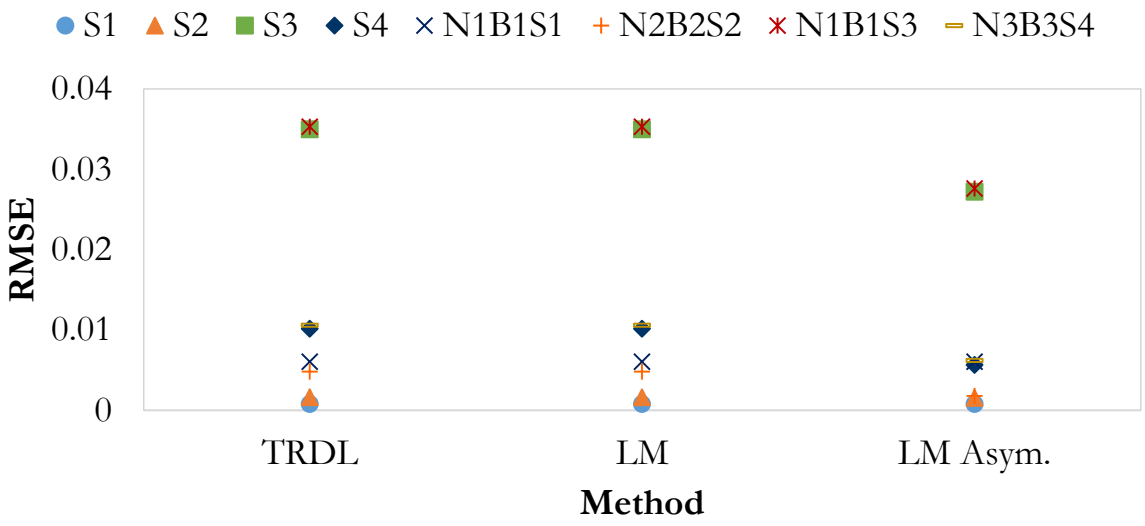

Figure 23: RMSE goodness-of-fit indicator for the best fit parameters of the TRDL, LM and asymmetric LM solutions.

The goodness-of-fit indicators, R^2 and RMSE, show promising results with respect to all analysed spectra, except for signal S3 (refer to Figure 22 and Figure 23). It is believed that the combination of asymmetry, peak area and FWHM of the peaks in this spectrum is the cause of the inaccurate solution. Figure 24 is an example of the residue (dashed, grey line) of an asymmetric peak (solid black line). The asymmetric parameters chosen for these synthetic spectra were large in comparison to what one might find in real data.

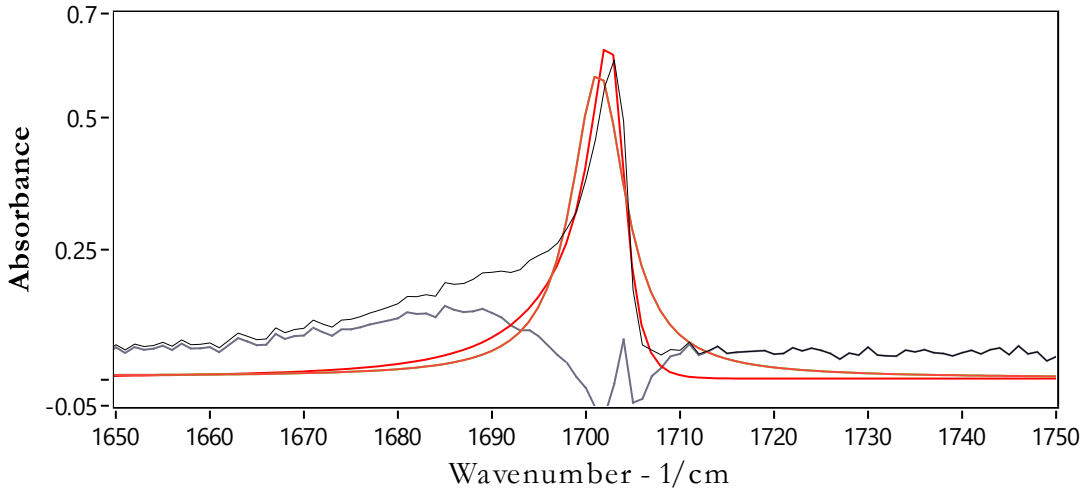

Figure 24: An example of an asymmetric peak in signal S3. The solution shows a definite problem with respect to severe asymmetry in peaks.

From the reviewed results it is certain that the TRDL and LM algorithms provide accurate results and are comparable to one another. The asymmetric LM solution performs the best when peaks with a small asymmetric tendency exist. The asymmetric LM solution should, however, perform better in all instances since it receives the best fitted parameters of the symmetric LM solution as its initial parameters.

The final criterion for evaluating the solution methods is execution time. The execution time of these solution functions is heavily dependent on the complexity of the equation to be solved, as well as the number of parameters to be solved for.

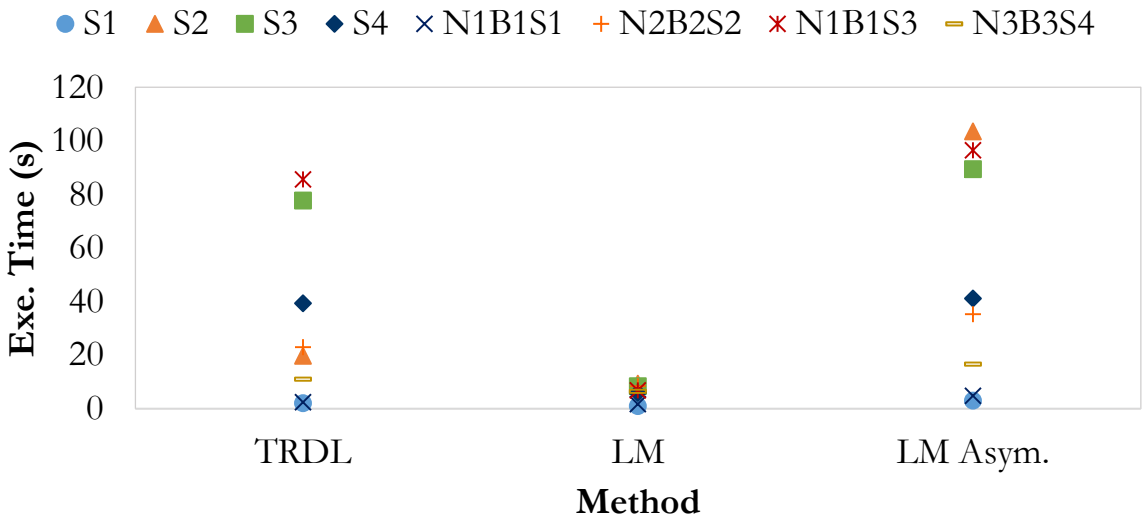

Figure 25: Execution time, for each evaluated spectrum, of the three algorithms considered.

Figure 25 indicates the execution time of each method considered. The symmetric LM method shows superior execution time compared to the TRDL method, even for signal S3. For all other performance indicators, residue, R^2 and RMSE, the LM method performed equally well with respect to the TRDL method. The addition of asymmetry to the LM solution indicates a definite impact on execution time, possibly due to both, the addition of a fifth parameter per peak as well as an increasingly complex mathematical function.

2.4 Conclusions and Recommendations

A method for the qualitative and quantitative analysis of time-resolved FTIR spectra was proposed and tested on the thermal decomposition products of PTFE. The method is to be packaged as a software bundle for use with relevant pyrolysis reactor systems such as TGA-FTIR analysis.

Pre-processing techniques were evaluated with respect to an improvement in signal-to-noise ratio (SNR) and baseline tracking. These techniques were also scrutinized for robustness of parameter selection and discrimination against desired signal peaks. Execution time of the preprocessing and analysis software was considered important, since the software bundle is intended for *in situ* data capturing and analysis. Three pre-processing techniques were evaluated based on positive reviews in the literature. These techniques are the asymmetric least squares (ALS) method, noise-median method (NMM) and an adapted LOcally WEighted Scatter plot Smoother (LOWESS) method. The LOWESS method can be expanded to include additional robustness and better baseline tracking as described by Ruckstuhl *et al.* (2001). However, the LOWESS procedure proved to be very slow and the expansion thereof would introduce additional processing time. The robust baseline estimation method presented by Ruckstuhl *et al.* (2001) was therefore not considered.

The ALS method proved to be the overall best performing method with respect to smoothing, baseline tracking, robustness, and peak discrimination. This method is slow (~2500 ms) when compared to the noise-median method. However, the execution time is still well within the limit imposed (< 5000 ms). The ALS method successfully improved SNR by a minimum factor of ~ 1.5 for the synthetic spectra tested. This method also produced the best results for baseline tracking. Based upon the findings, pre-processing of all spectra obtained from FTIR analyses were done by means of the ALS method.

An asymmetric lineshape, for the fitting of infrared spectra, was introduced for obtaining a mathematical function for the processing and analysis of spectra. The method introduces a bounded asymmetric function to a pseudo-Voigt function. It was found that the introduction of asymmetry could compensate for shoulder peaks that could not be solved for. Even though this is not scientifically correct, it enables accurate mathematical solutions without the introduction of additional functions to handle shoulder peaks.

The fitting of spectral data is needed to describe pure component spectra mathematically. The fitted function can then be used for fitting to experimental data and consequently provide *in* situ qualitative and quantitative data. In total, five parameters were fitted for each peak found. These parameters were optimally solved for by utilising the Levenberg-Marquardt (LM) LabVIEW Library function. Another variation of this nonlinear solver (the Trust-Region DogLeg (TRDL) algorithm) was also tested but found to be inferior to the LM solver. The asymmetric function introduced additional processing time. However, no results were evaluated on the processing time for fitting spectra since it is a once-off task prior to experimental work.

If a full set of calibration spectra is available, qualitative and quantitative analyses can be done *in situ*. The LM non-linear solver function is used to solve the constrained set of linear equations for the number of components present. However, this step is only possible if high quality calibration spectra are available and there are minimal deviations from Beer's law.

The method proposed was found to be viable with respect to accuracy of fitting infra-red spectral data and computational time. Additional testing is required before the software can be implemented as part of a process control philosophy. It is not possible to prove or disprove the use of such a method as part of a control system without a comprehensive set of calibration spectra.

3 Software Implementation: PTFE Pyrolysis as Test Case

3.1 Literature

Thermal degradation and pyrolysis of polytetrafluoroethylene (PTFE) has been studied by numerous researchers since the original work of Lewis & Naylor (1947). Chemical recycling of PTFE is of interest since it is thermally very stable, chemically inert, and also physically stability (Lewis & Naylor, 1947 and Simon & Kaminsky, 1998). These desired properties of PTFE and the fact that PTFE is not melt-processable, have resulted in buildup of unacceptably large amounts of PTFE waste (Meissner *et al.*, 2004). It is evident that the chemical recycling of waste PTFE would be environmentally advantageous.

The pyrolysis of PTFE has been studied in different reactor assemblies and processes, ranging from quartz assemblies (Morisaki, 1978 and Bhadury *et al.*, 2007), iron pipe assembly (Lewis & Naylor, 1947), nickel pipe reactor (Meissner *et al.*, 2004), fluidized bed reactor (Simon & Kaminsky, 1998) and by means of thermal gravimetric analysis (Morisaki, 1978 and Szekely *et al.*, 1987). In the work of these various researchers further process parameters are not consistent. These include the reactor temperature and pressure, gas atmospheres, gas flow rate, and transport mechanisms.

A common feature of all of the studies mentioned is the distribution of pyrolysis products and their variation as a function of reactor temperature and pressure.

3.1.1 Selectivity of Pyrolysis Products

All of the previously mentioned research studies indicate the formation of tetrafluoroethylene (TFE), hexafluoropropylene (HFP) and octafluorocyclobutane (OFCB) as the major constituents of the pyrolysis product gas. The composition of these products, however, vary significantly with respect to temperature and pressure, as well as the method or process used.

Other products, in varying fractions, have been reported as perfluoroisobutylene (PFIB), hexafluoroethane (HFE), octafluoropropylene (OFP), tetrafluoromethane (TFM), 1- and 2-octafluorobutene (1-OFB and 2-OFB, respectively) and in the cases where quartz reactors were used, low fractions of carbon monoxide, carbon dioxide and silicontetrafluoride were detected.

Tetrafluoroethylene wase found to be most abundant at lower temperatures and low pressures. Lewis & Naylor (1947) reported a weight fraction, of TFE, of 0.97 at 600 °C which substantially decreases with an increase in pressure. The pressure range investigated was 5 – 760 mm Hg. They also reported a slight decrease in TFE yield with at a reaction temperature of 700 °C. The work of Bhadury *et al.* (2007) and Meissner *et al.* (2004) supports the findings of Lewis & Naylor.

The formation of HFP is favoured at high temperatures. Meissner *et al.* reports weight fractions of above 0.80 at temperatures exceeding 700 °C and relatively low pressures (< 400 mm Hg). Bhadury *et al.* and Lewis & Naylor also report an increase in HFP formation at elevated temperatures.

Octafluorocyclobutane yield is favoured at lower temperatures (600 – 700 °C) but at pressures in the region of 100 – 200 mm Hg (Meissner *et al.*, 2004). Lewis & Naylor reports weight fractions of 0.584, calculated by difference, of OFCB at 600 °C and 760 mm Hg, while Bhadury *et al.* also reported the preference toward TFE and OFCB at these conditions.

High weight fractions of perfluorinated butenes were reported at temperatures above 800 °C and increased pressures. At even higher temperatures, the presence of unsaturated fluorocarbons is not favoured and the formation of perfluorinated alkanes and carbon is observed (Meissner *et al.*, 2004 and Bhadury *et al.*, 2007).

3.1.2 Properties of Pyrolysis Products

It has been reported that most of the light end products are non-toxic and harmless to humans (Simon & Kaminsky, 1998). For instance, OFCB has been used for medicinal purposes and in the food industry (Meissner *et al.*, 2004). However, it must be stressed that some of the products of pyrolysis, the perfluorinated butenes in particular, are highly toxic and extremely dangerous to humans (Simon & Kaminsky, 1998). Instances of TFE and HFP exploding violently, have been reported (Urben, 2006: 216).

3.2 Experimental

The apparatus, the experimental design and methods pertaining to the validation of the software are in the text which follows.

3.2.1 Apparatus

3.2.1.1 PTFE Fast Pyrolysis Reactor System

An in-house developed reactor system was available for the vacuum pyrolysis of PTFE. The reactor system is shown in Figure 26 and is capable of pyrolysing up to 30 grams of waste PTFE. The reactor is heated with a resistive heating furnace and controlled at temperature by means of a National Instruments CompactRio real-time controller (NI cRIO-9024 controller, mounted on a cRIO-9118 chassis). The reactor system is semi-automated and is constantly monitored for safety and data acquisitioning purposes. Temperatures exceeding 200 °C were measured with Type K thermocouples, while all other temperature measurements were made with Type T thermocouples. Acquisitioning of the thermocouple measurements was done with a NI 9213, 16 channel thermocouple module. The NI 9213 module provides onboard cold junction compensation and auto-zeroing capabilities. Pressure measurements were acquired by means of a NI 9207 current input module and were measured with Wika Instruments® S-10 and UT-10 pressure transmitters. The pressure transmitters are calibrated for a range of 0 – 6 bar (abs.).

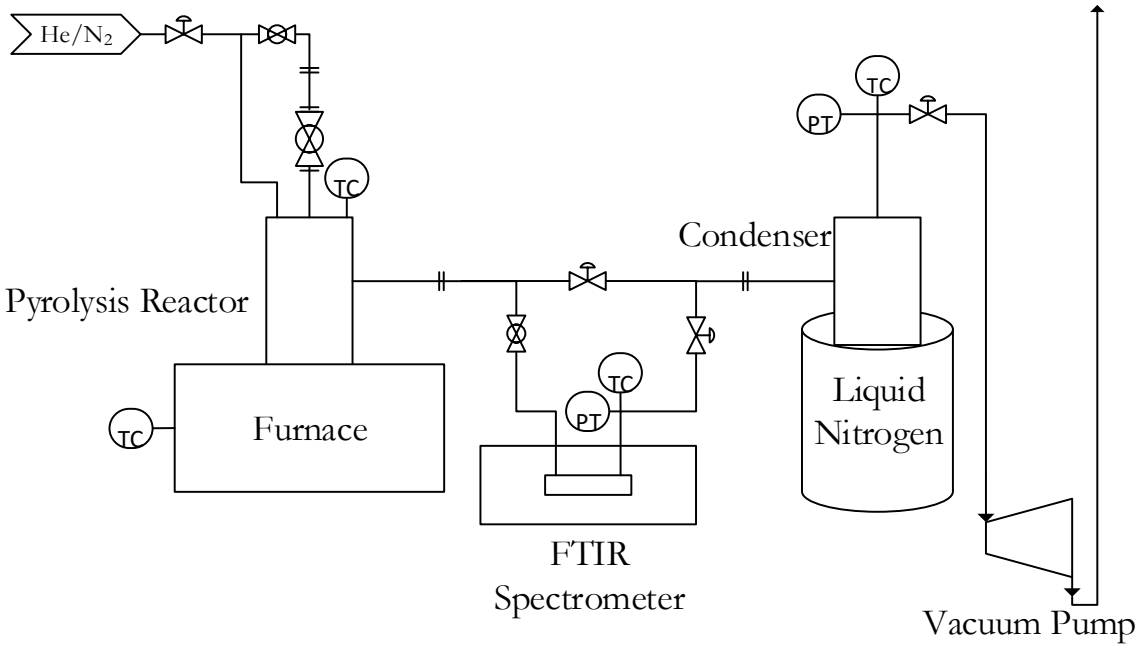

Figure 26: The pyrolysis reactor system used to pyrolyse PTFE and produce TFE, HFP and OFCB.

PTFE is loaded into a straight, one inch bore, tube above the reactor before commencing with an experiment. After initialising the experiment, the software does a series of system- flush and evacuation procedures and ultimately checks the vacuum status of the system. Once the software has established that the system is leak tight, the reactor is heated to the specified reaction temperature. A full bore, 1-inch ball valve isolates the PTFE from the reactor. This valve is opened once the reactor is at temperature and initiates the reaction sequence, which include the following:

1. Reaction time count down.
2. Temperature and pressure data acquisitioning.
3. Triggers the start of the time-resolved infrared spectra capture.

This sequence is initiated by a small switch in the lever of the ball valve and allows for accurate and immediate data capture.

Operating conditions can be varied between 550 °C and 850 °C within a pressure range of 0 kPa (abs.) up to atmospheric pressure (~86 kPa (abs.)).

3.2.1.2 Sub-Zero Semi-Batch Packed Separation Column

A packed column was available for the batch separation of TFE from the other, less volatile, products such as HFP and OFCB. The column is capable of producing TFE with a purity better than 99 %.

The column was used to separate pyrolysis products of experiments aimed at a high yield of TFE. These experiments were specifically performed to enable a good separation and produce high purity TFE for FTIR calibration purposes.

Two Julabo refrigerated circulators were used to cool the column, condenser and reboiler to the desired operating temperature. The operating conditions proposed was at a total pressure of 140 kPa (abs.) a condenser temperature of – 80 °C and a reboiler temperature of – 10 °C.

3.2.1.3 PerkinElmer Spectrum Two IR Spectrometer

A PerkinElmer Spectrum Two™ IR Spectrometer was used to obtain all experimental infrared spectra. This instrument is not state-of-the-art with respect to other FTIR spectrometers on the market. However, the size and capabilities of the instrument gave it preference over other, more sophisticated spectrometers. The unit had to be small to fit in the available space of the experimental setup to ensure that tubing lengths were kept to a minimum.

The Spectrum Two™ spectrometer was set up for sample scans as indicated in Table 4, also mentioned are the internal specifications of the instrument.

A custom built gas cell was used for all spectral measurements. The cell was manufactured from aluminium and has an optical path of 90 mm and internal diameter of 30 mm. The ends of the cell were sealed with KBr discs (38 mm ID x 6 mm) which do not interfere with the optimum range of the instrument.

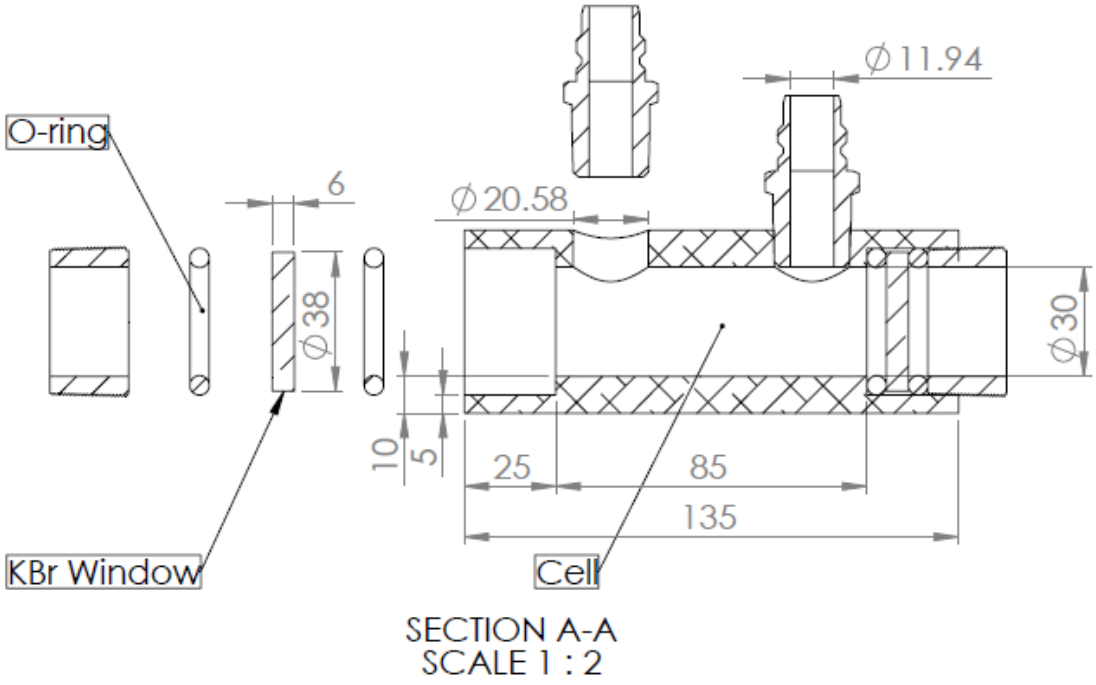

Figure 27: Design and dimensions of the gas cell used for the gas phase FTIR analyses.

Table 4: Spectrum Two instrument setup and internal configuration.

Scan range	$3000 - 500\ \text{cm}^{-1}$
Resolution	$4\ \text{cm}^{-1}$
Data interval	$1\ \text{cm}^{-1}$
Accumulations	1
Scan speed	$0.20\ \text{cm/s}$
Source	MIR
Beamsplitter	Optical KBr
Detector	$LiTaO_3$
Windows	KBr
Optimum range	$7800 - 450\ \text{cm}^{-1}$

The Spectrum Two™ is fitted with an external trigger for automated initiation of the time resolved spectra acquisitioning. The external trigger was activated by the real-time controller once the operator opened the valve to introduce PTFE to the

reactor. This ensured that the spectral data align with the reaction time and can therefore be used for kinetic studies.

3.2.1.4 PerkinElmer Clarus SQ8 GC-MS

Qualitative analysis of all pyrolysis products were performed by means of a PerkinElmer Clarus 680 gas chromatograph (GC), coupled to a PerkinElmer Clarus SQ8 C mass spectrometer (MS).

The GC was fitted with an 1 m x 1.00 mm ID Restek® Hayesep Q™ polymer packed column with a 100 / 120 mesh size.

An electron ionization source (PerkinElmer Marathon Filament, N6470012D) was used for sample ionization and both source and injection line was maintained at 120 °C for all analyses. The instrument maintained a system pressure of below 1.5×10^{-5} Torr for all analyses.

3.2.2 Experimental Design

3.2.2.1 PTFE Pyrolysis to Obtain Spectra of Pyrolysis Products

The findings of Bhadury *et al.* (2007), Lewis & Naylor (1947) and Meissner *et al.* (2004) were analysed and used to determine the appropriate operating conditions, for pyrolysis, to obtain high yields or low fraction components. Experiments were done to increase the yield specifically of tetrafluoromethane (TFM), hexafluorethane (HFE) octafluoropropane (OFP) and the octafluorobutenes (1- and 2-OFB and PFIB). The isolation of these components is important to obtain infrared spectral data for the purpose of qualitative analysis of the pyrolysis products. Infrared spectra of the octafluorobutenes are scarce or missing in the available literature and when found, not pure enough for the purposes of this investigation.

Spectra for tetrafluoroethylene (TFE), hexafluoropropene (HFP) and octafluorocyclobutane are available in the literature. However, these components

had to be produced in significant quantities, purified and analysed to obtain a set of calibration spectra for the purpose of quantitative analyses. The operating conditions for increased production of each component are shown in Table 5. Experimental runs with the most significant presence of a component were repeated at least three times to ensure the validity of the product distribution and mass spectra which were obtained.

Table 5: Optimum operating conditions for an increased yield of each component of the pyrolysis product gas.

Component	Temperature (°C)	Pressure (kPa abs.)
TFM	850	30 – 70
HFE	850	50 – 70
TFE	600 – 700	0
OFP	850	50 – 70
HFP	750 – 800	30 – 70
OFCB	550 – 600	30 – 70
OFB	850	70
PFIB	850	30 – 70

An experimental design was based on the data indicated in Table 5 and is shown in Table 6. The experimental parameters were expanded for additional data mining and comparison to existing literature in future work. Reaction pressures other than 0 kPa (abs.) were pressurised with high purity helium.

Table 6: Expanded experimental design of PTFE pyrolysis operating conditions.

T (°C)\P (kPa abs.)	0	10	30	50	70
550		○		●	
600	●		●		●
650	●	○	○	○	○
700	●		○		○
750		○		●	
800	○		●		●
850	○	○	●	●	●

The coloured dots (●) in Table 6 represent experiments that were necessary to obtain a high yield for each pyrolysis gas component. The circles (○) represent experiments that were done for validation purposes and were not necessary for the completion of this project.

3.2.3 Methods

3.2.3.1 Separation of Low Fraction Product Species for Generating Infrared Spectra

An alternative method was developed for producing (as pure as possible) infrared spectra of the components due to the limited infrared data available in the open literature. The quickest and easiest separation method was determined to be separation by means of a packed GC column. An Alltech™ Porapak™ Q, 100/120 mesh size, 5 m × 3.175 mm OD, with 2 mm ID, column was used to obtain acceptable separation of the components.

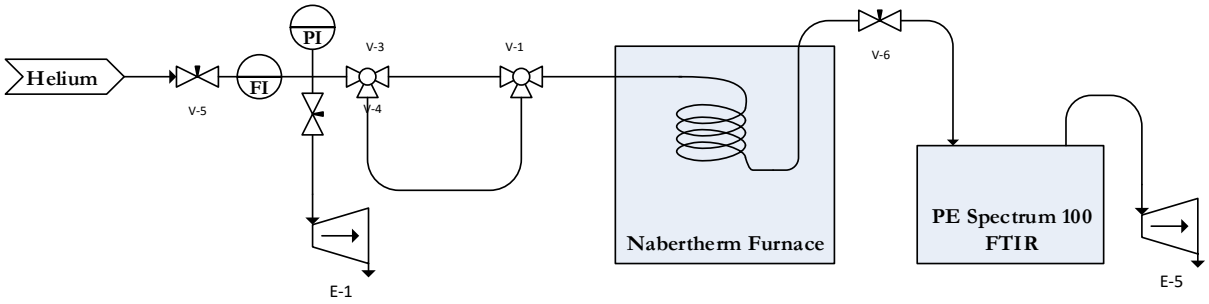

Figure 28: Process flow diagram of pyrolysis product stream separation.

Figure 28 shows the process layout and instruments used to separate the pyrolysis product stream into the individual components. Separation was done at different column temperatures to achieve the best possible degree of separation for each component.

The product gas of several experimental runs at different operating conditions were separated by means of the above mentioned method. This allowed the possibility of cross-referencing of the components based on qualitative results from mass spectroscopy.

3.2.3.2 Time-resolved Experimental Infrared Spectra

Time-resolved experimental data were obtained from the in-house developed fast pyrolysis reactor system. Pyrolysis product gas was transported from the reactor system, through a custom built gas cell and either collected in the condensed phase or vented by means of a vacuum pump.

Infrared spectra were captured at 5.4 second intervals. The rate of measurements is governed by the instrument setup. Spectra can be captured at shorter intervals but with loss of resolution. A resolution of 4 cm^{-1} yields good quality spectra, at intervals of 1 cm^{-1} and does not affect the analysis of kinetic data severely. Figure 29 represents a typical time-resolved FTIR analysis. In this case, it was captured for a GC-FTIR analysis of a PTFE pyrolysis product sample.

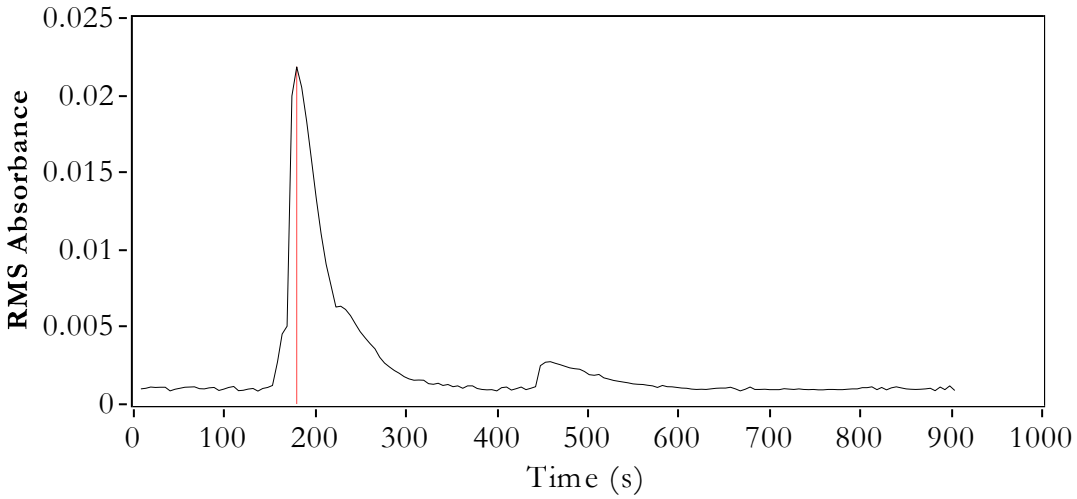

Figure 29: Total RMS absorbance profile of a GC-FTIR time-resolved analysis.

The spectrum at t = 179.4 s is shown in Figure 30. This spectrum is represented by the vertical red cursor in Figure 29.

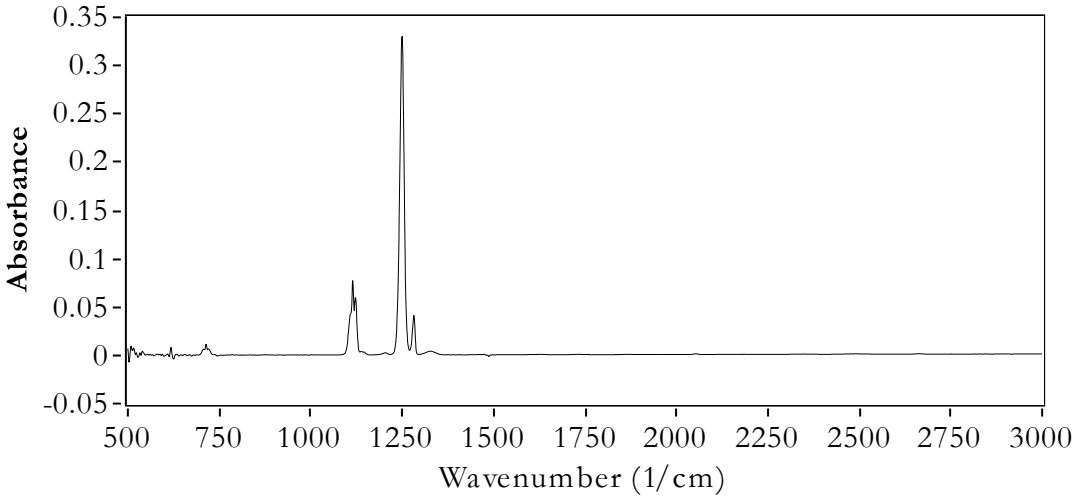

Figure 30: A slice at t = 179.4 s of a typical time-resolved GC-FTIR analysis.

3.2.3.3 GC-MS Method

The GC method used for producing well resolved peaks is as follows:

1. Hold at starting temperature of 50 °C for 1 minute.
2. Ramp temperature at a rate of 100 °C/min for 1 minute.
3. Hold at temperature of 150 °C for 8 minutes.

Helium flow was maintained at 20 ml/min and the injector was maintained at 150 °C. The MS transfer line and source were maintained at 120 °C and the MS was maintained at or below a maximum pressure of 1.5×10^{-5} Torr.

Component identification was by means of the NIST Mass Spectral Program for NIST/EPA/NIH Mass Spectral Library, version 2.0g, built May 19, 2011.

3.2.3.4 Collecting Calibration Data for the Purpose of Quantifying PTFE Pyrolysis Products

A representative data set for each possible component in the mixture to be analysed is needed to accurately predict the concentration of the component by means of infrared spectroscopy. This data set is obtained from collecting numerous spectra of pure components at a known temperature and pressure. The correlation between the absorbance at a specific wavenumber and the pressure of the absorbing specie is linear according to Beer's law. The relationship between pressure and concentration was assumed to be ideal.

Calibration data was collected for each component that could be isolated in sufficient quantities for this purpose. Varying amounts of these components were introduced into the evacuated gas cell and an infrared spectrum was collected from a sample. For components that could not be successfully isolated, a known mixture of these (produced by the pyrolysis of PTFE) components were analysed following the previously mentioned method. Molar attenuation coefficients were obtained by deconvoluting the obtained spectra and the partial pressure of each component.

To validate the calibration data, spectra for several mixtures of the pure components should be collected at known temperature and pressure and quantified by means of the calculated molar attenuation coefficients.

3.3 Results and Discussion

3.3.1 Pyrolysis of PTFE

The selectivity for specific compounds and rate of PTFE decomposition was studied to determine whether the proposed method would be viable. Experiments were performed over a range of temperatures and pressures to verify that the operation of the reactor is comparable to those reported in the literature. Samples of the pyrolysis products were taken for the purpose of purification by the methods previously discussed.

As confirmed in numerous research studies, TFE production is favoured at low pressure and moderate temperatures. The mole fraction of TFE produced is shown in Figure 31 and compares closely with the findings of other researchers. It is suggested that the best operating conditions for obtaining the highest yield of TFE is at 700 °C and 0 kPa (abs.).

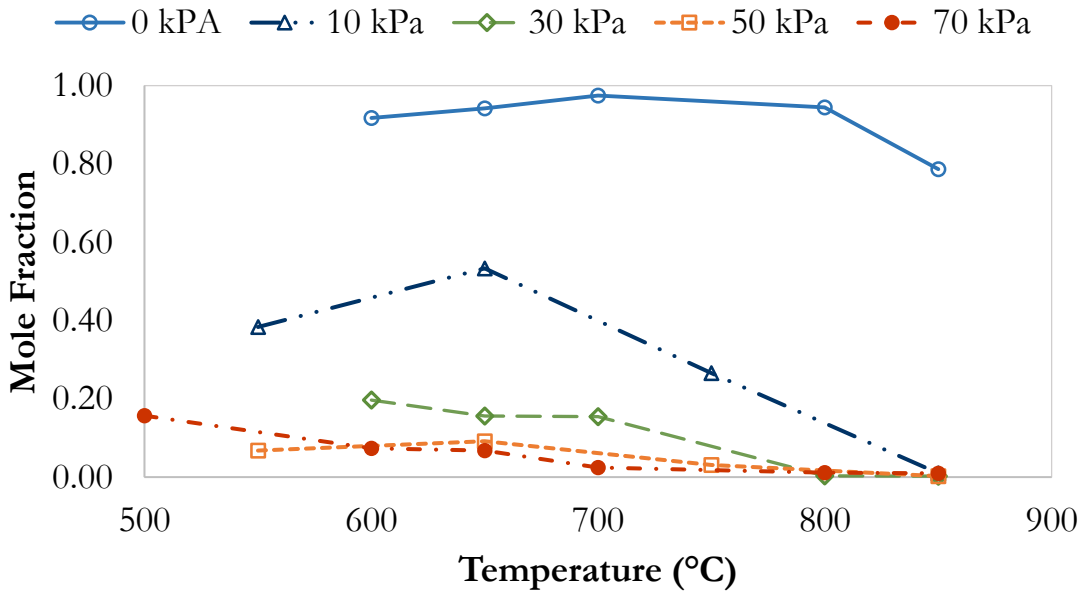

Figure 31: Fraction of TFE produced over the temperature and pressure range explored.

Figure 32 indicates the mole fraction of HFP produced at the operating conditions investigated. Substantial quantities of HFP can be obtained at high temperatures, 700 °C – 800 °C, and moderately high pressures, > 30 kPa (abs.). Selectivity toward HFP was reduced at a temperature of 850 °C where the pyrolysis product stream comprise mainly of the undesired components.

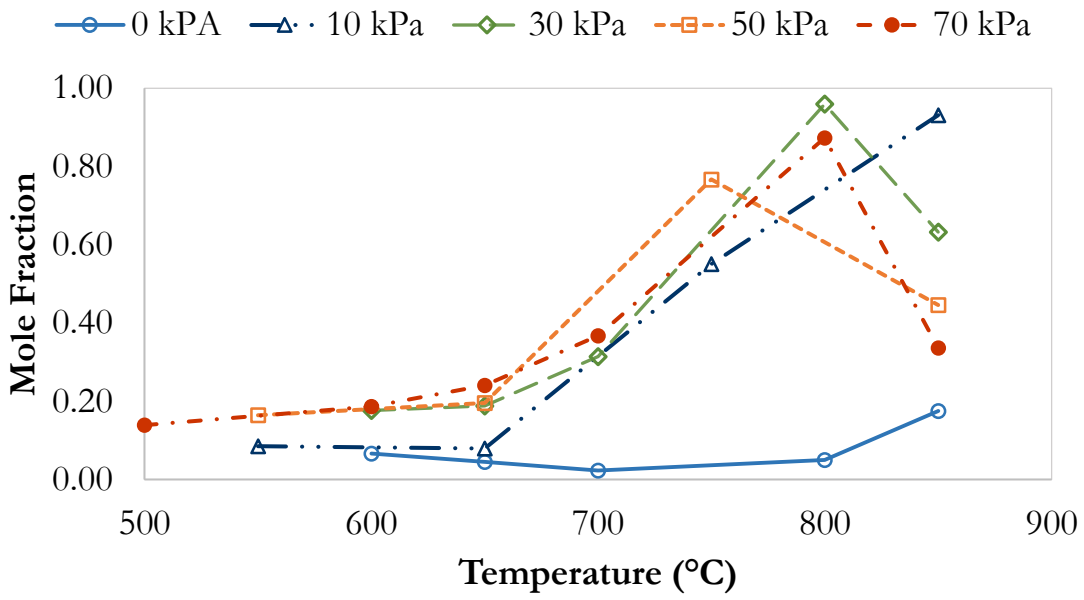

Figure 32: Fraction of HFP produced over the temperature and pressure range explored.

The pyrolysis reaction favours octafluorocyclobutane toward the lower temperatures investigated, 500 °C – 700 °C, and at pressures above 0 kPa (abs.), as seen in Figure 33. The production of OFCB is almost zero at 0 kPa (abs.).

The results of the pyrolysis experiments show that the selectivity toward the favoured products can be controlled by means of temperature and pressure. These findings correlate well with the findings of historic and recent literature. Although undesired products were obtained at the high end of the temperature (> 800 °C) and pressure range (50 – 70 kPa (abs.))(Figure 34), these products can be limited, or even eliminated, by the proper control of the reactor system.

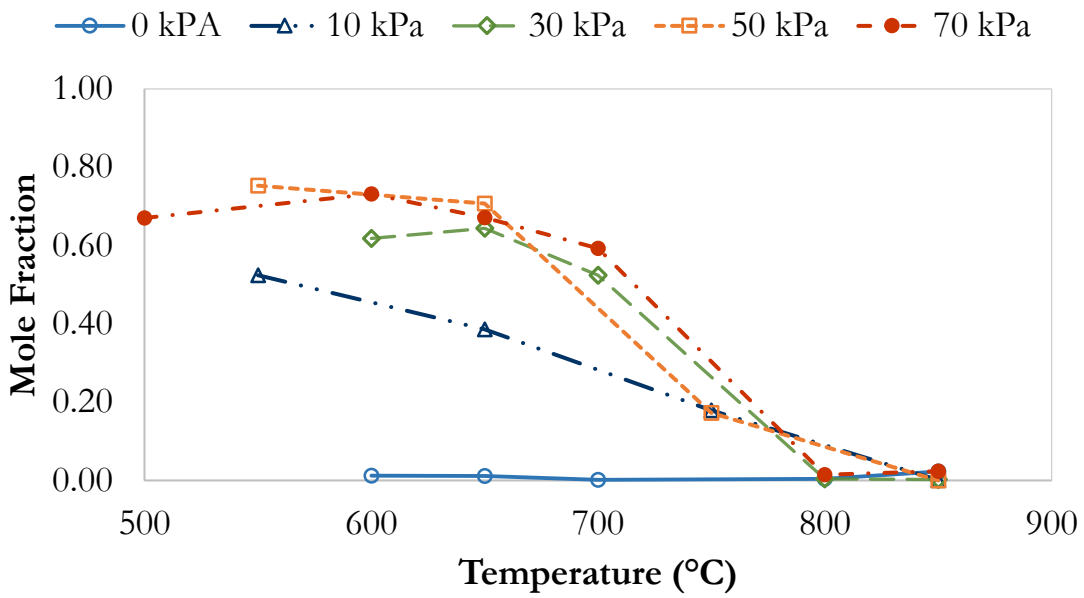

Figure 33: Fraction of OFCB produced over the temperature and pressure range explored.

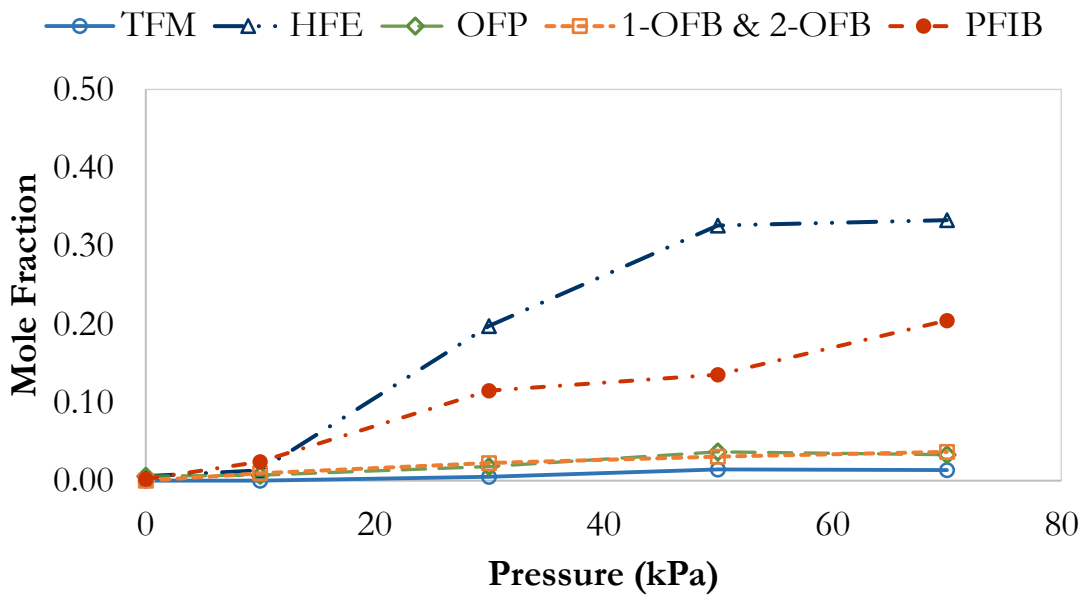

Figure 34: Fraction of pyrolysis products from undesired side reactions at 850 °C.

3.3.2 Isolation and Experimentally Obtained Spectra

Several methods were explored to obtain infrared spectra of the pure components, which can be expected in the product stream of a PTFE decomposition reaction. The main focus of this investigation is with respect to TFE, HFP and OFCB. A

qualitative indication of the presence of highly toxic components, 1- and 2-OFB and PFIB, was achieved.

3.3.2.1 Tetrafluoroethylene

Several experiments were conducted, in quick succession, to produce a large enough quantity of pyrolysis product gas. The captured pyrolysis products were then distilled in a packed bed separation column. The intent was to obtain a high purity distillate product, TFE, in sufficient quantities for further analysis. The "pure" TFE was validated by means of GC-MS. Pyrolysis reactions were performed at 650 °C and 0 kPa abs. for a high yield in TFE. The composition of these experiments are shown in Table 7. The compositions were determined from the integrated peak areas of the chromatograms observed in Figure 35. The peak at 1.47 min corresponds to TFE, 2.20 min to HFP and 2.46 min to OFCB.

Table 7: Pyrolysis product composition for experiments designed to produce a high yield of TFE.

Run	TFE	HFP	OFCB	Other
1	0.9395	0.0556	0.0041	0.0008
2	0.9382	0.0398	0.0210	0.0010
3	0.9483	0.0414	0.0095	0.0008

The data indicated in Table 7 corresponds well with the literature (Lewis & Naylor, 1947, Meissner *et al.*, 2004 and Bhadury *et al.*, 2007). Further exploration of process conditions were not considered due to the high purity achieved in these experiments.

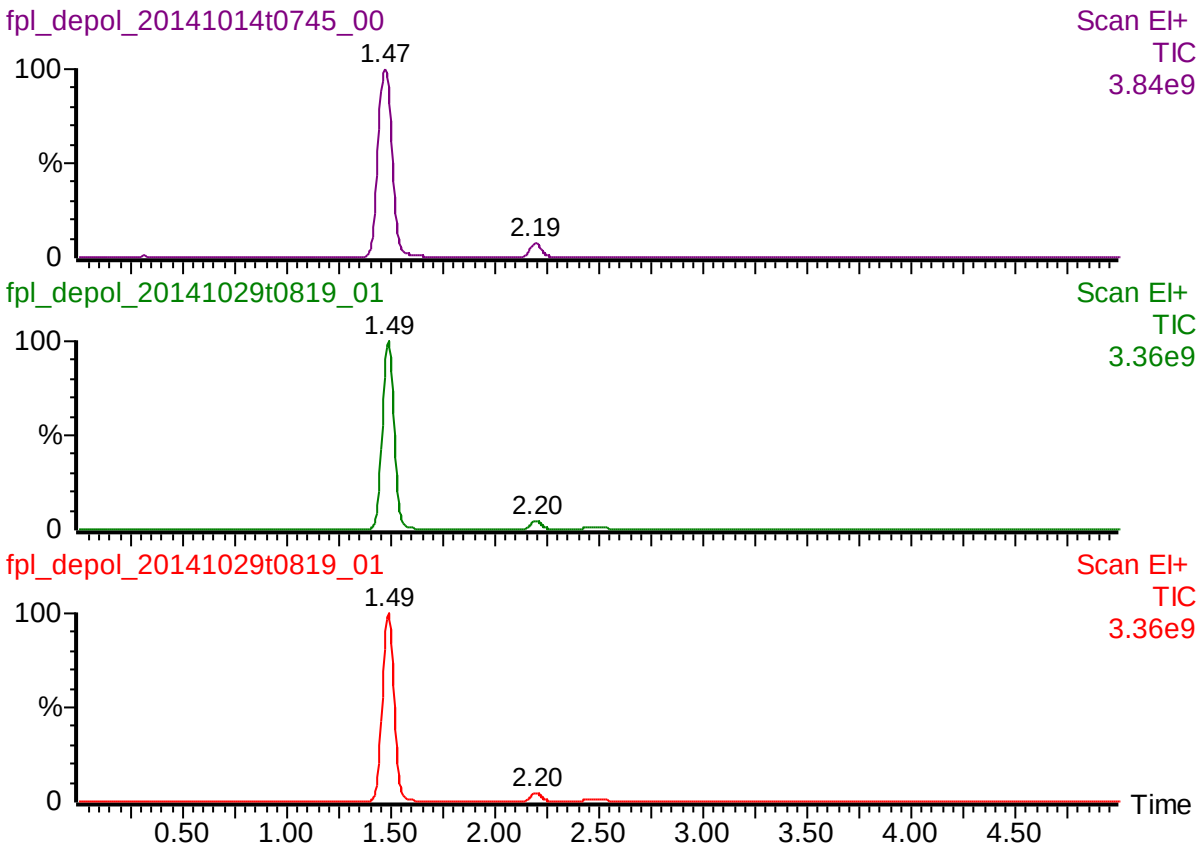

Figure 35: Chromatograms of the three experiments performed to obtain a high yield of TFE for purification purposes. These experiments were repeated at a later stage to produce sufficient quantities of product for the purpose of separation.

The more volatile TFE were separated from the higher boiling point components, (HFP and OFCB) by means of a packed bed separation column. After steady-state was achieved, the distillate was drawn off and analysed. Separation proved to be good and provided TFE with a purity in excess of 99.99 %. The chromatogram of the distillate product is shown in Figure 36.

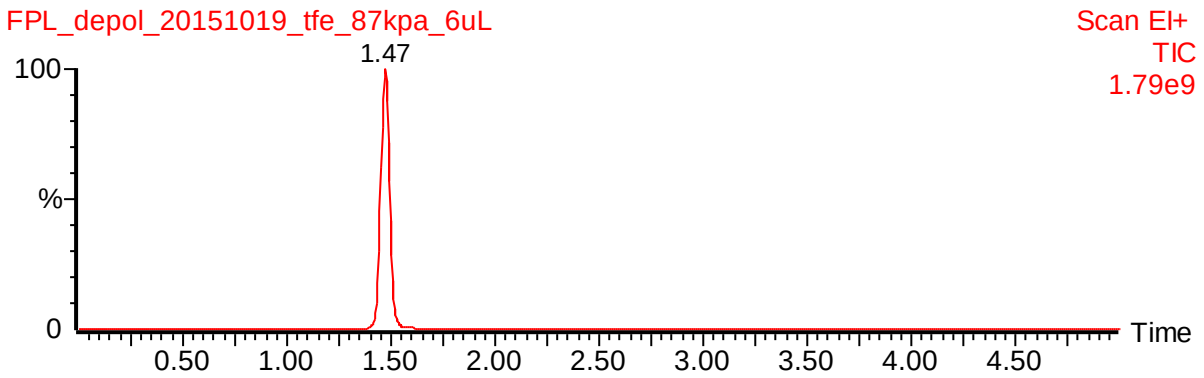

Figure 36: Chromatogram of the distillate product obtained from the pyrolysis product at 650 °C and 0 kPa (abs.).

The distillate product was analysed by means of FTIR spectroscopy and the resulting spectra were processed with the ALS algorithm. Lineshape fitting was performed on a scaled, average spectrum to determine the peak parameters for TFE.

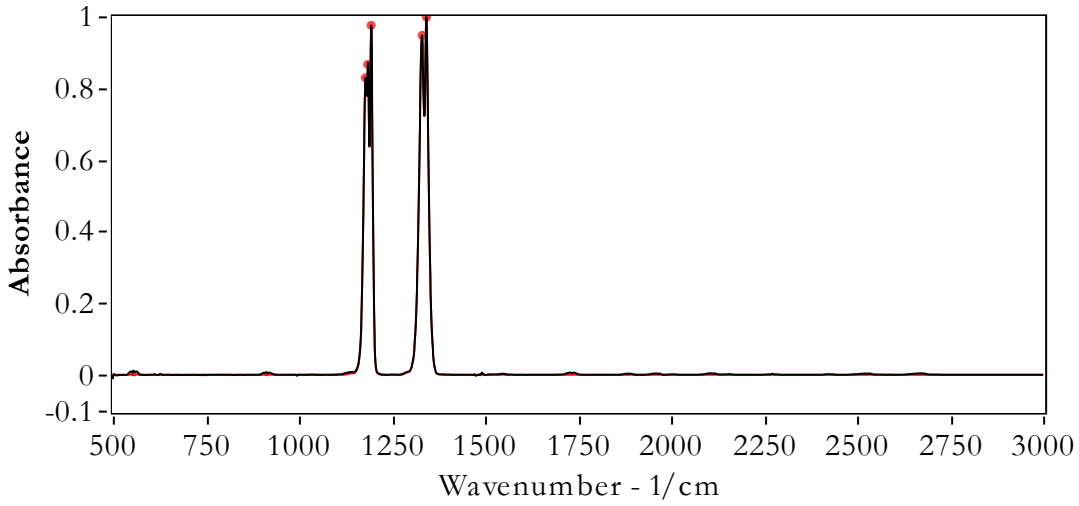

Figure 37: Experimentally obtained pure spectrum of TFE. The red dots indication peak positions. A faint red line is visible at small variations in the baseline, this is attributed to the smoothed spectrum of TFE.

Figure 37 indicates the experimentally determined spectrum of TFE. Little smoothing and baseline subtraction was required since the displayed spectrum is the average of twelve spectra captured at different pressures. The asymmetric LM method proved to yield the best solution of the lineshape parameters. The best fit parameters produce a fitted curve with an R^2 value of 0.9999 and an RMSE value of

1.405×10^{-3}. The parameters obtained for the TFE lineshape can be seen in Table 26, Appendix 5.3.1 on page 112.

3.3.2.2 Hexafluoropropylene

A cylinder of HFP, with unknown purity, was procured for the analyses with respect to pure component spectra. The purity of HFP was determined to be better than 0.9975 with unidentifiable trace components comprising the balance. The purity of the procured HFP was better than what could be achieved by means of distillation at the time. The chromatogram obtained for the HFP sample can be seen in Figure 38.

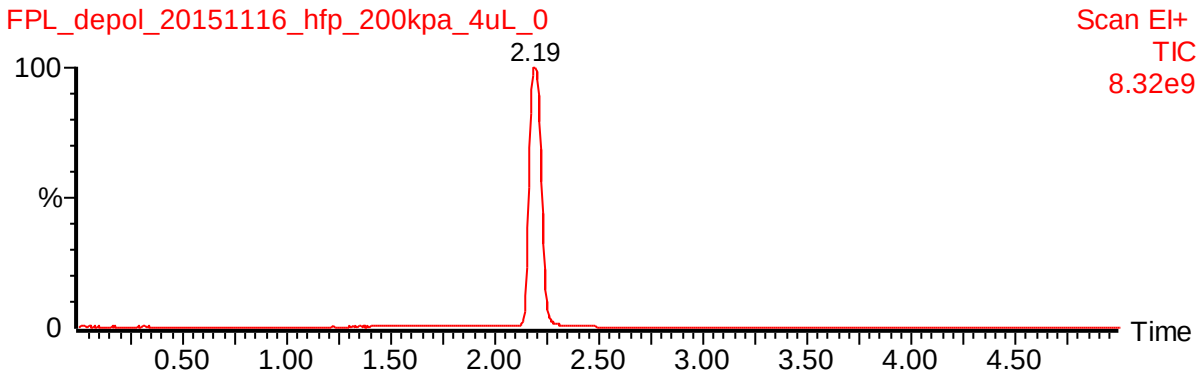

Figure 38: Chromatogram of HFP confirming a sufficiently pure sample for the purpose of this investigation.

Eleven spectra were captured at various pressures and subjected to processing with the ALS method. The resulting average spectrum of the captured spectra can be seen in Figure 39.

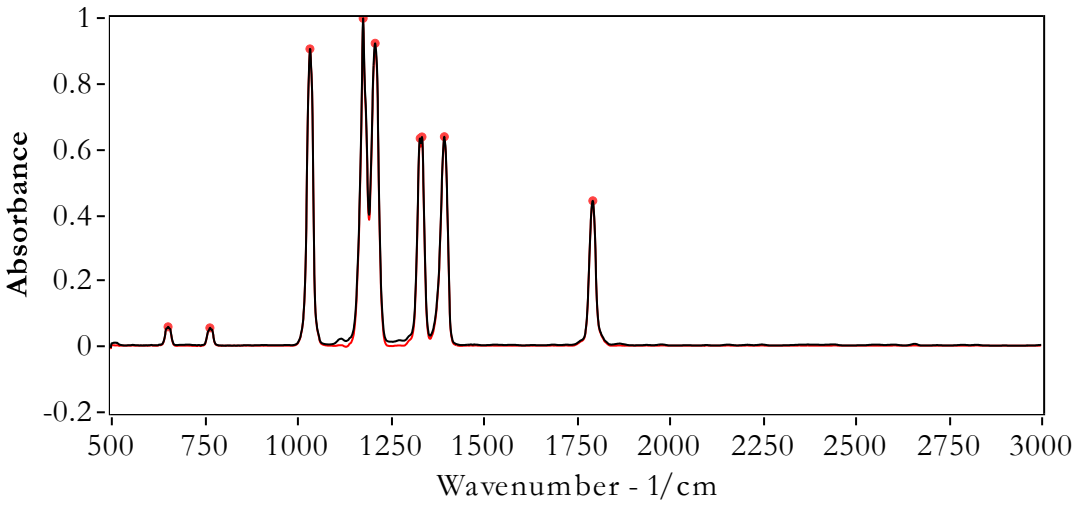

Figure 39: Average spectrum of eleven spectra of the procured HFP sample. The black line represents the average spectrum, the red line indicates the smoothed spectrum and the red dots indicate peak positions.

The smoothed, average spectrum obtained was processed for the purpose of lineshape fitting for HFP. The best fit obtained was for the asymmetric LM algorithm with goodness-of-fit indicators, R^2 of 0.9981 and RMSE of 6.344×10^{-3}. The best fit parameters for the symmetric and asymmetric LM solutions can be seen in Table 27, Appendix 5.3.2 on page 113.

3.3.2.3 Octafluorocyclobutane

The separation column used for separating TFE was unable to separate OFCB from HFP in order to yield a pure sample of OFCB. A pure spectrum of OFCB was therefore obtained by means of the method discussed in Section 3.2.3.1on page 61. The averaged spectrum was determined from two different GC-FTIR analyses, using three and six consecutive spectra, respectively. The average spectrum, and processed version thereof, can be seen in Figure 40. The spectrum is representative of OFCB. However, it is of low quality and has a low signal-to-noise ratio. Spectra obtained from a pure sample, by means of distillation, is needed to improve the quality of the subsequent best fit parameters.

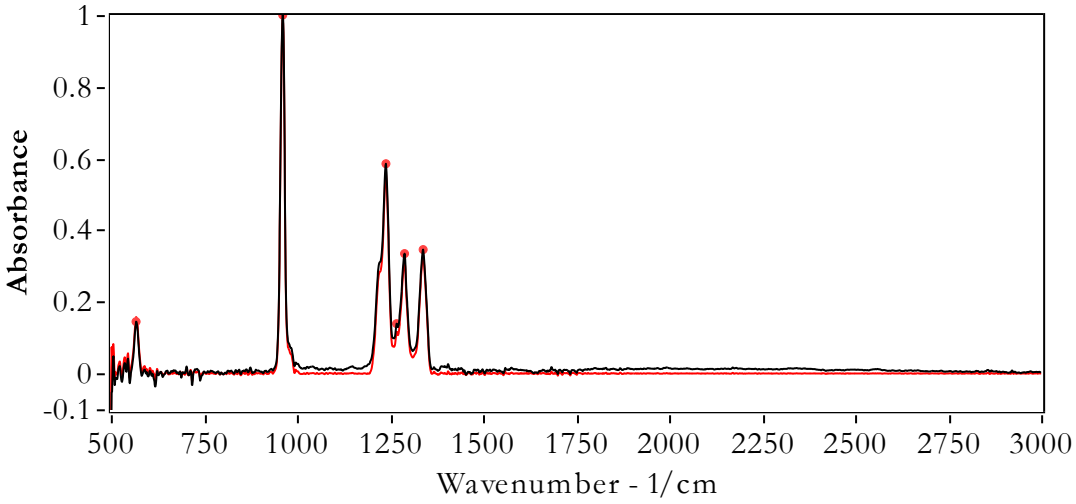

Figure 40: Experimentally generated FTIR spectrum of OFCB. The original spectra was obtained by means of GC-FTIR.

The asymmetric LM algorithm provides the best fit yet again. The best fit provided a reasonable R^2 value of 0.9625 with a corresponding RMSE value of 0.01707. Figure 41 and Figure 42 provide some insight into the relatively poor (in comparison the TFE and HFP) goodness-of- indicators.

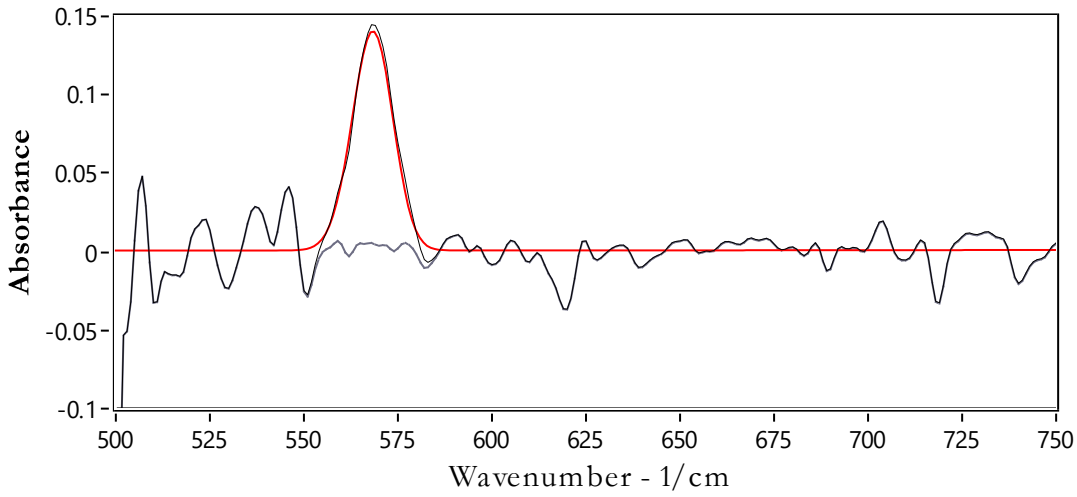

Figure 41: High frequency noise, due to low quality experimental spectra used, is partially responsible for the poor goodness-of-fit indicators.

High-frequency noise (Figure 41) is inevitable toward the low wavenumber range. This is due to the limitation of operating range of the optical KBr windows used in the gas cell. KBr windows have a longest wavelength (LWL) of transmission value of 345 cm^{-1} (Pike Technologies, 2015). The LWL limit is defined for a 1 mm thick

window and at 50 % transmission. The operating range is within the specified limits. However, the increase in noise at low wavenumbers was noticed after prolonged use of these windows.

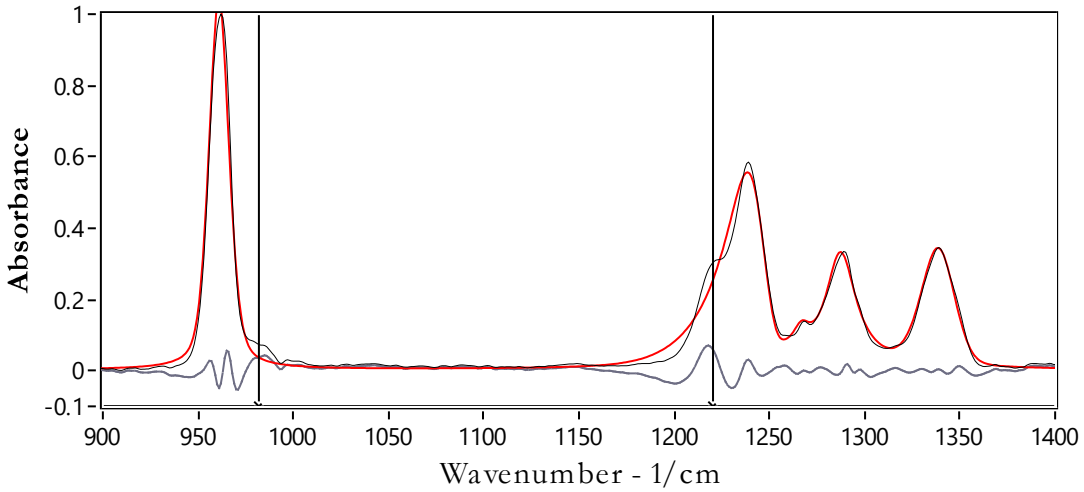

Figure 42: Two shoulder peaks were not detected and consequently not solved for by the parameter fitting function.

Figure 42 indicates the position of two shoulder peaks (refer to the positions of the two vertical lines in the figure) that were not detected and consequently solved for. The function responsible for detecting shoulder peaks and solving additional parameters was prone to fail during execution, due to an ill-behaved Hessian matrix. The function was excluded from the software package since good results were obtained without it and because of the above mentioned non-linear solving function limitations.

The best fit parameters can be seen in Table 28, Appendix 5.3.3 on page 115.

3.3.2.4 Low Fraction Components

Low fraction components include TFM, HFE, OFP, 1- and 2-OFB and PFIB. These components are of little interest with respect to quantification since they are undesired by-products of the pyrolysis reaction. Normal operating conditions, 600 °C to 700 °C and 0 kPa (abs.), include very little of these components. It is however necessary to establish qualitatively, if and when these components occur.

All the low fraction components were isolated by means of GC-FTIR for the purpose of capturing pure spectra and fitting lineshape parameters. The obtained data are presented in ascending order of carbon chain length.

Carbon tetrafluoride, hexafluoroethane and octafluoropropane was produced in sufficient quantities at elevated temperatures, > 800 °C and 70 kPa (abs.), for time-resolved FTIR analysis (refer to Section 3.2.3.2 on page 62 for details on the method used). Spectra that were considered pure enough for each of these components are shown in Figure 43 to Figure 45

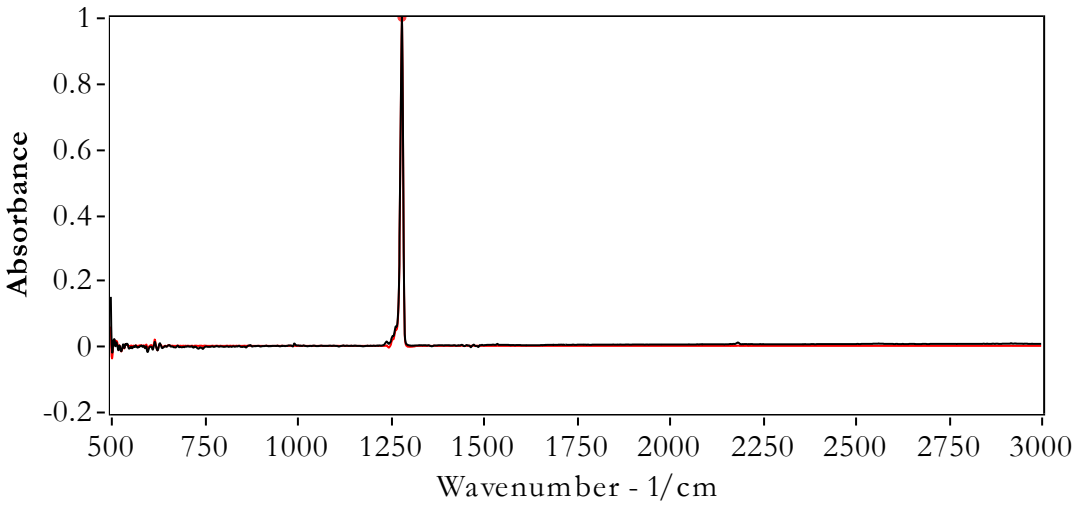

Figure 43: Carbon tetrafluoride IR absorbance spectrum obtained from GC-FTIR analysis.

Carbon tetrafluoride was represented as a single peak. However, this is most definitely not true as shown in Figure 43. A small shoulder peak exists at the base of the peak found at 1282 cm^{-1}. The asymmetric lineshape can compensate for the shoulder peak by adjusting the asymmetry of the peak. This solution is scientifically incorrect. However, the mathematical formulation of these spectra are only intended for qualitative and quantitative analyses. A good, scientifically incorrect fit would provide better results than a bad, scientifically correct fit. The asymmetric LM algorithm provided a good fit to the experimental data with an R^2 value of 0.9869 and RMSE value of 5.737×10^{-3}.

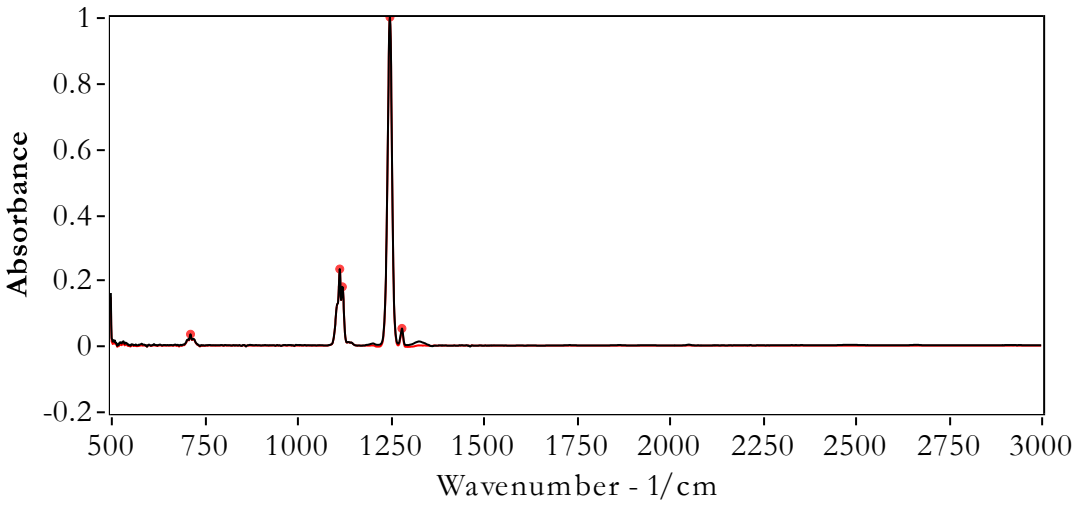

Figure 44: Hexafluoroethane IR absorbance spectrum obtained from GC-FTIR analysis.

HFE was produced in considerable quantities and good experimental spectra were obtained for this compound. Figure 44 shows the resulting spectrum, fitted with the asymmetric LM method. An R^2 value of 0.9944 and RMSE value of 4.858×10^{-3} was obtained for the fitted parameters.

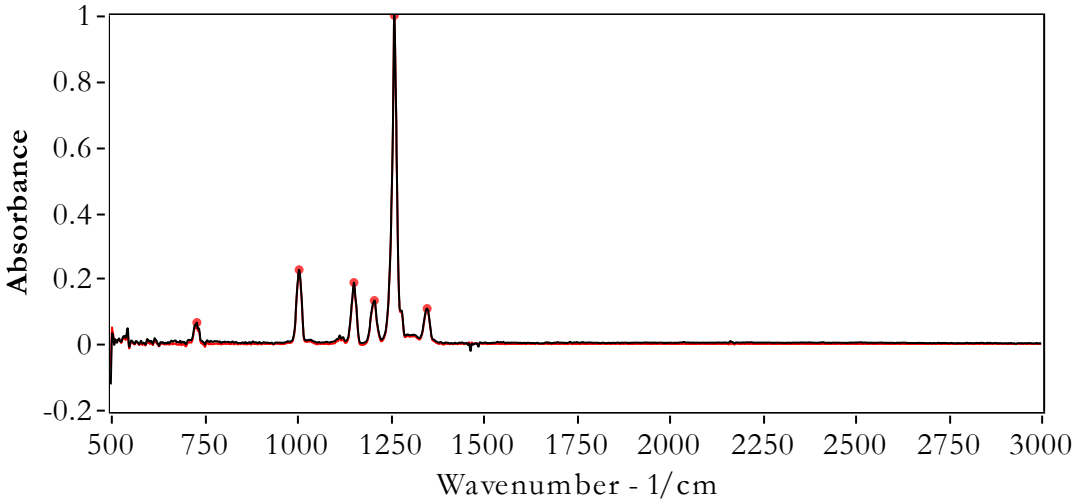

Figure 45: Octafluoropropane IR absorbance spectrum obtained from GC-FTIR analysis.

Octafluoropropane was produced in small quantities and proved to be difficult to isolate with the, crude, GC-FTIR method used. A representative spectrum was, however, obtained and is shown in Figure 45. The fitted parameters produces a good fit with R^2 of 0.9894 and RMSE of 6.809×10^{-3}.

The perfluorobutenes proved to be very difficult to isolate. Elution times through the column were the same for 1-OFB and 2-OFB. Besides the similar elution times, poorly resolved peaks were obtained and always included some tails of preceding or trailing peaks. The spectrum shown in Figure 46 is believed to be that of a combination of the two straight chain butenes. It can be said, with certainty, that other considered compounds attribute to this spectrum and that no other fluorinated carbon, not included in this study, was found upon analysis of the GC-MS data. By method of elimination, the spectrum considered in Figure 46 is therefore attributed to the two straight chain butenes. It should be noted that these components could not be successfully resolved with complex GC-MS methods either. To consider the combination of these compounds as a single entity should not compromise the resulting data since both are produced at the same operating conditions and in very small quantities.

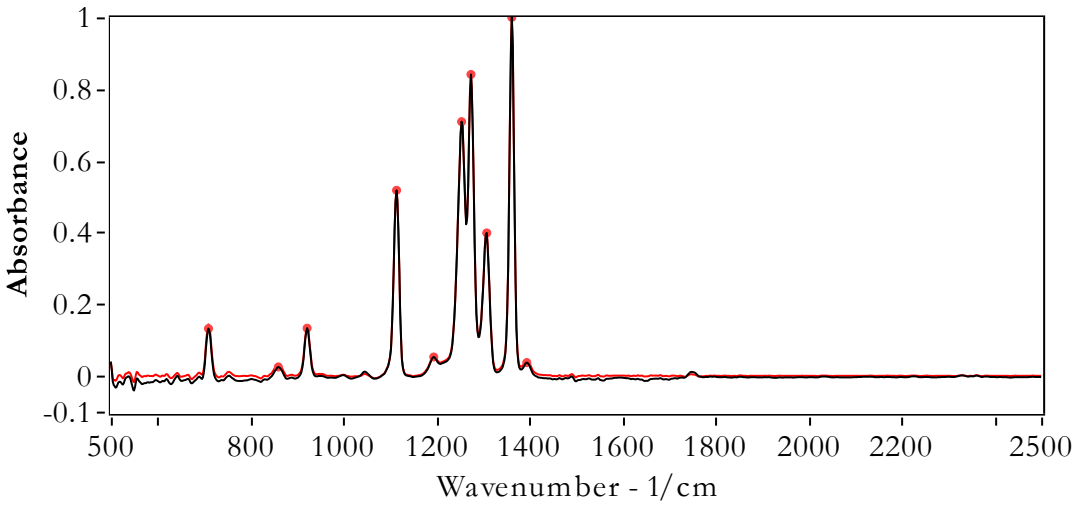

Figure 46: 1- and 2-octafluorobutene IR absorbance spectrum obtained from GC-FTIR analysis. The components are not distinguishable due to both having the same elution time.

A fitted asymmetric Voigt model resulted in an R^2 value of 0.9945 and RMSE value of 8.944×10^{-3}, for the spectrum of the OFB compounds shown in Figure 46.

Perfluoroisobutene was isolated by means of GC-FTIR. The spectrum obtained contained some artefacts from an HFP tail. The HFP artefact was subtracted, based on the intensity of the peak located at 1794 cm^{-1}. The resulting spectrum is

considered a reasonably pure spectrum of perfluoroisobutene (Figure 47). The peaks located at 1115, 1124 and 1250 cm^{-1} are considered to be from possible contaminants.

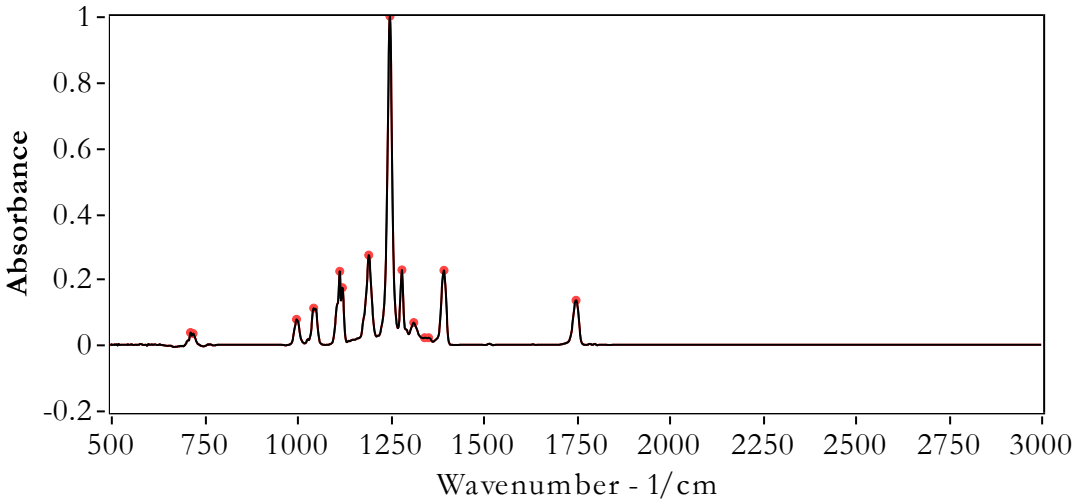

Figure 47: Perfluoroisobutene IR absorbance spectrum obtained from GC-FTIR analysis.

The asymmetric lineshape solution to the spectrum produced an R^2 value of 0.9987 and RMSE value of 2.651×10^{-3}.

The parameters solved for each component discussed are listed in Appendix 5.3 on page 112.

3.3.3 Correlation of Pyrolysis Products to Beer's Law

To enable qualitative and quantitative prediction of the pyrolysis products, one must obtain a full calibration data set for each component produced. Results obtained for all possible pyrolysis productsare presented here. Sufficient data was collected to quantify TFE, HFP and OFCB accurately. The remainder of the products were evaluated from mixtures of these products. These components are produced at temperatures in excess of 800 °C and at pressures in excess of 30 kPa (abs). To achieve elevated pressures, helium was introduced and could possibly be trapped in the condensed products. This would however be very little and should not dilute the condensed sample significantly.

3.3.3.1 Tetrafluoroethylene

A pyrolysis product mixture containing a known fraction of tetrafluoroethylene was injected into the gas cell used for time-resolved infrared analysis. The purity of TFE obtained from the run was 34.6 %, HFP accounted for 11.7 % and OFCB another 53.7 %.. The path length of the gas cell used is 85 mm. Spectra were taken at various pressures to obtain a distribution of absorbance data as a function of concentration. The collected data can be seen in Figure 48, which was collected at 1342 cm^{-1}. A straight line was fitted to the data and the best fit obtained by means of the least absolute residual method and a slope of 8465 dm^3/mol was obtained. The linear fit has an R^2 value of 0.9998 which is a good indication of the adherence to Beer's law.

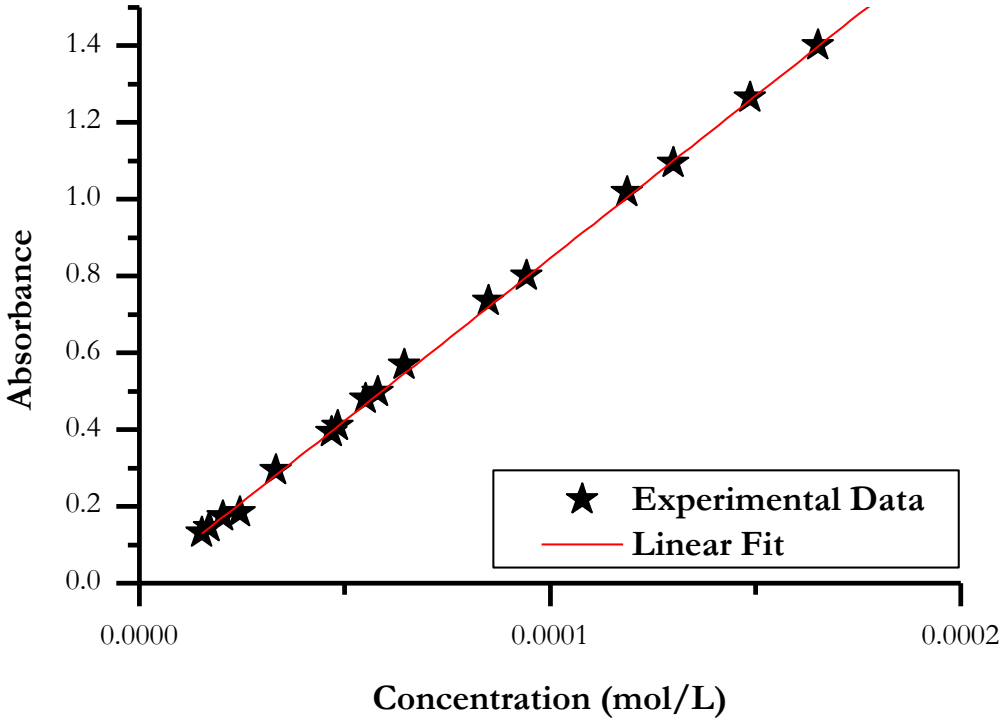

Figure 48: Correlation of the molar attenuation coefficient of TFE at x = 1342 cm^{-1}.

The molar attenuation coefficients at the peak positions of TFE can be seen in Table 8. The temperature was monitored and noted as constant at 24.8 °C ±0.6.

Table 8: Molar attenuation coefficients determined at the peak positions of TFE.

Wavenumber (cm^{-1})	ε (dm^2/mol)
1179	8419
1186	8734
1195	9665
1330	9581
1342	9959

3.3.3.2 Hexafluoropropylene

A sample of HFP was also subjected to the same procedure as for TFE. All peaks of HFP showed little deviation from linearity (Figure 49). The linear fit to the data has an R^2 value of 0.9993.

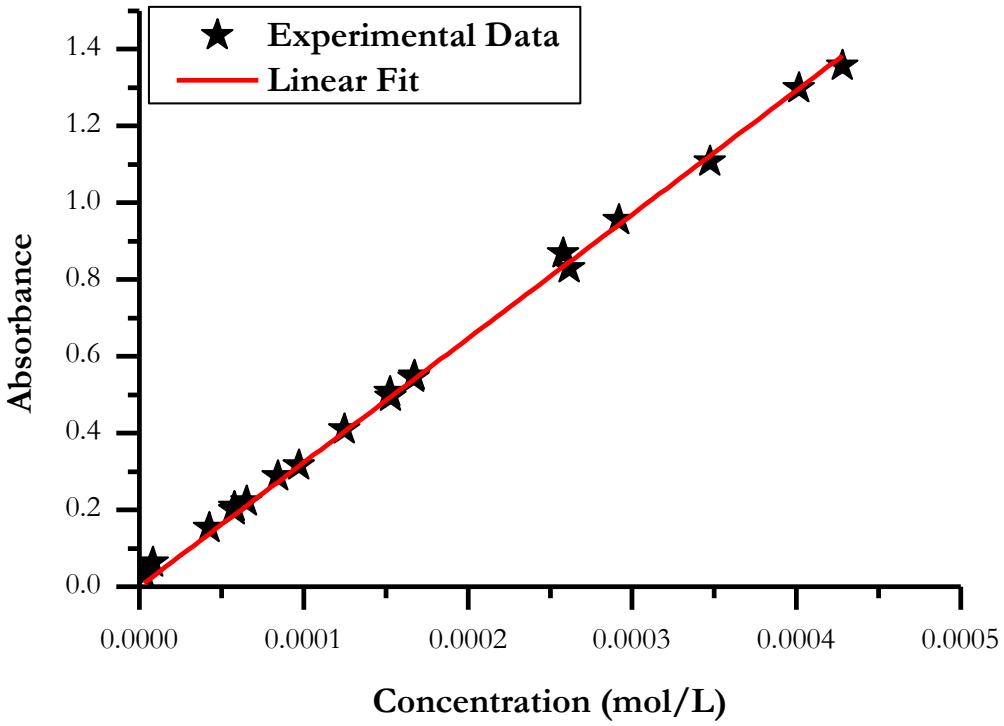

Figure 49: Correlation of the molar attenuation coefficient of HFP at x = 1329 cm^{-1}.

The molar attenuation coefficients at the peak positions of HFP can be seen in Table 9.

Table 9: Molar attenuation coefficients determined at the peak positions of HFP.

Wavenumber (cm^{-1})	ε (dm^2/mol)
1035	5732
1179	5775
1210	5818
1329	3804
1338	3689
1396	3941
1794	2805

3.3.3.3 Octafluorocyclobutane

A mixture containing 53.7 % OFCB, 34.6 % TFE and 11.7 % HFP was analysed to determine the molar attenuation coefficient for OFCB. This mixture was also used to validate the results for HFP and TFE. The result obtained for OFCB was consistent with Beer's law and is linear for all peak centres. Figure 50 indicates the close fit to linearity and is fitted with a slope of 4125 dm^3/mol and an R^2 value of 0.9999.

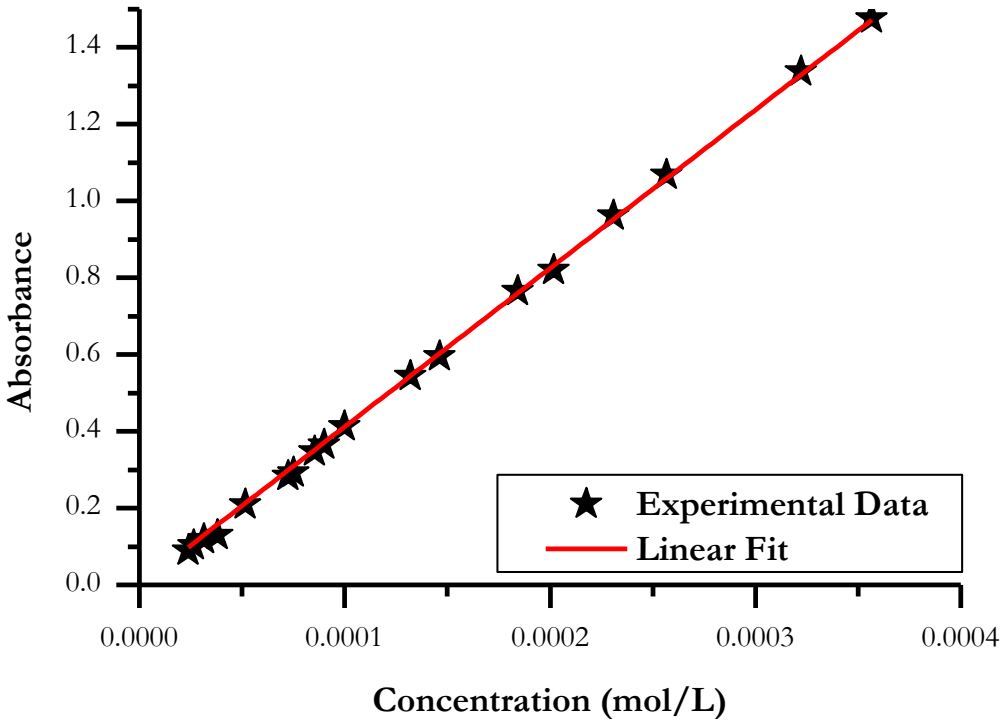

Figure 50: The linear trend obtained for the molar attenuation coefficient for OFCB at 961 cm^{-1}.

The molar attenuation coefficients for OFCB can be seen in Table 10.

Table 10: Molar attenuation coefficients of OFCB at the peak centres.

Wavenumber (cm^{-1})	ε (dm^2/mol)
569	654
962	4848
1236	2492
1267	638
1288	1547
1339	1601

3.3.3.4 Low Fraction Products

The remainder of the possible products were obtained from a high temperature and pressure run to produce these products in sufficient quantities. Molar attenuation coefficients were obtained for perfluoromethane, perfluoroethane and

perfluoroisobutene. The quantity of the octafluorobutenes and perfluoropropane was insufficient to determine molar attenuation coefficients. This is however not a major drawback since the maximum fraction that has ever been recorded in this laboratory is less than 5 % and at conditions in excess of the standard operating conditions. Table 11 indicates the molar attenuation coefficients of the low fraction components. The linear fit to the data is not as good as for TFE, HFP and OFCB, however, TFM is only ever noticed at very low fractions and since it is fitted (to the experimental spectrum) with only one peak, deviations occur regularly. The fitted lines for HFE and PFIB are much better and reliable which is especially desirable for PFIB.

Table 11: Molar attenuation coefficients of the low fraction components at the peak centre of maximum absorbance.

Component	Wavenumber (cm^{-1})	ε (dm^2/mol)	R^2
TFM	1282	80411	0.795
HFE	1250	16859	0.968
PFIB	1250	83600	0.988

3.3.4 Quantification of Batch Pyrolysis Data

The molar attenuation data for the PTFE pyrolysis products were used to quantify batch pyrolysis runs over the entire range of operating temperatures and pressures. Fifteen experiments were analysed and compared to the literature and previous work conducted in the lab. To ensure no holdup of products, the system was constantly evacuated and no composition analyses were available for comparison. However, the same experiments were conducted and collected for sampling previously (see Section 3.3.1 on page 65). However, it should be noted that the experiments that were sampled could be subjected to further reactions and could therefore predict a higher composition in products such as HFP, OFCB and PFIB than predicted for the experimental data shown here. All experimental data sets were quantified by the function described in Section2.2.4 on page 32. Although the function was not

executed during the experiment, the execution time per spectrum processed was noted to provide insight into the time dependence of the function.

3.3.4.1 T = 550 °C and P = 10 kPa (abs.)

Figure 51 shows the concentration profile determined from the time-resolved spectra of an experiment at 550 °C and 10 kPa (abs.). A total of 114 spectra were analysed (note that only every 5th data point is indicated with a symbol for clarity).

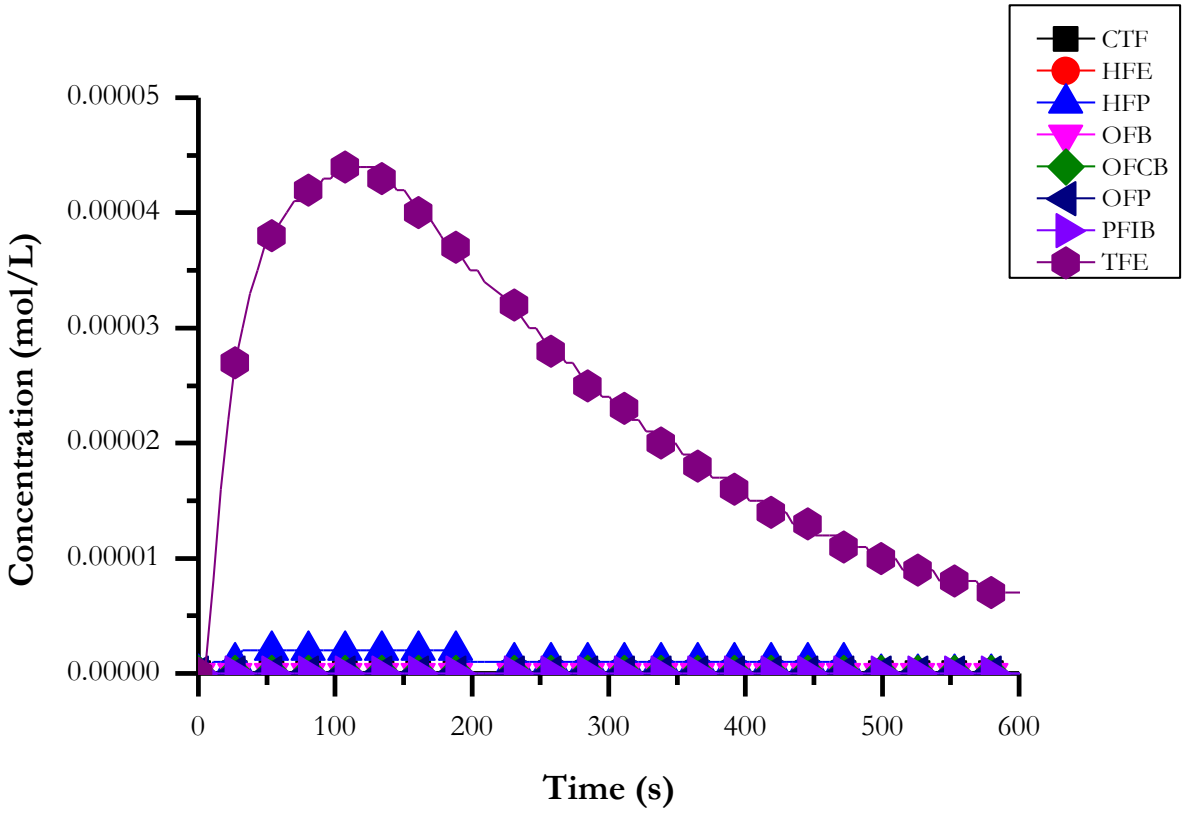

Figure 51: Concentration profile as determine with the quantification function for the pyrolysis of 0.1 g of PTFE at 550 °C and 10 kPa (abs.).

The composition of the total mixture was calculated from the concentration profile obtained and is shown in Table 12. The actual fractions determined by GC-MS on similar experiments are also indicated in the table. It should be noted that the fractions of OFB and OFP are omitted since the molar attenuation coefficient could not be calculated.

Table 12: Composition of the pyrolysis products at 550 °C and 10 kPa (abs) as determined by the quantification function and by GC-MS from historic data.

Component	Calculated	Actual
CTF	0	0
HFE	0	0
HFP	0.0285	0.020
OFCB	<0.001	0.00022
PFIB	<0.001	0
TFE	0.971	0.979

It is definite from the data in Table 12 that the calculated composition resembles that of the historic experiments at similar conditions. Comparison of the composition data to a closed system experiment (with no induced flow) is not possible since these experiments are prone to further reaction and produce significant quantities of OFCB at the operating conditions.

The average execution time for the entire batch of spectra was 1998 ms, which is well within the maximum available time of 5.4 s. The maximum execution time for a spectrum was 2578 ms and also well within the limit proposed. Analysis of the R^2 values obtained from the set of spectra indicate varying quality of fit to the data. This is due to the number of spectra that does not have any peaks (before and after the majority of the product has passed the spectrometer). Spectra with little signal show a very bad fit although this is not meaningful. Figure 52 indicated the R^2 indicator for each spectrum and also shows the lack of fit to the first two spectra. However, as discussed previously, the function fits signals to a spectrum of noise only, hence the lack of fit.

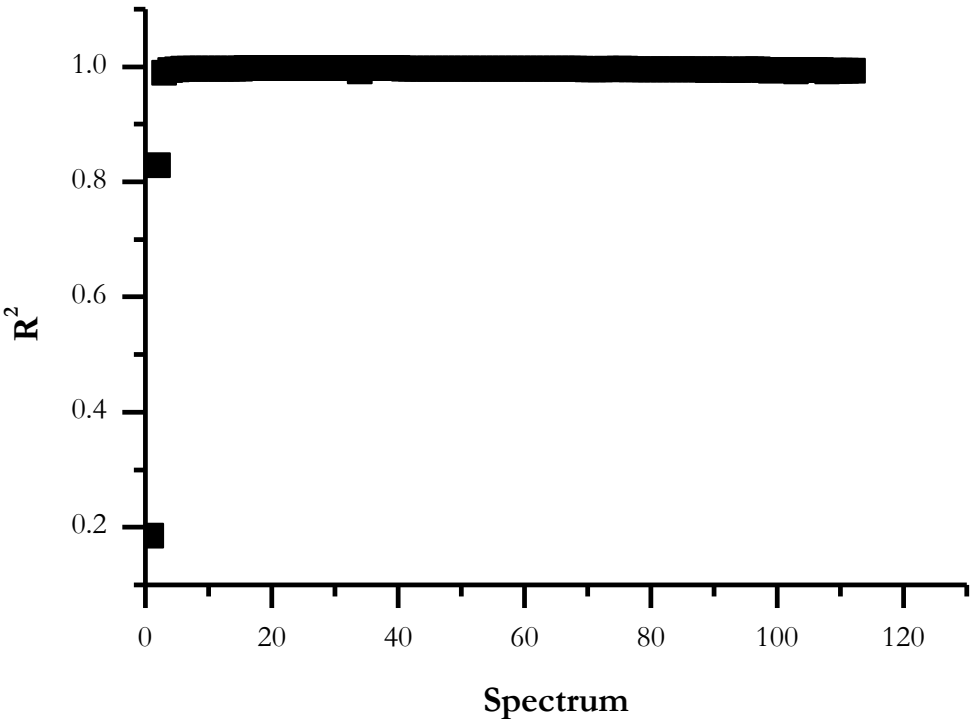

Figure 52: R^2 indicator for each spectrum analysed.

3.3.4.2 T = 550 °C and P = 70 kPa (abs.)

The concentration profile (Figure 53) at 70 kPa (abs.) indicates essentially the same profile as that at 10 kPa (abs.) with only a slight increase in OFCB and HFP during the experiment. According to literature, these products are produced from TFE and not directly from the polymer. The formation thereof is favoured by a higher localised concentration of TFE. The increased localised partial pressure is due to the decreased rate of transport away from the reactor which is in turn caused by the increased reactor pressure.

The maximum execution time for this set of spectra was 2696 ms and the average execution time was 2227 ms, also well within the proposed limit. The minimum R^2 indicator for the data set was 0.9765 which indicates a very good fit to all spectra.

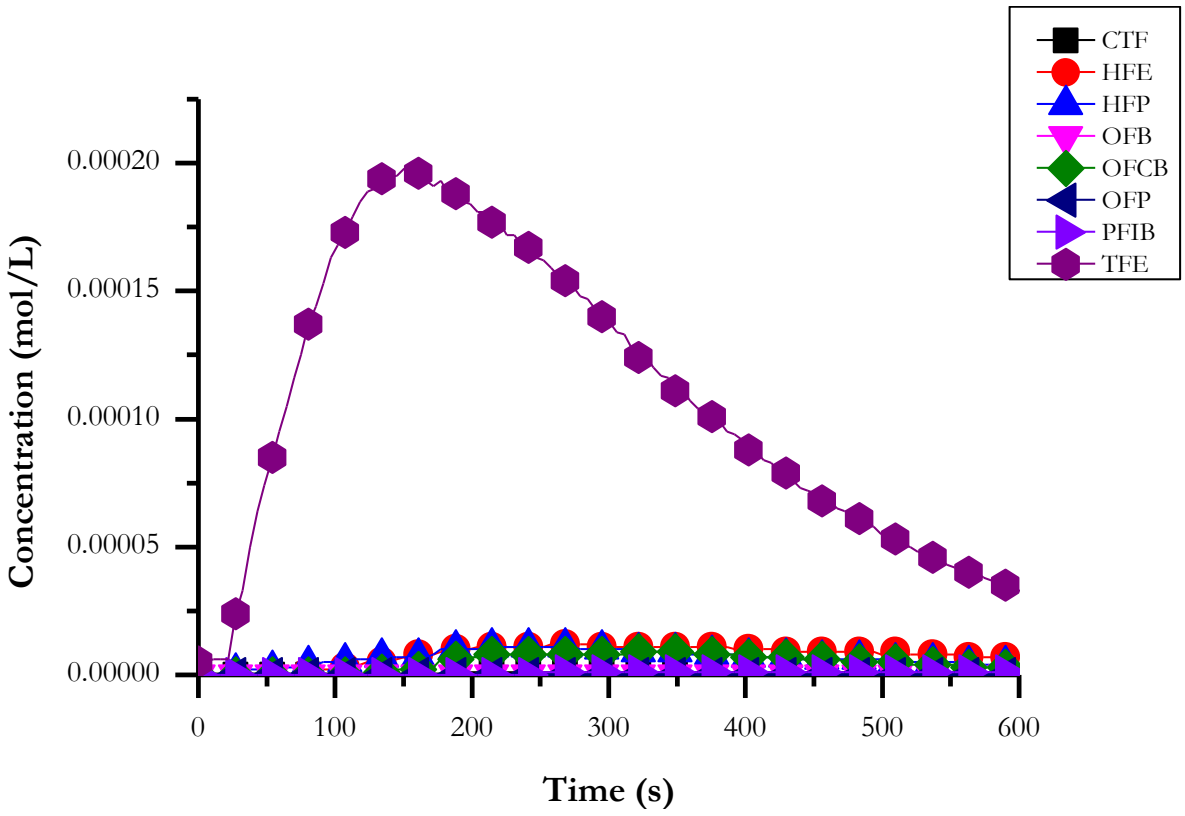

Figure 53: Concentration profile as determine with the quantification function for the pyrolysis of 0.1 g of PTFE at 550 °C and 70 kPa (abs.).

Table 13 shows the calculated composition for the experiment. No data is available for a similar experiment analysed by means of GC-MS.

Table 13: Composition of the pyrolysis products at 550 °C and 70 kPa (abs) as determined by the quantification function.

Component	Calculated
CTF	0.007
HFE	0.046
HFP	0.036
OFCB	0.019
PFIB	0.002
TFE	0.888

3.3.4.3 T = 650 °C and P = 10 kPa (abs.)

At 650 °C the concentration profile indicate an increase in yield of OFCB and HFP with respect to 550 °C. Figure 54 show a significant increase in reaction time which is consistent with historic data. The increase in OFCB and HFP is also comparable to previous results obtained in this laboratory.

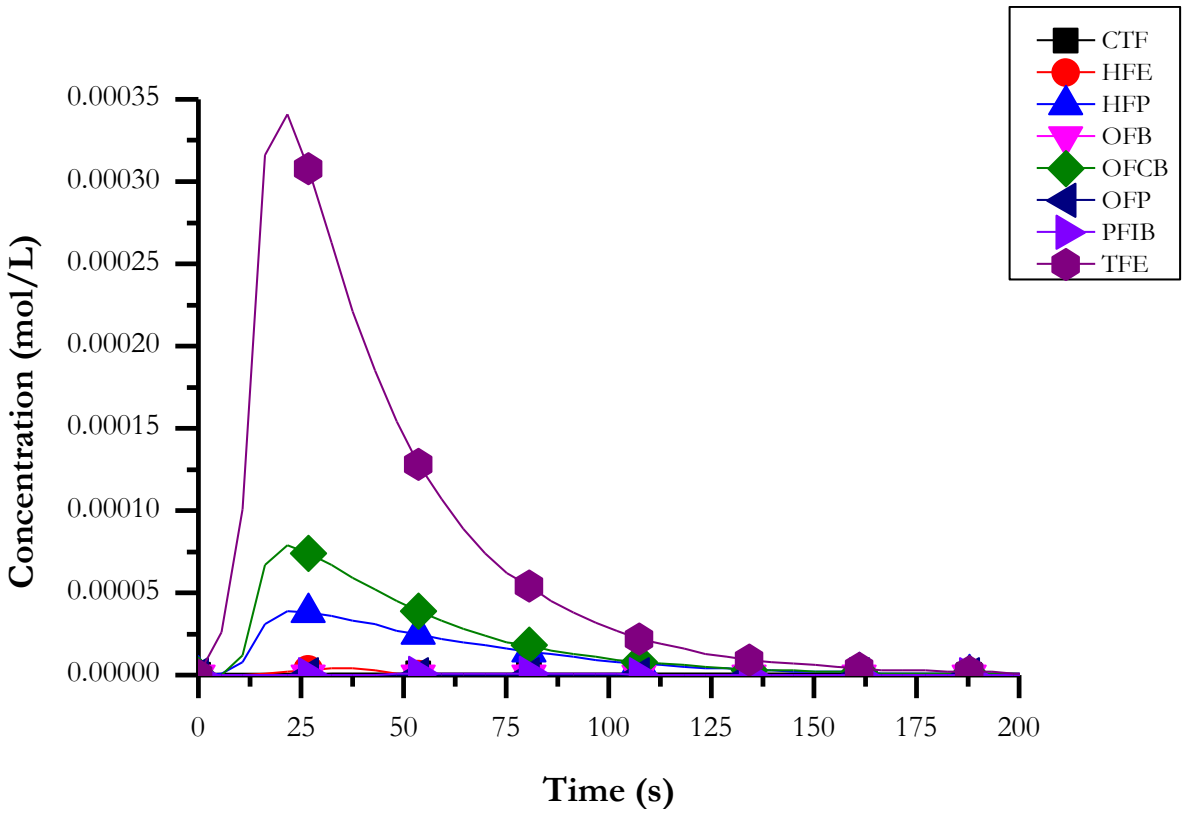

Figure 54: Concentration profile as determine with the quantification function for the pyrolysis of 0.1 g of PTFE at 650 °C and 10 kPa (abs.).

The average execution time of the data set is within the limit at 2156 ms and the maximum execution time was 2528 ms.

Table 14 shows the compositional analysis as calculated with the quantification function, no quantified mass spectrometer data was available for comparison. However, similar closed system experiments show similar trends in the composition, except for much higher preference toward HFP and OFCB.

Table 14: Composition of the pyrolysis products at 650 °C and 10 kPa (abs) as determined by the quantification function.

Component	Calculated
CTF	0.01
HFE	0.005
HFP	0.088
OFCB	0.105
PFIB	0.002
TFE	0.791

3.3.4.4 T = 650 °C and P = 70 kPa (abs.)

As suspected, the preference toward HFP and OFCB is ever increasing with an increase in pressure (Figure 55). The execution time for both average (2247 ms) and maximum (2368 ms) are within the proposed limits. The calculated composition of the total mixture can be seen in Table 15: Composition of the pyrolysis products at 650 °C and 70 kPa (abs) as determined by the quantification function.. In both composition and time-resolved concentration profile one notice a sharp increase in the production of HFP and OFCB. It should be noted that the delay in product formation at higher pressure is due to dilution of the product in the inert gas.

Table 15: Composition of the pyrolysis products at 650 °C and 70 kPa (abs) as determined by the quantification function.

Component	Calculated
CTF	0.027
HFE	0.012
HFP	0.170
OFCB	0.189
PFIB	0.006
TFE	0.596

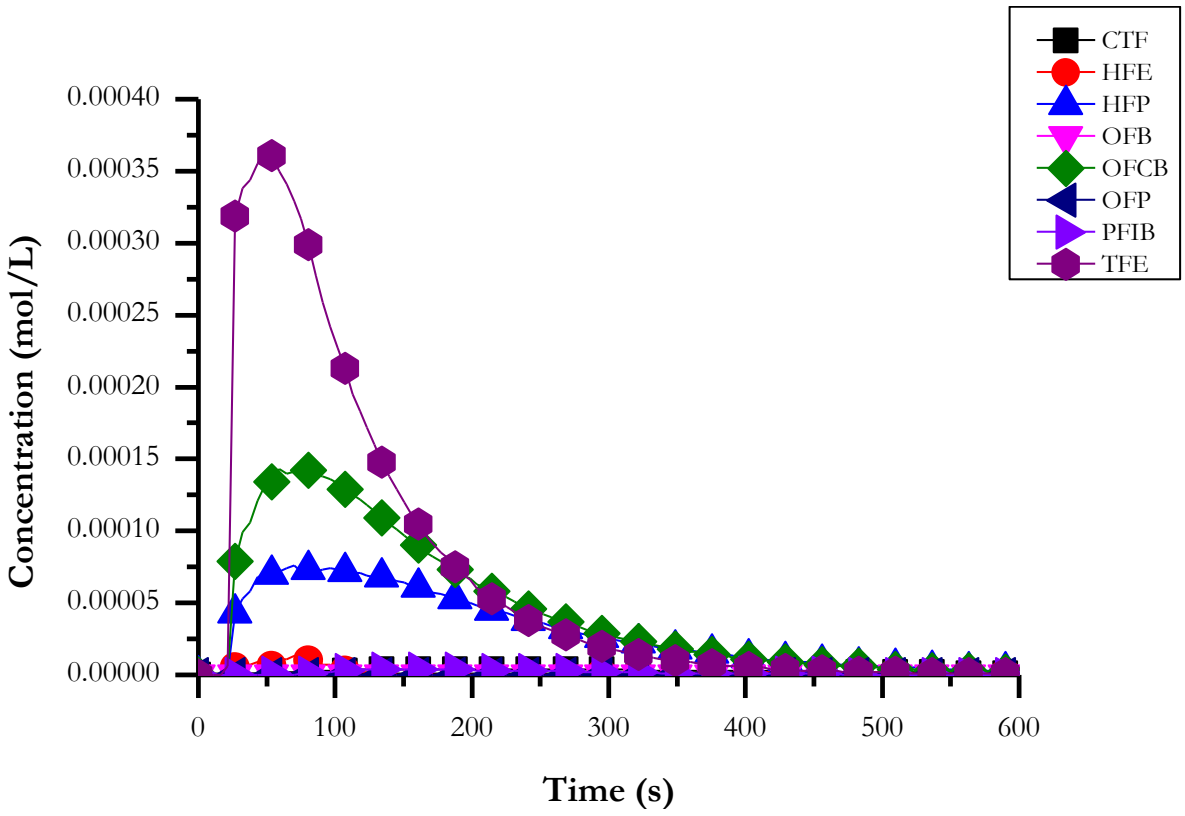

Figure 55: Concentration profile as determine with the quantification function for the pyrolysis of 0.1 g of PTFE at 650 °C and 70 kPa (abs.).

3.3.4.5 T = 750 °C and P = 10 kPa (abs.)

At 750 °C one would expect HFP to be the major product in a pyrolysis reaction. Figure 56 clearly shows that TFE in not the dominant product in the reaction. This is also clear in the calculated composition of the mixture (Table 16). OFCB is expected to be in the minority at these temperatures. The predicted concentration profile and composition data suggests that it is in accordance with the literature data.

The execution time is again within range and the average execution time was 2235 ms and the maximum was 2301 ms.

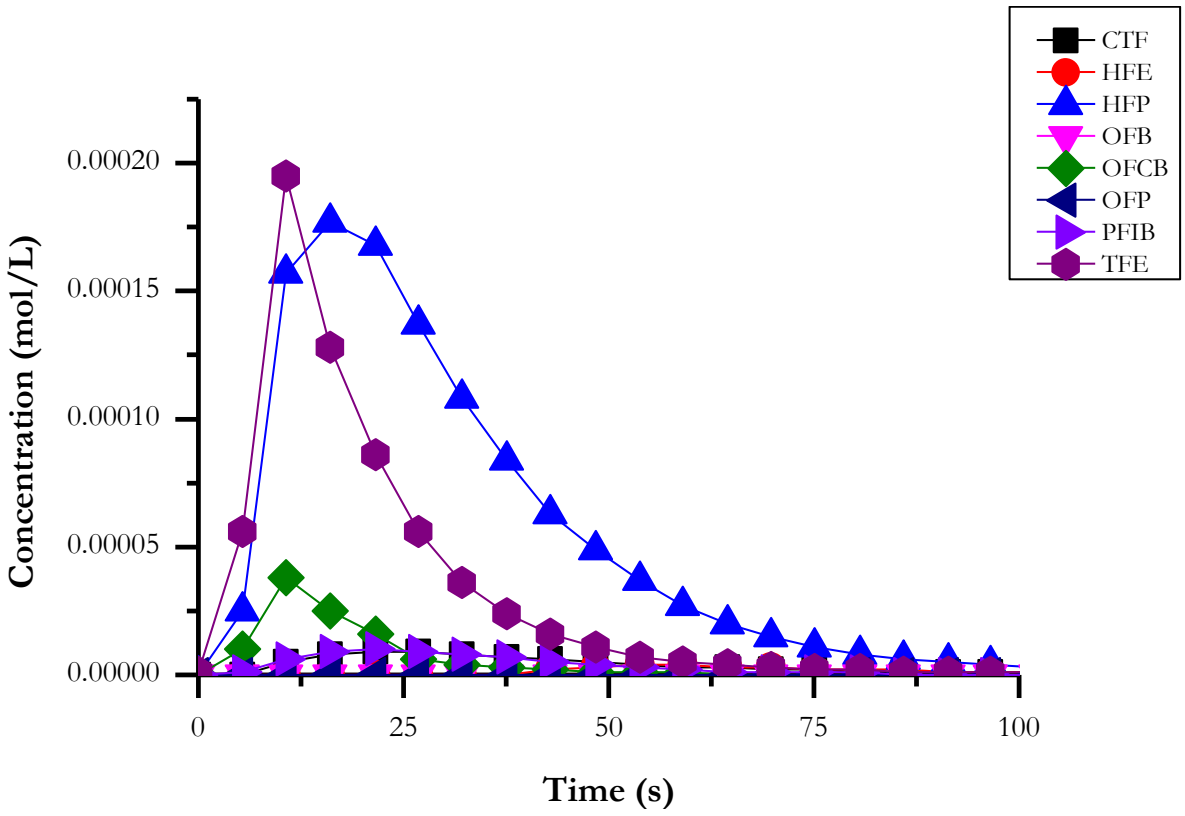

Figure 56: Concentration profile as determine with the quantification function for the pyrolysis of 0.1 g of PTFE at 750 °C and 10 kPa (abs.).

It should be noted (Table 16) that the quantification function detects the increase in PFIB production at elevated temperatures. This is particularly important with respect to safety and process control.

Table 16: Composition of the pyrolysis products at 750 °C and 10 kPa (abs) as determined by the quantification function.

Component	Calculated
CTF	0.053
HFE	0.017
HFP	0.467
OFCB	0.033
PFIB	0.021
TFE	0.409

3.3.4.6 T = 750 °C and P = 70 kPa (abs.)

At 750 °C and 70 kPa (abs.) the conversion of TFE to HFP is favoured and an appreciable amount of PFIB is generated. Figure 57 shows that the HFP is produced in large quantities, when compared to all other experiments, and that the production of TFE is mostly suppressed. This is in good agreement with literature.

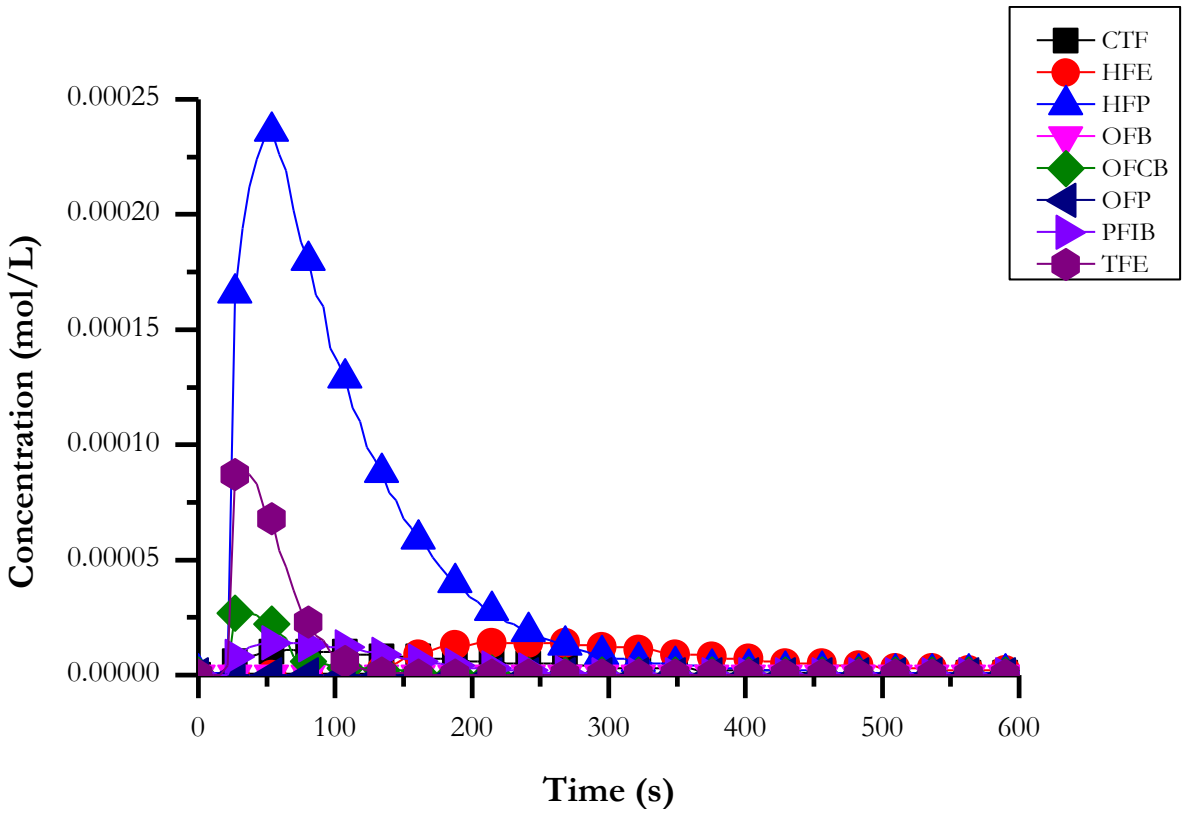

Figure 57: Concentration profile as determine with the quantification function for the pyrolysis of 0.1 g of PTFE at 750 °C and 70 kPa (abs.).

The average execution time for analysis of this experiment was 2210 ms and the maximum iteration was 2294 ms. The calculated composition data can be seen in Table 17. The function detects an increase in CTF as well as HFE which are produced in low quantities at the operating conditions. The predicted CTF composition should not be stated as a fact, since CTF is a single peak and could easily be fitted incorrectly.

Table 17: Composition of the pyrolysis products at 750 °C and 70 kPa (abs) as determined by the quantification function.

Component	Calculated
CTF	0.102
HFE	0.010
HFP	0.598
OFCB	0.025
PFIB	0.033
TFE	0.146

3.4 Conclusions and Recommendations

PTFE was successfully decomposed in a laboratory-scale pyrolysis reactor. The product selectivity obtained from a representative set of experiments compared well with the findings of other researchers (Lewis & Naylor, 1947; Meissner *et al.*, 2004 and Bhadury *et al.*, 2007).

Infra-red spectra were generated for the main compounds of interest, *viz.* TFE, HFP and OFCB. Spectra for the low fraction components, *viz.* carbon tetrafluoride, hexafluoroethane, octafluoropropane, and the perfluorobutenes, were generated by means of GC-FTIR. No absorbance spectra for the perfluorobutenes or octafluoropropane could be found the available literature. The spectra obtained by means of GC-FTIR are of low quality. However, FTIR spectroscopy can now be implemented to warn lab workers of the possible formation of the highly toxic perfluorobutenes.

Pure TFE was successfully generated in sufficient quantities to determine molar attenuation coefficients, at various pressures, for the respective absorbance peaks. Results confirm that TFE does not deviate from linearity at the conditions tested and therefore obeys Beer's law.

HFP, with an unknown composition, was procured and analysed for the presence of other perfluorocarbons. The composition was determined to have a purity better than 99.75 % and was deemed pure enough for the intended purpose. Pure spectra were captured at various pressures and the molar attenuation coefficients determined from these spectra. The absorptivity varied linearly as a function of the pressure, over the range of pressures tested. It can be concluded that HFP obeys Beer's law.

A mixture of TFE, HFP and OFCB was sampled and quantified by GC-MS. This mixture was then used to generate pressure dependent infrared spectra. The software was used to deconvolute the spectra. Molar attenuation coefficients were

calculated for all the components present and compared to the values from pure samples. The attenuation coefficient for OFCB was calculated and showed good adherence to Beer's law.

The ability of the software to perform real-time quantification of the PTFE pyrolysis stream was demonstrated over a range of experimental conditions spanning the temperature range 650 ºC to 850 ºC, and pressures from <1kPa to 70 kPa.

It is recommended that further high-purity spectra for each component at different pressures be generated in order to calibrate the software more accurately for the purpose of qualitative and quantitative analyses and to ensure reproducibility.

4 References

Atkinson, B and Atkinson VA (1957) "The thermal decomposition of tetrafluoroethylene" *Journal of the Chemical Society*, 2086 – 2094.

Atkinson, B and Trenwith, AB (1953) "The thermal decomposition of tetrafluoroethylene" *Journal of the Chemical Society*, 2082 – 2087.

Bhadury, PS, Singh, S, Sharma, M and Palit, M (2007) "Flash pyrolysis of polytetrafluoroethylene (Teflon) in a quartz assembly" *Journal of Analytical and Applied Pyrolysis*, 78 (2), 288 – 290.

Buravtsev, NN and Kolbanovskii, YA (2002) "Mechanism of hexafluoropropylene formation in gas-phase pyrolysis of tetrafluoroethylene" *Russian Journal of Applied Chemistry*, 75 (4), 598 – 605.

Butler, JN (1962) "The thermal decomposition of octafluorocyclobutane" *Journal of the American Chemical Society*, 84 (8), 1393 – 1398.

Cleveland, WS (1979) "Robust locally weighted regression and smoothing scatterplots" *Journal of the American Statistical Association*, 74 (368), 829 – 836.

Collins, RD, Fiveash, P and Holland, L (1969) "A mass spectrometry study of the evaporation and pyrolysis of polytetrafluoroethylene", *Vacuum*, 19 (3), 113 – 116.

Drennan, GA, Matula, RA (1968) "The pyrolysis of tetrafluoroethylene" *The Journal of Physical Chemistry*, 72 (10), 3462 – 3468.

Eilers, PHC (2003) "A perfect smoother" *Analytical Chemistry*, 75 (14), 3631 – 3636.

Friedrichs, MS (1995) "A model-free algorithm for the removal of baseline artifacts" *Journal of Biomolecular NMR*, 5 (2), 147 – 153.

He, S, Zhang, W, Liu, L, Huang, Y, He, J, Xie, W, Wu, P, Du, C (2014) "Baseline correction for Raman spectra using an improved asymmetric least squares method" *Analytical Methods*, 6 (12), 4402 – 4407.

Hoerman, B (2006) "Weighted curve fit" LabVIEW Example Programs v6.0, http://www.ni.com/example/29499/en/

Kneen, MA and Annegarn, HJ (1996) "Algorithm for fitting XRF, SEM and PIXE X-ray spectra backgrounds" *Nuclear Instruments and Methods in Physics Research B*, 109/110 (April) 209 – 213.

Komsta, Ł (2011) "Comparison of several methods of chromatographic baseline removal with a new approach based on quantile regression" *Chromatographia*, 73 (7-8), 721 – 731.

Książcak, A, Boniuk, H & Cudzilo, S (2003) "Thermal decomposition of PTFE in the presence of silicon, calcium silicide, ferrosilicon and iron" *Journal of Thermal Analysis and Calorimetry*, 74 (2), 569 – 574.

Lacher, JR, Tompkin, GW and Park, JD (1952) "The kinetics of the vapour phase dimerization of tetrafluoroethylene and trifluorochloroethylene" *Journal of the American Chemical Society*, 74 (7), 1693 – 1696.

Lewis, EE, Naylor, MA (1947) "Pyrolysis of polytetrafluoroethylene" *Journal of the American Chemical Society*, 69 (8), 1968 – 1970.

Liland, KH, Almøy, T and Mevik, BH (2010) "Optimal choice of baseline correction for multivariate calibration of spectra" *Applied Spectroscopy*, 64 (9), 1007 – 1016.

McCue, AJ, Mutch, GA, McNab, AI, Campbell, S and Anderson, JA (2015) "Quantitative determination of surface species and adsorption sites using infrared spectroscopy" *Catalysis Today*, 259 (1), 19 – 26.

Meissner, E, Wróblewska, A and Milchert, E (2004) "Technological parameters of pyrolysis of waste polytetrafluoroethylene" *Polymer Degradation and Stability*, 83 (1), 163 – 172.

Morisaki, S (1978) "Simultaneous thermogravimetry-mass spectrometry and pyrolysis-gas chromatography of fluorocarbon polymers" *Thermochimica Acta*, 25 (2), 171 – 183.

Pike Technologies (2015) "Choice of window materials for transmission sampling of liquids in the mid-IR spectral range" *Application Note – 0602*, http://www.piketech.com/skin/fashion_mosaic_blue/application-pdfs/CrystalChoiceForTransmission.pdf [2015/12/03].

Pitha, J and Jones, RN (1966) "A comparison of optimization methods for fitting curves to infrared band envelopes" *Canadian Journal of Chemistry*, 44 (24), 3031 – 3050.

Ruckstuhl, AF, Jacobson, MP, Field, RW, Dodd, JA (2011) "Baseline subtraction using robust local regression estimation" *Journal of Quantitative Spectroscopy & Radiative Transfer* 68 (2), 179 – 193.

Schulze, G, Jirasek, A, Yu, MML, Lim, A, Turner, RFB and Blades, MW (2005) "Investigation of selected baseline removal techniques as candidates for automated implementation" *Applied Spectroscopy*, 59 (5), 545 – 574.

Simon, CM and Kaminsky, W (1998) "Chemical recycling of polytetrafluoroethylene by pyrolysis" *Polymer Degradation and Stability*, 62 (1), 1 – 7.

Skoog, DA, Holler, FJ and Nieman, TA (1998) *Principles of Instrumental Analysis*, Thomson Learning, London.

Stancik, AL and Brauns, EB (2008) "A simple asymmetric lineshape for fitting infrared absorption spectra" *Vibrational Spectroscopy*, 47 (1), 66 – 69.

Stec, AA, Fardell, P, Blomqvist, P, Bustamante-Valencia, L, Saragoza, L and Guillaume, E (2011) "Quantification of fire gases by FTIR: Experimental characterization of calibration systems" *Fire Safety Journal*, 46 (5), 225 – 233.

Szekely, T, Varhegyi, G, Till, F, Szabo, P and Jakab, E (1987) "The effects of heat and mass transport on the results of thermal decomposition studies: Part 2. Polystyrene, polytetrafluoroethylene and polypropylene" *Journal of Analytical and Applied Pyrolysis*, 11, 83 – 92.

Urben, P (2007) *Bretherick's Handbook of Reactive Chemical Hazards*, Volume 1, Elsevier.

Vandeginste, BGM, De Galan, L (1975) "Critical evaluation of curve fitting in infrared spectrometry" *Analytical Chemistry*, 47 (13), 2124 – 2132.

Xin, H, Wang, D, Qi, X, Qi, G and Dou, G (2014) "Structural characteristics of coal functional groups using quantum chemistry for quantification of infrared spectra" *Fuel Processing Technology*, 118, 287 – 295.

5 Appendices

5.1 Synthetic Spectra and the Result Obtained from Processing

Figure 58 to Figure 61 show the synthetic spectra processed by the three pre-processing techniques. These spectra were processed using the recommended parameters for each method.

The legend to all these figures are:

- The solid black line represents the original, synthetic spectra;
- Solid red dots indicate the position and intensity of any detected peaks;
- ALS method is represented by the solid red line;
- NMM is represented by the dashed blue line; and
- LOWESS procedure is represented by the solid green line.

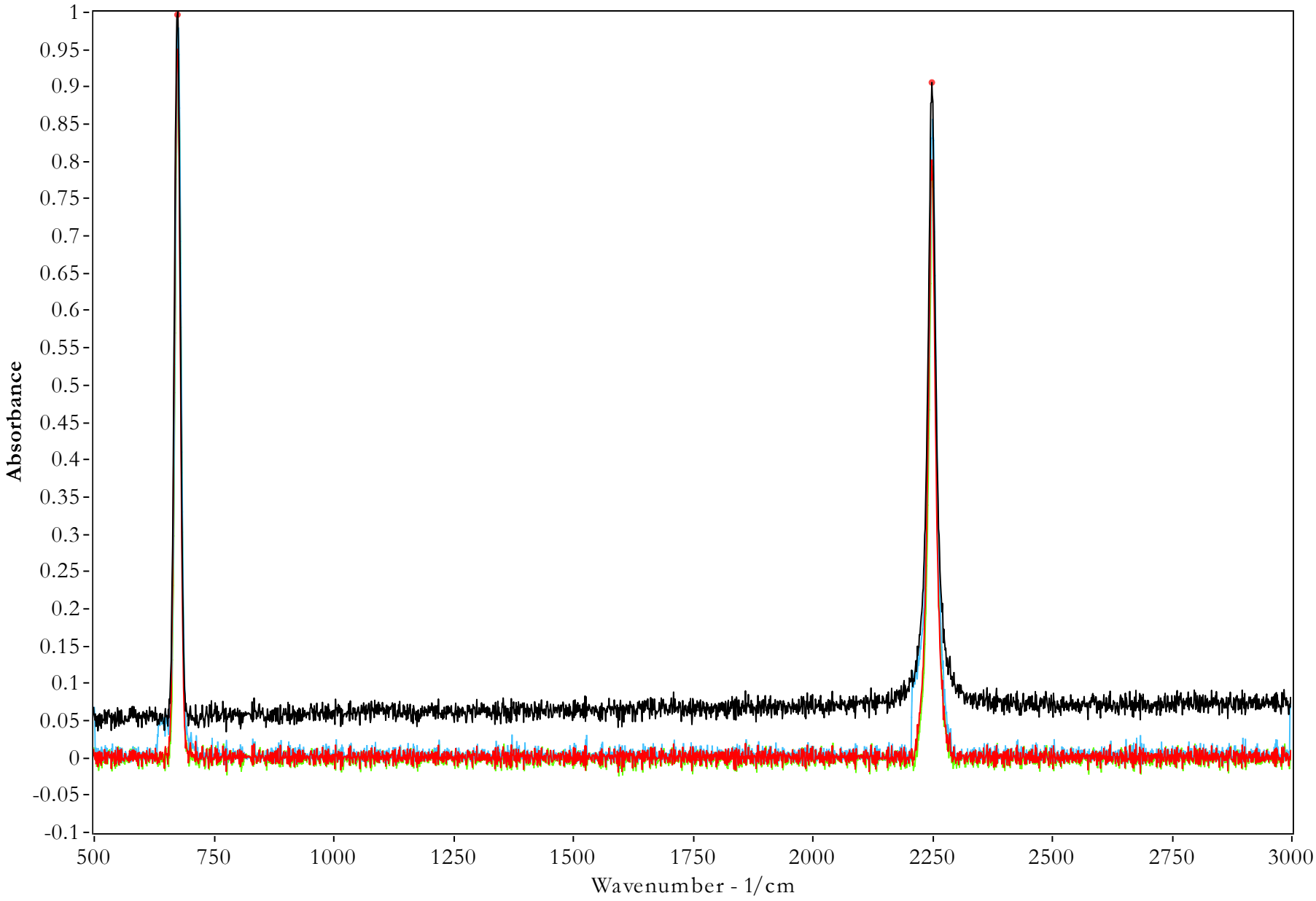

Figure 58: Spectrum N1B1S1, also indicated are the detected peaks and the solutions from all three processing methods.

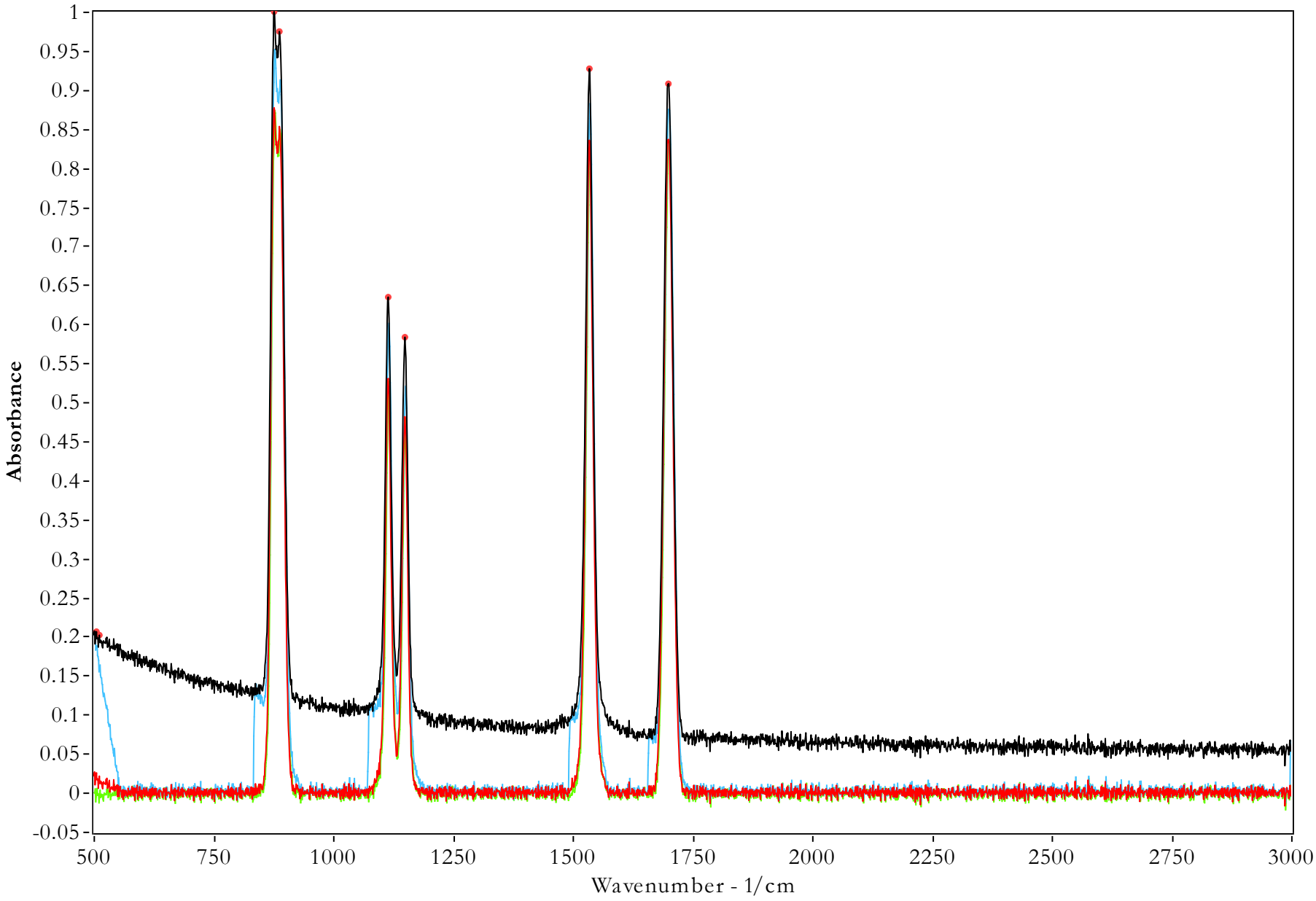

Figure 59: Spectrum N2B2S2, also indicated are the detected peaks and the solutions from all three processing methods.

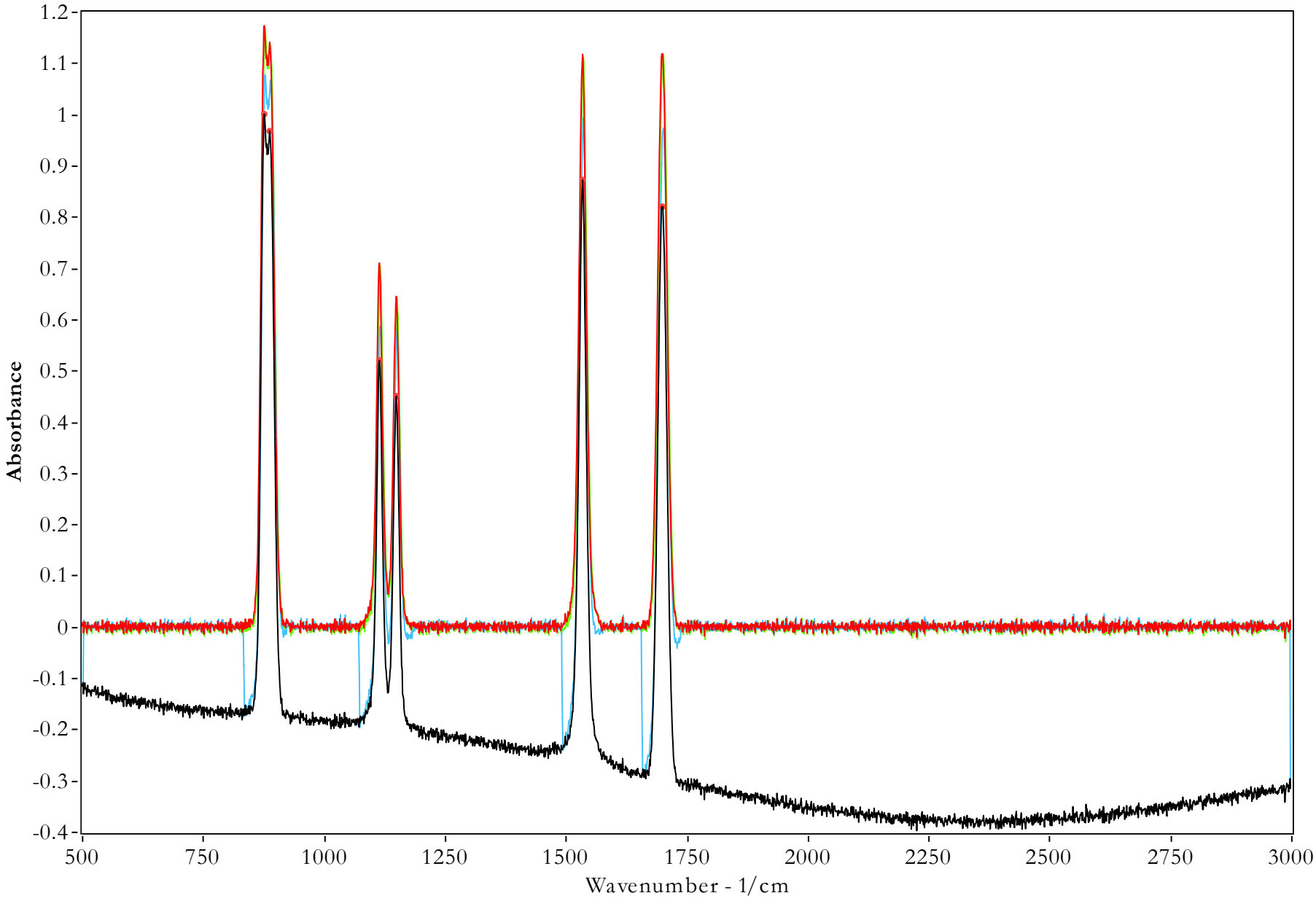

Figure 60: Spectrum N2B3S2, also indicated are the detected peaks and the solutions from all three processing methods.

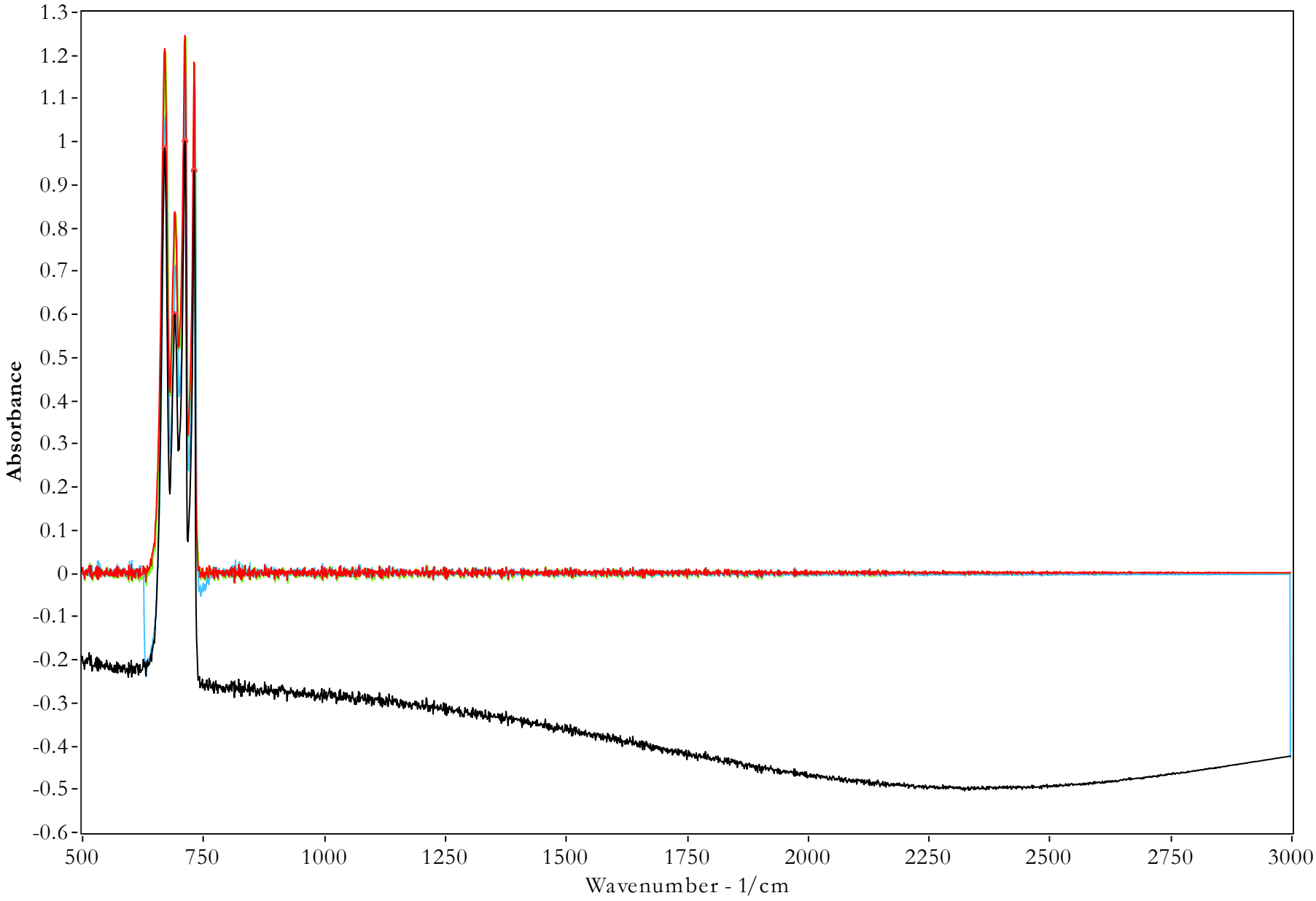

Figure 61: Spectrum N3B3S4, also indicated are the detected peaks and the solutions from all three processing methods.

5.2 Synthetic Spectra Lineshape Fitting Parameters

Table 18 to Table 25 show all parameters solved for by means of the TRDL and LM non-linear solver. The LM solution for an asymmetric lineshape is also included. The values under the heading "Exact" are the actual parameters used to generate the respective signals.

Table 18: Comparison of all the parameters solved for the synthetic signal spectrum S1.

Peak #	Parameter		Exact	TRDL	LM	Asym. LM
1	Centre	x_0	675	675.000	675.000	675.000
	Area	A	12	11.999	11.999	11.999
	FWHM	γ	14	13.999	13.999	13.999
	Voigt	f	0	0.000	0.000	0.000
	Asymmetry	a	0	0.000	0.000	0.000
2	Centre	x_0	2250	2250.000	2250.000	2250.000
	Area	A	20	19.647	19.646	19.647
	FWHM	γ	18	17.978	17.984	17.979
	Voigt	f	1	0.974	0.974	0.974
	Asymmetry	a	0	0.000	0.000	0.000

Table 19: Comparison of all the parameters solved for the synthetic signal spectrum N1B1S1.

Peak #	Parameter		Exact	TRDL	LM	Asym. LM
1	Centre	x_0	675	674.983	674.983	674.979
	Area	A	12	11.965	11.961	11.963
	FWHM	γ	14	13.930	13.931	13.932
	Voigt	f	0	0.000	0.000	0.000
	Asymmetry	a	0	0.000	0.000	0.000
2	Centre	x_0	2250	2250.000	2250.000	2249.998
	Area	A	20	17.685	17.593	17.665
	FWHM	γ	18	18.031	18.418	18.143
	Voigt	f	1	0.807	0.769	0.796
	Asymmetry	a	0	0.000	0.000	-0.001

Table 20: Comparison of all the parameters solved for the synthetic signal spectrum S2.

Peak #	Parameter		Exact	TRDL	LM	Asym. LM
1	Centre	x_0	875	874.911	874.910	874.876
	Area	A	12	11.776	11.776	11.702
	FWHM	γ	14	13.942	13.942	13.765
	Voigt	f	0.25	0.225	0.225	0.191
	Asymmetry	a	0	0.000	0.000	0.005
2	Centre	x_0	1535	1535.000	1535.000	1534.998
	Area	A	20	18.596	18.596	18.597
	FWHM	γ	18	18.079	18.079	18.079
	Voigt	f	0.55	0.401	0.401	0.401
	Asymmetry	a	0	0.000	0.000	0.000
3	Centre	x_0	890	889.935	889.935	889.901
	Area	A	16	15.650	15.650	15.644
	FWHM	γ	18	18.143	18.144	17.938
	Voigt	f	0.1	0.015	0.015	0.000
	Asymmetry	a	0	0.000	0.000	-0.004
4	Centre	x_0	1115	1115.020	1115.020	1115.012
	Area	A	10	9.630	9.630	9.641
	FWHM	γ	14	14.050	14.050	14.049
	Voigt	f	0.6	0.524	0.524	0.526
	Asymmetry	a	0	0.000	0.000	-0.002
5	Centre	x_0	1150	1149.980	1149.980	1149.993
	Area	A	8	7.732	7.732	7.708
	FWHM	γ	14	14.057	14.057	14.055
	Voigt	f	0.3	0.220	0.220	0.214
	Asymmetry	a	0	0.000	0.000	0.002
6	Centre	x_0	1700	1700.004	1700.004	1700.002
	Area	A	20	19.937	19.937	19.936
	FWHM	γ	22	21.954	21.954	21.954
	Voigt	f	0	0.000	0.000	0.000
	Asymmetry	a	0	0.000	0.000	0.000

Table 21: Comparison of all the parameters solved for the synthetic signal spectrum N2B2S2.

Peak #	Parameter		Exact	TRDL	LM	Asym. LM
1	Centre	x_0	875	874.942	874.923	874.919
	Area	A	12	11.838	11.789	11.777
	FWHM	γ	14	13.963	13.938	13.908
	Voigt	f	0.25	0.228	0.228	0.218
	Asymmetry	a	0	0.000	0.000	0.002
2	Centre	x_0	1535	1534.998	1534.998	1534.991
	Area	A	20	18.521	18.521	18.521
	FWHM	γ	18	18.029	18.030	18.029
	Voigt	f	0.55	0.396	0.396	0.397
	Asymmetry	a	0	0.000	0.000	-0.001
3	Centre	x_0	890	889.934	889.910	889.906
	Area	A	16	15.551	15.599	15.618
	FWHM	γ	18	18.162	18.202	18.144
	Voigt	f	0.1	0.000	0.000	0.000
	Asymmetry	a	0	0.000	0.000	-0.001
4	Centre	x_0	1115	1115.023	1115.023	1115.013
	Area	A	10	9.705	9.704	9.711
	FWHM	γ	14	13.929	13.930	13.929
	Voigt	f	0.6	0.546	0.545	0.547
	Asymmetry	a	0	0.000	0.000	-0.003
5	Centre	x_0	1150	1149.966	1149.966	1149.974
	Area	A	8	7.585	7.586	7.564
	FWHM	γ	14	14.132	14.132	14.129
	Voigt	f	0.3	0.173	0.173	0.167
	Asymmetry	a	0	0.000	0.000	0.001
6	Centre	x_0	1700	1700.000	1700.000	1699.988
	Area	A	20	19.953	19.953	19.943
	FWHM	γ	22	21.969	21.969	21.971
	Voigt	f	0	0.000	0.000	0.000
	Asymmetry	a	0	0.000	0.000	-0.001

Table 22: Comparison of all the parameters solved for the synthetic signal spectrum S3.

Peak #	Parameter		Exact	TRDL	LM	Asym. LM
1	Centre	x_0	875	875.377	875.377	875.827
	Area	A	12	17.219	17.218	19.519
	FWHM	γ	14	14.573	14.571	17.990
	Voigt	f	0.25	1.000	1.000	1.000
	Asymmetry	a	0.05	0.000	0.000	-0.087
2	Centre	x_0	1535	1534.839	1534.868	1535.343
	Area	A	20	18.307	18.316	18.152
	FWHM	γ	18	15.579	15.492	15.879
	Voigt	f	0.55	0.652	0.661	0.536
	Asymmetry	a	0.1	0.000	0.000	0.093
3	Centre	x_0	915	916.269	916.269	916.941
	Area	A	16	8.699	8.699	8.699
	FWHM	γ	18	6.936	6.936	6.936
	Voigt	f	0.1	0.557	0.557	0.454
	Asymmetry	a	0.2	0.000	0.000	0.199
4	Centre	x_0	1100	1100.740	1100.740	1101.107
	Area	A	10	6.006	6.006	6.006
	FWHM	γ	14	6.959	6.959	6.959
	Voigt	f	0.6	0.751	0.751	0.591
	Asymmetry	a	0.3	0.000	0.000	0.236
5	Centre	x_0	1150	1151.204	1151.204	1151.501
	Area	A	8	3.601	3.601	3.601
	FWHM	γ	14	4.107	4.107	4.107
	Voigt	f	0.3	0.708	0.708	0.615
	Asymmetry	a	0.4	0.000	0.000	0.358
6	Centre	x_0	1700	1702.240	1702.241	1702.519
	Area	A	8	2.547	2.547	2.547
	FWHM	γ	22	3.299	3.299	3.299
	Voigt	f	0	0.692	0.692	0.636
	Asymmetry	a	0.4	0.000	0.000	0.395

Table 23: Comparison of all the parameters solved for the synthetic signal spectrum N1B1S3.

Peak #	Parameter		Exact	TRDL	LM	Asym. LM
1	Centre	x_0	875	875.389	875.389	875.766
	Area	A	12	17.031	17.029	19.073
	FWHM	γ	14	14.348	14.346	17.369
	Voigt	f	0.25	1.000	1.000	1.000
	Asymmetry	a	0.05	0.000	0.000	-0.084
2	Centre	x_0	1535	1534.809	1534.838	1535.336
	Area	A	20	18.229	18.240	18.110
	FWHM	γ	18	15.645	15.557	15.851
	Voigt	f	0.55	0.632	0.641	0.529
	Asymmetry	a	0.1	0.000	0.000	0.092
3	Centre	x_0	915	916.253	916.253	916.912
	Area	A	16	8.804	8.804	8.804
	FWHM	γ	18	7.022	7.022	7.022
	Voigt	f	0.1	0.557	0.557	0.452
	Asymmetry	a	0.2	0.000	0.000	0.198
4	Centre	x_0	1100	1100.773	1100.774	1101.151
	Area	A	10	5.921	5.921	5.921
	FWHM	γ	14	6.805	6.805	6.805
	Voigt	f	0.6	0.746	0.746	0.585
	Asymmetry	a	0.3	0.000	0.000	0.239
5	Centre	x_0	1150	1151.172	1151.172	1151.470
	Area	A	8	3.613	3.613	3.613
	FWHM	γ	14	4.156	4.156	4.156
	Voigt	f	0.3	0.701	0.701	0.610
	Asymmetry	a	0.4	0.000	0.000	0.360
6	Centre	x_0	1700	1702.238	1702.239	1702.510
	Area	A	8	2.581	2.581	2.581
	FWHM	γ	22	3.379	3.379	3.379
	Voigt	f	0	0.685	0.685	0.630
	Asymmetry	a	0.4	0.000	0.000	0.386

Table 24: Comparison of all the parameters solved for the synthetic signal spectrum S4.

Peak #	Parameter		Exact	TRDL	LM	Asym. LM
1	Centre	x_0	670	670.445	670.429	670.175
	Area	A	12	15.912	15.818	12.185
	FWHM	γ	14	14.676	14.629	14.280
	Voigt	f	0.25	0.626	0.627	0.185
	Asymmetry	a	0.05	0.000	0.000	0.039
2	Centre	x_0	690	692.284	692.280	691.334
	Area	A	8	6.608	6.848	11.407
	FWHM	γ	16	13.631	13.628	14.856
	Voigt	f	0.55	0.000	0.095	1.000
	Asymmetry	a	0.1	0.000	0.000	-0.025
3	Centre	x_0	710	711.690	711.700	711.459
	Area	A	12	14.293	14.197	11.427
	FWHM	γ	18	11.248	11.248	11.248
	Voigt	f	0.1	1.000	1.000	0.766
	Asymmetry	a	0.2	0.000	0.000	0.165
4	Centre	x_0	730	730.994	730.994	731.216
	Area	A	12	5.134	5.131	7.088
	FWHM	γ	14	6.854	6.854	6.854
	Voigt	f	0.6	0.000	0.000	0.566
	Asymmetry	a	0.3	0.000	0.000	0.236

Table 25: Comparison of all the parameters solved for the synthetic signal spectrum N3B3S4.

Peak #	Parameter		Exact	TRDL	LM	Asym. LM
1	Centre	x_0	670	670.416	670.414	670.148
	Area	A	12	15.792	15.817	11.879
	FWHM	γ	14	14.752	14.735	14.351
	Voigt	f	0.25	0.605	0.610	0.122
	Asymmetry	a	0.05	0.000	0.000	0.039
2	Centre	x_0	690	692.318	692.330	691.284
	Area	A	8	6.643	6.666	11.560
	FWHM	γ	16	13.731	13.782	15.059
	Voigt	f	0.55	0.000	0.003	1.000
	Asymmetry	a	0.1	0.000	0.000	-0.022
3	Centre	x_0	710	711.700	711.706	711.465
	Area	A	12	14.268	14.238	11.338
	FWHM	γ	18	11.243	11.243	11.243
	Voigt	f	0.1	1.000	1.000	0.755
	Asymmetry	a	0.2	0.000	0.000	0.168
4	Centre	x_0	730	730.993	730.993	731.191
	Area	A	12	5.216	5.216	7.247
	FWHM	γ	14	6.955	6.955	6.955
	Voigt	f	0.6	0.000	0.000	0.579
	Asymmetry	a	0.3	0.000	0.000	0.237

5.3 Lineshape Parameters of Experimentally Obtained Spectra

5.3.1 Lineshape Parameters for Tetrafluoroethylene

Table 26: Best fit parameters for pure TFE.

Peak #	Parameter		LM	Asym. LM
1	Centre	x_0	1179	1179
	Area	A	13.177	12.179
	FWHM	γ	14.054	12.968
	Voigt	f	0.233	0.192
	Asymmetry	a	0	0.022
2	Centre	x_0	1195	1195
	Area	A	8.832	8.239
	FWHM	γ	8.877	8.277
	Voigt	f	0.114	0.000
	Asymmetry	a	0	-0.044
3	Centre	x_0	1329	1330
	Area	A	16.442	16.711
	FWHM	γ	15.511	16.243
	Voigt	f	0.452	0.087
	Asymmetry	a	0	0.032
4	Centre	x_0	1344	1344
	Area	A	13.078	10.844
	FWHM	γ	11.962	11.455
	Voigt	f	0.592	0.029
	Asymmetry	a	0	-0.080
5	Centre	x_0	1186	1187
	Area	A	1.588	2.982
	FWHM	γ	4.263	5.560
	Voigt	f	0	0.000
	Asymmetry	a	0	-0.060

5.3.2 Lineshape Parameters for Hexafluoropropylene

Table 27: Best fit parameters for pure HFP.

Peak #	Parameter		LM	Asym. LM
1	Centre	x_0	654	654
	Area	A	1.145	1.118
	FWHM	γ	19.041	17.048
	Voigt	f	0.013	0.108
	Asymmetry	a	0	0.005
2	Centre	x_0	767	767
	Area	A	1.080	0.970
	FWHM	γ	21.093	16.640
	Voigt	f	0.000	0.000
	Asymmetry	a	0	0.007
3	Centre	x_0	1035	1035
	Area	A	17.973	17.791
	FWHM	γ	17.604	17.628
	Voigt	f	0.100	0.070
	Asymmetry	a	0	0.012
4	Centre	x_0	1179	1179
	Area	A	24.488	22.330
	FWHM	γ	20.412	19.408
	Voigt	f	0.552	0.487
	Asymmetry	a	0	0.008
5	Centre	x_0	1210	1210
	Area	A	19.953	21.841
	FWHM	γ	20.744	21.806
	Voigt	f	0.000	0.099
	Asymmetry	a	0	0.012
6	Centre	x_0	1329	1329
	Area	A	9.224	10.706
	FWHM	γ	13.522	13.274
	Voigt	f	0.675	0.652
	Asymmetry	a	0	0.016
7	Centre	x_0	1338	1339
	Area	A	6.745	4.621
	FWHM	γ	11.572	10.476
	Voigt	f	0.612	0.056
	Asymmetry	a	0	-0.043
	Voigt	f	0.135	0.152
	Asymmetry	a	0	0.025

Peak #	Parameter		LM	Asym. LM
8	Centre	x_0	1395	1396
	Area	A	15.007	15.470
	FWHM	γ	21.377	21.830
	Centre	x_0	1395	1396
	Area	A	15.007	15.470
9	Centre	x_0	1794	1794
	Area	A	10.399	10.440
	FWHM	γ	18.667	18.649
	Voigt	f	0.415	0.425
	Asymmetry	a	10.399	0.002

5.3.3 Lineshape Parameters for Octafluorocyclobutane

Table 28: Best fit parameters for OFCB.

Peak #	Parameter		LM	Asym. LM
1	Centre	x_0	568	569
	Area	A	1.936	1.886
	FWHM	γ	12.578	12.665
	Voigt	f	0.000	0.000
	Asymmetry	a	0	0.005
2	Centre	x_0	962	962
	Area	A	16.187	16.286
	FWHM	γ	12.485	12.481
	Voigt	f	0.453	0.468
	Asymmetry	a	0	-0.003
3	Centre	x_0	1236	1236
	Area	A	22.751	17.784
	FWHM	γ	27.177	28.315
	Voigt	f	0.971	0.369
	Asymmetry	a	0	0.047
4	Centre	x_0	1339	1339
	Area	A	8.941	7.801
	FWHM	γ	20.704	20.627
	Voigt	f	0.536	0.241
	Asymmetry	a	0	0.005
5	Centre	x_0	1270	1267
	Area	A	0.310	1.297
	FWHM	γ	7.580	12.172
	Voigt	f	0.000	1.000
	Asymmetry	a	0	0.062
6	Centre	x_0	1288	1288
	Area	A	5.703	10.038
	FWHM	γ	19.152	19.756
	Voigt	f	0.002	1.000
	Asymmetry	a	0	-0.008

5.3.4 Lineshape Parameters of Carbon Tetrafluoride

Table 29: Best fit parameters for pure CTF.

Peak #	Parameter		LM	Asym. LM
1	Centre	x_0	1282	1282
	Area	A	10.082	10.141
	FWHM	γ	8.247	8.362
	Voigt	f	0.396	0.380
	Asymmetry	a	0.000	0.071

5.3.5 Lineshape Parameters of Hexafluoroethane

Table 30: Best fit parameters for pure HFE.

Peak #	Parameter		LM	Asym. LM
1	Centre	x_0	1115	1113
	Area	A	3.958	2.276
	FWHM	γ	17.081	11.818
	Voigt	f	0.365	0.000
	Asymmetry	a	0	0.180
2	Centre	x_0	1124	1122
	Area	A	0.426	1.919
	FWHM	γ	4.829	8.389
	Voigt	f	0.000	0.470
	Asymmetry	a	0	-0.011
3	Centre	x_0	1250	1250
	Area	A	15.202	15.163
	FWHM	γ	13.342	13.361
	Voigt	f	0.199	0.188
	Asymmetry	a	0	0.011
4	Centre	x_0	1282	1282
	Area	A	0.346	0.365
	FWHM	γ	6.930	7.129
	Voigt	f	0.000	0.000
	Asymmetry	a	0	0.021

5.3.6 Lineshape Parameters for Octafluoropropane

Table 31: Best fit parameters for pure OFP.

Peak #	Parameter		LM	Asym. LM
1	Centre	x_0	1.625	1.625
	Area	A	729.562	729.539
	FWHM	γ	15.900	16.029
	Voigt	f	1.000	1.000
	Asymmetry	a		0.011
2	Centre	x_0	4.199	4.115
	Area	A	1005.781	1005.850
	FWHM	γ	15.084	15.114
	Voigt	f	0.384	0.335
	Asymmetry	a		0.008
3	Centre	x_0	1153	1153
	Area	A	3.295	3.228
	FWHM	γ	15.132	15.119
	Voigt	f	0.379	0.358
	Asymmetry	a	0	0.025
4	Centre	x_0	1206	1206
	Area	A	2.140	2.056
	FWHM	γ	16.449	16.187
	Voigt	f	0.000	0.000
	Asymmetry	a	0	0.012
5	Centre	x_0	1262	1262
	Area	A	18.967	18.678
	FWHM	γ	13.545	13.760
	Voigt	f	0.816	0.762
	Asymmetry	a	0	0.015
6	Centre	x_0	1349	1349
	Area	A	2.503	3.008
	FWHM	γ	16.922	17.215
	Voigt	f	0.703	1.000
	Asymmetry	a	0	0.049

5.3.7 Lineshape Parameters for 1- and 2-Octafluorobutene

Table 32: Best fit parameters for pure 1- and 2- OFB.

Peak #	Parameter		LM	Asym. LM
1	Centre	x_0	710	710
	Area	A	1.675	1.669
	FWHM	γ	11.615	11.492
	Voigt	f	0.000	0.000
	Asymmetry	a	0	-0.006
2	Centre	x_0	860	860
	Area	A	0.400	0.395
	FWHM	γ	16.725	16.364
	Voigt	f	0.000	0.000
	Asymmetry	a	0	0.004
3	Centre	x_0	922	922
	Area	A	1.824	1.815
	FWHM	γ	12.922	12.837
	Voigt	f	0.000	0.000
	Asymmetry	a	0	0.000
4	Centre	x_0	1114	1114
	Area	A	7.478	7.323
	FWHM	γ	13.243	13.368
	Voigt	f	0.083	0.009
	Asymmetry	a	0	0.016
5	Centre	x_0	1307	1307
	Area	A	5.974	7.091
	FWHM	γ	15.317	16.125
	Voigt	f	0.000	0.246
	Asymmetry	a	0	0.021
6	Centre	x_0	1362	1362
	Area	A	13.110	13.293
	FWHM	γ	11.623	11.622
	Voigt	f	0.194	0.224
	Asymmetry	a	0	0.011

Peak #	Parameter		LM	Asym. LM
7	Centre	x_0	1394	1395
	Area	A	0.498	0.564
	FWHM	γ	18.478	18.300
	Voigt	f	0.000	0.000
	Asymmetry	a	0	0.033
8	Centre	x_0	1254	1254
	Area	A	17.317	17.233
	FWHM	γ	18.081	18.284
	Voigt	f	0.766	0.648
	Asymmetry	a	0	0.018
9	Centre	x_0	1275	1275
	Area	A	13.007	11.705
	FWHM	γ	12.713	13.093
	Voigt	f	0.612	0.233
	Asymmetry	a	0	-0.011

5.3.8 Lineshape Parameters for Perfluoroisobutene

Table 33: Best fit parameters for pure PFIB.

Peak #	Parameter		LM	Asym. LM
1	Centre	x_0	714	714
	Area	A	0.276	0.269
	FWHM	γ	21.461	21.386
	Voigt	f	0.000	0.000
	Asymmetry	a	0	-0.022
2	Centre	x_0	720	720
	Area	A	0.369	0.371
	FWHM	γ	13.899	13.993
	Voigt	f	0.000	0.000
	Asymmetry	a	0	0.013
3	Centre	x_0	1000	1000
	Area	A	1.248	1.221
	FWHM	γ	15.207	15.088
	Voigt	f	0.030	0.000
	Asymmetry	a	0	-0.006
4	Centre	x_0	1047	1048
	Area	A	1.974	1.970
	FWHM	γ	16.096	16.096
	Voigt	f	0.000	0.000
	Asymmetry	a	0	0.019
5	Centre	x_0	1115	1115
	Area	A	3.586	3.240
	FWHM	γ	17.679	17.020
	Voigt	f	0.178	0.000
	Asymmetry	a	0	0.012
6	Centre	x_0	1124	1124
	Area	A	0.384	0.475
	FWHM	γ	4.758	5.272
	Voigt	f	0.000	0.000
	Asymmetry	a	0	-0.134
7	Centre	x_0	1193	1193
	Area	A	5.756	5.491
	FWHM	γ	16.443	16.824
	Voigt	f	0.666	0.540
	Asymmetry	a	0	0.031

Peak #	Parameter		LM	Asym. LM
8	Centre	x_0	1250	1250
	Area	A	17.923	17.996
	FWHM	γ	13.694	13.706
	Voigt	f	0.578	0.583
	Asymmetry	a	0	0.011
9	Centre	x_0	1314	1314
	Area	A	1.961	1.981
	FWHM	γ	22.114	22.180
	Voigt	f	1.000	1.000
	Asymmetry	a	0	0.024
10	Centre	x_0	1355	1355
	Area	A	0.573	0.645
	FWHM	γ	56.907	56.912
	Voigt	f	0.000	0.000
	Asymmetry	a	0	0.011
11	Centre	x_0	1355	1354
	Area	A	0.071	0.141
	FWHM	γ	15.304	15.296
	Voigt	f	0.743	0.617
	Asymmetry	a	0	0.283
12	Centre	x_0	1394	1395
	Area	A	3.394	3.478
	FWHM	γ	14.192	14.411
	Voigt	f	0.000	0.000
	Asymmetry	a	0	0.016
13	Centre	x_0	1750	1750
	Area	A	2.539	2.539
	FWHM	γ	16.938	17.082
	Voigt	f	0.070	0.047
	Asymmetry	a	0	0.021
14	Centre	x_0	1282	1282
	Area	A	2.027	2.199
	FWHM	γ	8.515	8.444
	Voigt	f	0.337	0.528
	Asymmetry	a	0	-0.010